Iowa State University
Digital Repository

1973

Swelling pressure of sodium montmorillonite in relation to interlayer spacing

Teeracharti Ruenkrairergsa
Iowa State University

Recommended Citation

www.manaraa.com

INFORMATION TO USERS

73-16,977

RUENKRAIRERGSA, Teeracharti, 1945-
SWELLING PRESSURE OF SODIUM MONTMORILLONITE IN
RELATION TO INTERLAYER SPACING.

Iowa State University, Ph.D., 1973
Engineering, civil

University Microfilms, A XEROX Company, Ann Arbor, Michigan

Swelling pressure of sodium montmorillonite

in relation to interlayer spacing

by

Teeracharti Ruenkrairergsa

A Dissertation Submitted to the

Graduate Faculty In Partial Fulfillment of

The Requirements for the Degree of

DOCTOR OF PHILOSOPHY

Department: Civil Engineering
Major: Soil Engineering

Approved:

In Charge of Major Work

For the Major Department

For the Graduate College

Iowa State University
Ames, Iowa
1973

PLEASE NOTE:

Some pages may have

indistinct print.

Filmed as received.

University Microfilms, A Xerox Education Company

TABLE OF CONTENTS

LIST OF FIGURES

LIST OF TABLES

INTRODUCTION

Statement of the Problem

Some of the most troublesome soils encountered by soil and foundation engineers are of a type termed expansive or swelling clays. Such soils contain large amounts of montmorillonite clay mineral. They are common in the Gulf Coastal Plain and in river floodplains of the central United States; on weathered basalt of the southwestern United States and central India; and in many other local areas. These areas are subjected to climatic conditions that are conductive to significant changes in moisture content during different seasons of the year. Expansive soils can also give trouble in any region where construction is accomplished in a dry season and the soils absorb moisture during a subsequent wet season. If highly compacted, these soils will swell and produce uplift pressures of considerable intensity if the moisture content of the soil increases after compaction. This action may result in heaving that is intolerable to support structures. Heave can result in the failure of a highway embankment, cracking of concrete structures and tilting of buildings.

Because of the problems caused by expansive soils, this research was directed to an investigation of the shrink-swell phenomenon caused by the change in moisture content. The study was divided into two phases; one is the study of the shrink-swell phenomenon due to the processes of adsorption and desorption of water on montmorillonite, and the other study concerns the process of mechanically loading and unloading a montmorillonitic clay sample.

Scope

The scope of the study is concentrated on the physico-chemical and mineralogical aspects of montmorillonite clay expansion, and involves volume and energy relationships. The X-ray diffraction data were obtained and analyzed under varying conditions of partial vacuum on the one hand, and variable applied mechanical pressure on the other. Both apparatuses used in the study were designed by Olson(89), and worked properly throughout the period of the investigation. From the X-ray and adsorption-desorption data, swelling pressures at various clay interlayer spacings or hydration states can be deduced and then compared to those induced by mechanical means.

THEORY AND REVIEW OF LITERATURE

Clay-Water System

Many investigators (12,64,105) have presented evidence to show that the water held directly on the surfaces of clay particles is in a physical state different from that of liquid water. The specific characteristics of this water which delimit it from ordinary water would be restricted to relatively short distances from the clay-particle surface. Terzaghi (105) explained the surface adsorption of water on the basis of the dipole character of the water molecule; the latter possesses positive and negative charges, the centers of which do not coincide. Since the surface of the clay particle is normally negatively charged, the positive ends of the water molecules are considered to be attracted toward the clay surface, the negative ends extending outward. The initial layer of water is believed to consist of water molecules which form another surface of negative charges on which can be built another layer of completely oriented water molecules. This process of building up layer upon layer could be continued indefinitely were it not for the fact that the water molecules possess thermal energy and tend to be in a state of continuous motion. In accordance with classical concepts of kinetic theory, the motion due to thermal energy opposes the regular orientation. At the actual clay-mineral surface the water molecule should be highly oriented, and the degree of orientation decreasing outward as the ulative effect of thermal movement becomes greater (105). Macey (68) pointed out difficulties encountered by this concept, particularly in view of the facts that the clay-mineral surface is not a uniformly charged plane, and

that the water molecules do not act strictly as little rods with positive and negative ends.

There are many concepts of the structure of a water molecule, but the one proposed by Bernal and Fowler (14) and modified by Morgan and Warren (81) is probably the most acceptable (64). According to Bernal and Fowler (14), the water molecule consists of a V-shaped arrangement of the atomic nuclei, the internuclear O-H distances being 0.96 $\overset{o}{A}$ and the internuclear angle being 103 to 106 degrees, which is very close to the tetrahedral angle of 109 degrees. In the molecule there are four regions where the density of the outer electrons is maximal. Two of these regions are associated with the OH bonds and coincide with the position of the protons; the other two are associated with lone pairs of electron and are located above and below the plane of the atomic nuclei on the opposite side of the oxygen nucleus from the proton. Therefore, the net charge distribution of the water molecule resembles a tetrahedron with two positive and two negative corners. The resultant positive center midway between the protons is separated from the resultant negative center near the oxygen nucleus on the side next to the protons. Hence the water molecule has a dipole moment (14).

At temperatures below 0°C, water molecules tend to occur in fixed positions in an ice lattice. For this reason it is possible to determine their molecular arrangement by means of X-ray diffraction, which shows that each molecule is tetrahedrally coordinated to four others and that the oxygen nuclei are 2.76 $\overset{o}{A}$ apart (94,95). Ockman (88) showed by using infrared and Raman spectra that the hydrogen atom is not midway between

the oxygen atoms of the bonded molecules, but is 1.00 Å from one oxygen atom and 1.76 Å from the other; thus the individual water molecules retain their identity and are held together by hydrogen bonds. Therefore, in an assembly of water molecules, there is a tendency for each molecule to be hydrogen-bonded to four neighboring water molecules which surround it tetrahedrally (88).

When ice melts there is an increase in density from 0.917 for ice to nearly 1.000 for water. The magnitude of this density increase is very revealing in that if all of the hydrogen bonds were broken in the process of melting, water would have a close-packed arrangement, i.e., each water molecule would be in close contact with twelve others. Then, provided the molecular radius remained at 1.4 Å, it would have a density of 1.84. Conversely, for a density of 1.00 the molecular radius would have to be 1.72 Å (14). In the words of Bernal and Fowler (14), "We have therefore the choice of assuming either that water is a simple close-packed liquid in which the effective molecular radius has changed from 1.4 Å in the solid to 1.72 Å in the liquid, or that the radius is still approximately 1.4 Å but that the mutual arrangements of the molecules are far from that of a simple liquid." The X-ray evidences of Morgan and Warren (81) indicate that the latter is correct. It appears that liquid water retains a high degree of hydrogen bonding and that this bonding decreases with increasing temperature. It has been concluded that the structure of water must be similar to that of ice at least for short distances, or perhaps it may be stated that water has a loose ice-like arrangement or, in the terminology of Morgan and Warren, water has a "broken down ice structure."

Hence, not only is the radius of the water molecule nearly the same as in ice, but the structure of water partly resembles that of ice (81).

The surface of clay mineral is made up of either oxygen atoms or hydroxyl groups arranged in a hexagonal pattern which can superimpose a similar pattern in a hydrogen-bonded water structure (37,49,68). In the model of Hendricks and Jefferson (49), a water layer is composed of water molecules joined into hexagonal groups of an extended hydroxyl net as shown in projection in Figure 1. Each side of the hexagon must correspond to a hydroxyl bond, the hydrogen bond of one water molecule being directed toward the negative charge of a neighboring molecule. One-fourth of the hydrogen atoms, or one hydrogen atom of half of the water molecules, are not involved in bonding within the net (K, M and O of Figure 2). The net is tied to the surface of the clay minerals by the attraction between those hydrogen atoms not involved in bonding within the net and the surface oxygen layer of the clay-mineral units (Figure 2 and 3) (49). Because of the dipole character of the water as well as the lattice characteristics of the clay mineral surface, water molecules are joined by hydrogen bonding into groups of extended hexagonal networks. By assuming a 3.0 $\overset{o}{A}$ separation of oxygen, such a water network as $\underline{a}$ and $\underline{b}$ dimensions of the clay minerals, and every other water molecule in the net has one hydrogen available for bonding to an oxygen of the clay mineral surface. Successive hexagonal nets might build up on one another and are hydrogen bonded to one another. This hypothesis leads to a laminar stacking of hexagonal water molecule network with a vertical separation of 2.76 $\overset{o}{A}$ for each layer. In this configuration each water molecule
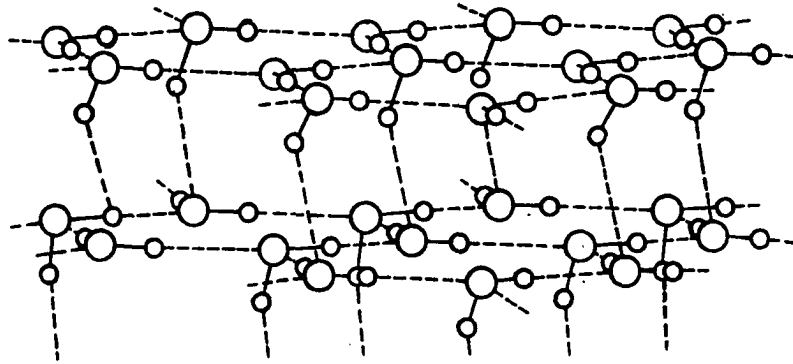
Figure 1. Configuration of water adsorbed directly adjacent to the basal plane surfaces of the clay minerals (after Hendricks and Jefferson, 49)

○ Oxygens
○ Hydrogens in plane of oxygens
● Hydrogens below plane of oxygens
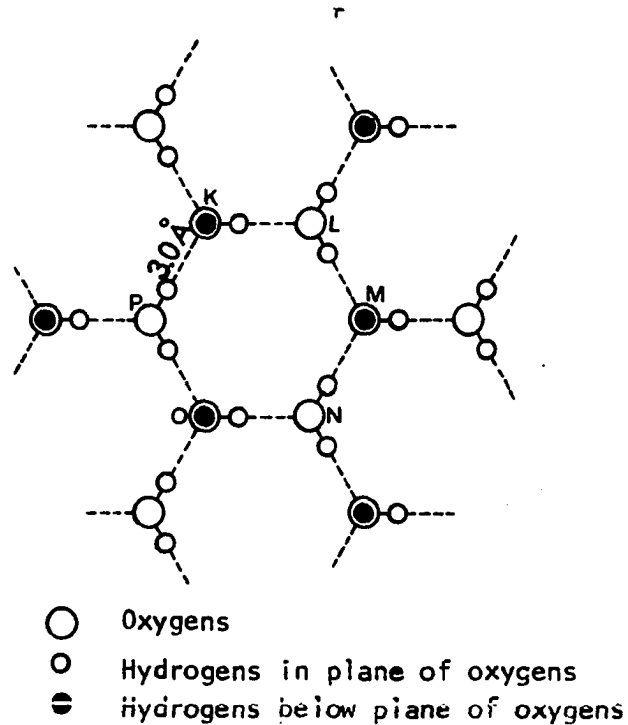
Figure 2. Arrangement of oxygens and hydrogens in a water net (after Hendricks and Jefferson, 49)

Silica layer of
clay mineral

Oriented water
molecules

Silica layer
of clay mineral
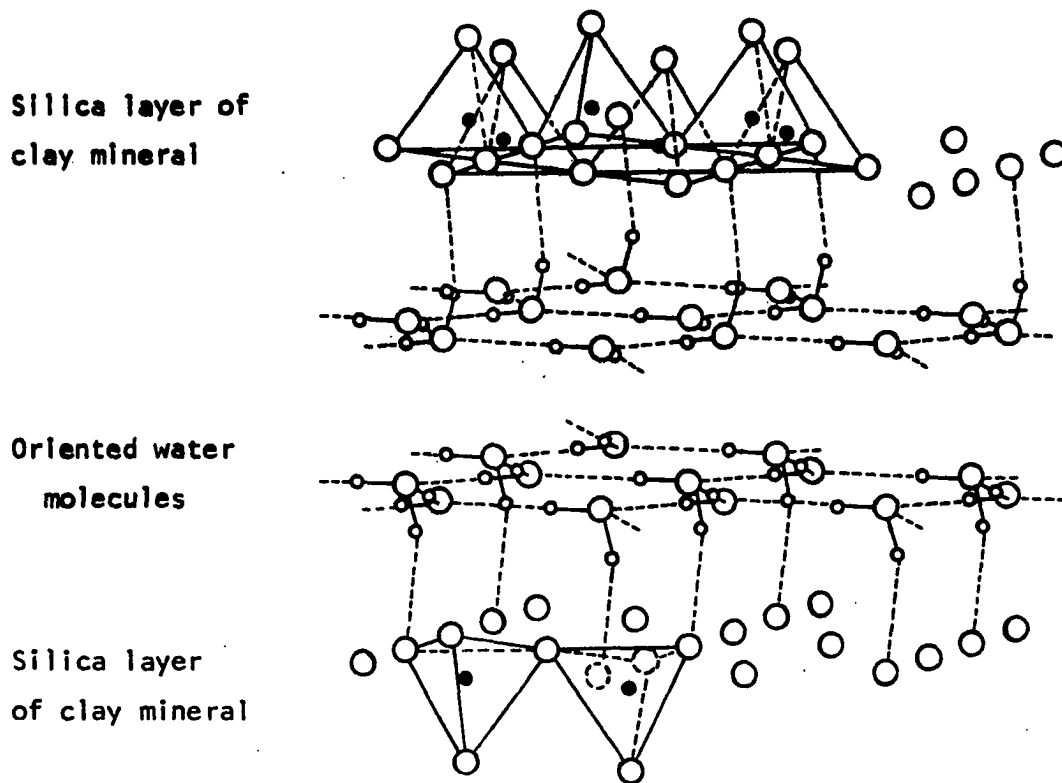
Figure 3. Configuration of the water net proposed
by Hendricks and Jefferson, showing the
binding through hydrogens to the adjacent
clay-mineral surfaces (after Hendricks
and Jefferson, 49)

In a monomolecular layer occupies an area of about 11.5 Å^2.

A second mechanism by which water may be attracted to a clay surface is hydration of exchangeable cations. Since the cations are attracted to the negatively charged surface, so is the water of hydration. Low (64) suggests that this mechanism of attracting water should be most important at low water contents, and at high water contents, exchangeable cations should still play a role in clay-water interaction. At high water contents the exchangeable cations tend to dissociate from the surface and are regarded as being in solution.

Macey (68) postulated that the initially adsorbed water has the structure of ice. He considered that it fits on top of the oxygen net of the basal plane of the three-layer clay minerals as shown in Figure 4. The fit of the water molecules with the oxygen net as suggested by Macey (68) is different from that suggested by Hendricks and Jefferson (49) in that the distribution of water molecules is not planar. In the clay interlayer oxygen surface, the oxygen atoms are 4.51 Å apart, whereas according to the Macey concept, the oxygens of the basal plane of ice are 4.52 Å apart, and the packing would be even looser than that suggested by Hendricks and Jefferson (49). Macey suggested that the ice structure develops on clay mineral surfaces with the hexagonal molecular configuration of the basal plane of ice. This structure tends to build outward from the surface. In the Hendricks and Jefferson concept, the ice structure is stretched so that the offset water molecules come into the same plane and there is no change in the hydrogen bonding.

Forslind (37,38), on the basis of electron-diffraction data, suggested
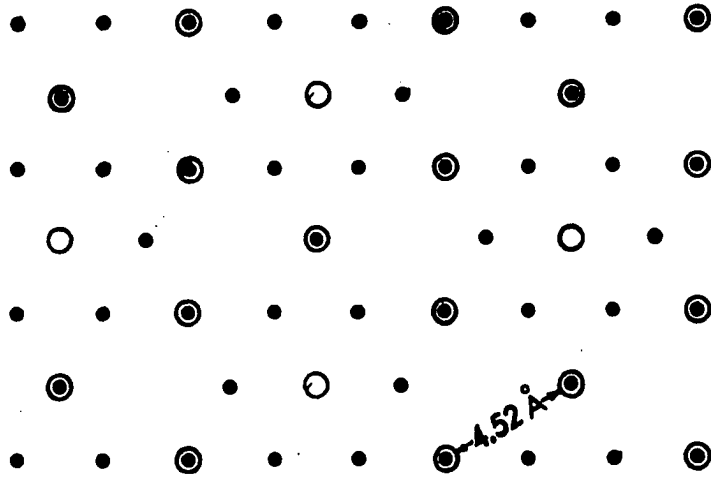
Figure 4a. Superposition of the ice lattice on the surface
oxygen layer of the clay minerals (after Macey, 68)
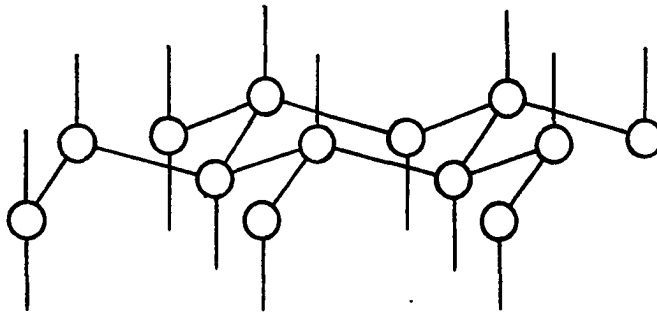
• Oxygen layers forming surface of silicate

◯ Oxygen atoms of ice

Figure 4b. Structure of ice

the same ice structure arrangement postulated by Macey but based his argument on the Edelman-Favejee structure (66, p. 152) rather than the Hofmann-Endel-Wilm structure of montmorillonite (66, p. 146).

Demirel (33) presented two ways in which the ice structure may develop in the interlayer regions. One would be to stack the hexagonal rings in the way they successively occur in the quartz-like structure of ice. This would cause an alternating platelet separation of 2.76 Å and 0.92 Å with successive molecular layers of water. In the second method the first hexagonal network is shared by two montmorillonite platelets causing a separation of 2.76 Å; two hexagonal networks are stacked and held by the two silica surfaces causing a separation of 5.52 Å; the third and fourth molecular layers of water fill in between the hexagonal networks forming tetrahedrons with the water molecules of the network. A complete unit cell of ice is formed with the entrance of the fourth molecular layer of water, causing a separation of 7.36 Å. The fifth and sixth layers of water enter between the unit cell of ice and the clay surfaces, forming hexagonal networks and causing separations of 10.12 Å and 12.88 Å, respectively. Demirel (33), using data reported in the literature and his own for various species of homoionic montmorillonites, found evidence to support the build-up of an ice structure in the second way. With an ice structure, the area covered by a water molecule is about 17.5 Å^2.

Barshad (9) suggested another concept of the nature of the adsorbed water, on the basis of careful dehydration determinations. According to him, at very low states of dehydration for montmorillonite, the water

molecules tend to form tetrahedrons with the oxygen of the top layer of the linked silica tetrahedrons of the lattice. This type of packing would give rise to hexagonal rings of water molecules which are similar to the hexagonal rings of oxygens on the vertices of the linked silica tetrahedrons of the individual silicate sheets. In Figure 5, $\underline{a}$ to $\underline{f}$ represent such water molecules forming tetrahedral units with oxygens of the underlying silica tetrahedral network. The packing in this configuration would be loose, as there would be only four molecules of water per unit cell per molecular layer, and the height added for a single layer of water molecules would be 1.78 Å, according to Barshad. At higher states of hydration the water adsorbed by montmorillonite tends to form hexagonal rings of water molecules; these are similar to the hexagonal rings of the oxygens of the montmorillonite basal plane which forms the bases of the linked silica tetrahedrons. In Figure 5, $\underline{1}$ to $\underline{6}$ represent such water molecules. In this configuration the packing is more dense, and there are six molecules of water per unit cell per layer of water molecules. The height added for a single layer would be about 2.55 Å, since the water molecules would be directly superimposed on the oxygens (9).

None of these suggested configurations take into account a "kinking" of tetrahedral clay layers into a distorted hexagonal arrangement, which accounts for the changes in $\underline{a}$ and $\underline{b}$ dimensions with ionic substitutions in the octahedral clay layer (18). This appears pertinent to a recent finding of Ravina and Low (96) that the b-dimension also changes with varying degree of hydration, tending to expand as the clay hydrates,
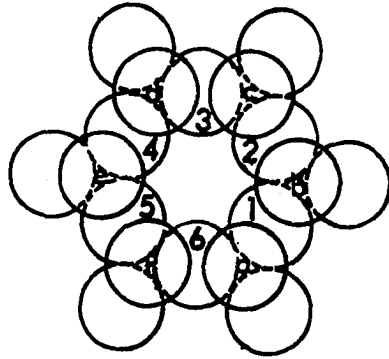
Figure 5. Arrangement of water molecules in the
interlayer space of montmorillonite and
vermiculite (after Barshad, 9)

suggesting an "unkinking" of the clay tetrahedron.

Adsorption Method to Determine the Surface Area of Sodium Montmorillonite

In 1938 Brunauer, Emmett, and Teller (22,25) developed the multi-molecular adsorption (BET) theory under the following assumptions:

a. The same forces that produce condensation are also chiefly responsible for the binding energy of multimolecular adsorption.

b. The first adsorbed layer is attracted strongly by the surface, the second layer essentially not by the surface but by the first adsorbed layer, and the adsorption thus propagates from layer to layer. Their derivation is a generalization of the Langmuir treatment of unimolecular adsorption and is based on a detailed balancing of forward and reverse rates of reaction (22). BET theory seems to be the most acceptable one for the study of adsorption of vapor on a solid surface (32).

A direct method for the determination of the surface area of a powdered solid from the adsorption isotherm plot for a gas or vapor has been suggested by Brunauer, Emmett and Teller (25) on the basis of their multimolecular theory. When the weight or volume of a gas or vapor adsorbed on a solid surface at standard temperature and pressure is plotted on the ordinate axis versus the relative pressure of the gas or vapor on the abscissa axis, a typical S-shaped curve is obtained, called an S-shaped isotherm. Brunauer et al. (25) found from many experiments that all substances except charcoal gave typical S-shaped isotherms, the low pressure portion of the isotherm being concave to the pressure axis, the higher pressure region convex to the pressure axis, and the inter-mediate region approximately linear with respect to pressure. The

beginning of the approximate linear portion of the experimentally de-
termined low-temperature adsorption isotherms is believed to correspond
to the covering of the surface of the adsorbent by a complete uni-
molecular layer of adsorbed gas. The specific surface of the solid
covered with a monomolecular layer of the vapor then may be calculated
by a formula as,

$$\Sigma = \frac{N_A q_m s}{M} \qquad (1)$$

where N_A is Avogadro's number, M is the molecular weight of the adsorbate,
s is the area of an adsorbated molecule, and q_m is the mass adsorbed at
monolayer coverage at the adsorbent surface, expressed per gram of the
adsorbent. Assuming that the adsorbed molecules have the same packing
on the surface as the molecules of the liquified or solidified gas have
in their plane of closest packing, we can obtain for the area covered by
a molecule:

$$\text{Area } s = 4(0.866) \left(\frac{M}{4\sqrt{2}\ N_A \delta}\right)^{2/3} = 1.091 \left(\frac{M}{N_A \delta}\right)^{2/3} \qquad (2)$$

where δ is the density of the solidified or liquified adsorbate. The co-
efficient 1.091 is called, by Brunauer (22), the packing factor; its
value for an adsorbate may vary from one adsorbent to another depending
on the packing and on the variation of adsorbent pores (63). In the case
of water adsorption on any adsorbents, the densities of the liquified and
solidified water differ by nearly 10 percent. Hence Equation (2) can not
be significantly more precise than $\pm$ 5 percent. It is therefore

inappropriate to give the "packing factor" to 0.1 percent for the water adsorption on clay minerals. The packing factor for water adsorption on clay minerals can be in the limit of 1.1. Equation (1) can be used to determine specific surface areas of adsorbents if the cross-sectional area of the adsorbate molecule is known; or it can be used to determine the area occupied by an adsorbate molecule if the specific surface is known. Using nitrogen as an adsorbate, Emmett et al. (36) obtained specific surface areas of soil colloids ranging from 41 to 71 m^2/gm. Hendricks, Nelson and Alexander (50) investigated the effect of various chemisorbed cations on the adsorption of water by the clay mineral montmorillonite. The different samples of montmorillonite had the same specific surface areas and same number of equivalent weights of positive ions adsorbed, but differed from each other with respect to the nature of the positive ions. It was found that the adsorption of water at equal relative pressures depended strongly on the nature of the positive adsorbed ions, particularly at low relative vapor pressures. Brunauer (22, p. 357), using the water adsorption data of Hendricks et al. (50), obtained a specific surface of 400 m^2/gm for montmorillonite. Zettlemoyer et al. (120) used ammonia adsorption on Wyoming bentonite and obtained a value of 556 m^2/gm; they obtained 34.5 m^2/gm with nitrogen as an adsorbate. Mooney et al. (79) used water desorption data to obtain values of about 800 m^2/gm for sodium and hydrogen montmorillonites, but could not obtain similar values during a later study (80). Goates and Hatch (44) found a value of 303 m^2/gm with water adsorption on montmorillonite. Orchiston (91) obtained 336 m^2/gm with water vapor and sodium saturated

montmorillonite. Johansen and Dunning (55), with sodium montmorillonite, get 38 m^2/gm with nitrogen, 203 m^2/gm with water vapor adsorption data and 250 m^2/gm with water vapor desorption data. All of the areas mentioned above were based on closest packing of the adsorbate on the clay surfaces. The large differences between values determined with nitrogen and those for ammonia and water vapor are attributed to the ability of the latter to penetrate between montmorillonite layers while nitrogen covers only the external surfaces (7,79). The underlying assumption of closest packing of the adsorbate may be pertinent since the specific surfaces obtained from ammonia and water vapor sorption data, except for the one determination by Mooney et al. (79), were substantially less than that calculated from crystallographic data. The value of specific surface area calculated from crystallographic data is 748 m^2/gm. This calculation is shown in Appendix I. The variations of specific surface areas obtained from the past investigations (44,55,91) will be discussed in more detail on page 117 of this report.

Surface Free Energy Change Due to Adsorption

Bangham (5) was the first to show that the Gibbs adsorption equation could be used to determine the free energy changes that occur during adsorption of vapor on solid surfaces. Others (15,53) have used Gibbsian methods to show that the free energy of immersion of a solid surface in saturated vapor can be calculated from vapor adsorption data. Jura and Harkins (58) showed that the formulas given by those investigators (15,53), when expanded, are identical to that of Bangham.

Boyd and Livingston (15) have shown that if the adsorption isotherm

for a vapor on a crystalline nonporous powder is obtained and if the specific surface area determined by the BET method (25) is employed, the change in free energy of a clean solid surface upon immersion in a saturated vapor can be calculated. Using the Gibbs adsorption equation, Boyd and Livingston (15) derived an equation for the free energy of immersion of a nonporous wettable surface in a saturated vapor. It can be made to read:

$$\Delta F = (\gamma_{sl} - \gamma_{so} + \gamma_{lv}) = - \frac{RT}{M\Sigma} \int_{o}^{P_o} \frac{q}{p} \, dp \tag{3}$$

where γ_{sl} is the solid-liquid interfacial tension, γ_{so} the surface tension of the solid in vacuum, γ_{lv} the surface tension of the liquid in contact with its own vapor, q is the mass of the vapor adsorbed by a unit of solid at pressure p, and R, T, M, Σ and p_o are the gas constant, absolute temperature, molecular weight of the vapor, specific surface of the solid and the saturation pressure, respectively.

Demirel (33) has presented a somewhat simpler derivation based on thermodynamics, by considering that when a vapor at pressure p is in equilibrium with an adsorbed layer, the differential free energy change involved is isothermal transfer to one mole of saturated vapor onto a solid surface of unit area is equal to the difference between the chemical potential of the vapor at pressure p and at saturation pressure p_o. The transfer involves the compression of the vapor, and the expansion of the adsorbed layer. He further pointed out that by substituting $p_o d(p/p_o)$ for dp, the expression may be changed to the following:

$$\Delta F = - \frac{RT}{M\Sigma} \int_o^1 \frac{q}{p/p_o} \, d(p/p_o) \qquad (4)$$

which is a more convenient form to use when relative vapor pressures are employed.

The value for ΔF, the free energy change accompanying the process of transferring the saturated vapor onto a unit area of solid surface, can be calculated from Equation (4). This transfer is completed when the equilibrium relative vapor pressure p/p_o equals unity. Boyd and Livingston (15) and Jura and Harkins (58) recommended graphical integration of this equation as a simple and accurate means of determining ΔF. Boyd and Livingston (15) and Jura and Harkins (58) calculated the free energy change by extrapolating the adsorption isotherm to saturation pressure with the assumption that no capillary condensation occurs. They make a correction which amounts to subtracting the surface tension of the liquid (γ_{lv}) from the equation for ΔF for obtaining the free energy of wetting, which presumes a zero contact angle. However, Craig et al. (30) have pointed out that this method leads to difficulties for nonporous powders because it is not possible to accurately extrapolate the adsorption isotherm to a definite limiting value, and a "nonporous" powder acts as a porous solid so that large numbers of capillary spaces are actually formed due to particle-to-particle contacts. The main difference in behavior between porous and nonporous solids is that during adsorption of a vapor on a porous solid, the solid-vacuum interface is replaced by a liquid-vapor interface and a solid-liquid interface, and at $p/p_o = 1$

because of filling of the pores, the liquid-vapor interface is completely destroyed. In the case of a vapor on a nonporous solid, the area of the liquid-vapor interface at $p/p_o = 1$ is not destroyed, and the area is considered to be essentially equal to that of the solid-vacuum interface (30). The assumption of no capillary condensation, and the steepness of the adsorption isotherm near the saturation pressure, introduce uncertainties in the determination of the free energy of immersion by the subtraction of the surface tension of liquid (γ_{lv}) from ΔF. For these reasons and because of the porous nature of clay minerals, the free energy of immersion in the bulk liquid (the free energy of adsorption) was calculated directly from Equation (4) by graphical integration of the q versus p/p_o plot.

If the adsorbent is a noninteracting fine particle wettable by the liquid, capillary condensation in the contact zones of the particles would theoretically fill the voids with the liquid before final saturation is attained. In these cases, the change in free surface energy may be calculated by equation

$$\Delta F = (\gamma_{sl} - \gamma_{so}) \qquad (5)$$

where ΔF would be the free energy of immersion of a unit area of solid surface in a bulk liquid. Craig et al. (30), Dobay et al. (34), and Fu and Bartell (42) concur in this viewpoint. The free energy of immersion in the bulk liquid was then calculated directly from Equation (4) by graphical integration.

If the material being investigated consists of interacting solid

particles, Hirst (51) and Demirel (33) independently have shown that Equation (5) must be modified by introducing a term representing the particle interaction. If the solid powder adsorbent has a rigid structure, ΔF as given by Equation (4) is equal to that expressed by Equation (5). When the adsorbate penetrates into the interstices of interacting solid surfaces and causes a separation against the forces of interaction, Equation (5) may be modified as given by Demirel (33):

$$\Delta F = (\gamma_{sl} - \gamma_{so}) + \alpha\Delta V \tag{6}$$

where α is the interstitial surface area per cm^2 of total surface and ΔV is the free energy change per cm^2 of the interstitial surface due to separation of particles against the force of interaction (92, p. 253). Therefore, with clay minerals the free energy change given by Equation (4) is equivalent to that expressed by Equation (6). The term $(\gamma_{sl} - \gamma_{so})$ will be called the free energy of immersion of the solid in the liquid and ΔF the free energy of wetting of the solid by the liquid.

Brunauer (22) states that "the term physical adsorption may be defined as the disappearance of molecules from the gas phase and the remaining of these molecules attached to the surface of the solid and there held in place by a weak interaction between the solid and the gas" (22). Physical adsorption takes place spontaneously. The process can be reversed and the adsorbate may be removed by lowering the pressure and is then recovered unchanged chemically (1). Other terms associated with physical adsorption are low temperature adsorption, secondary adsorption, and capillary condensation.

According to Adamson (1), atoms or molecules constituting a solid
are held together by different forces: van der Waals or ionic forces or
chemical bonds are involved. Whatever the nature of these forces, an
atom located within the body of the solid is subjected to balanced forces
in all directions or it would move out. At the surface of a solid the
chemical bonding interactions are not balanced as they are in the interior
of the solid, resulting in a surface energy or surface tension. The
tendency of a solid surface to interact is partially satisfied by the
adsorption of molecules of a gas, and therefore adsorption on a clean
surface occurs with a decrease in the free energy of the system.

Expansion and Swelling of Montmorillonite

Several investigators have studied the expansion of montmorillonite
upon adsorption of water between the clay layers. Nagelschmidt (82)
showed that there was apparently a continuous variation of the basal
spacing with water content. Bradley, Grim and Clark (17) found that water
molecules are adsorbed in monomolecular layers between the clay layers.
From studies with oriented samples they found no evidence of a gradual
swelling but rather a series of apparently definite and discrete hydrates.
Hendricks et al. (50) reported that basal spacing varies continuously but
not uniformly with water content; this variation and nonuniformity result
from an averaging effect from a lattice containing various numbers of
water layers in different parts. Mering (74) found that the formation of
discrete monomolecular layers of water does not hold precisely at low
moisture contents when the adsorbed ion hydrates, e.g. Ca^{++} or Mg^{++}; for
sodium montmorillonite hydration seemed to occur by complete molecular

layers. Mooney et al. (79) used the data of Hendricks et al. (50) and their own to show a stepwise uptake of interlayer water with increasing humidity; however, they disregard much of the data of Hendricks et al. (50). Gillery (43) found that well-defined hydrates exist over certain ranges of vapor pressure and that between these ranges mixed layers of the hydrates predominate. From the studies mentioned above, and others (33,76), it has been quite well established that the separation of clay layers is due to the adsorption of integral molecular layers of water; the apparently continuous change in observed basal spacings results from random alteration of layers at various spacings. However, the relationship between relative humidities and layer separation is not well defined; data reported for homoionic, e.g., sodium, montmorillonite shows considerable variations (33,43,50,76,80).

Barrer and McLeod (7) investigated the sorption of nonpolar and of polar gases and vapors on sodium montmorillonite and have shown that the nonpolar species are not intercalated, but the polar molecules may be. Many workers (50,74) found that the interlayer swelling does not proceed beyond 20 $\overset{o}{A}$ for calcium montmorillonite. Mering (74) concluded that crystalline swelling for sodium montmorillonite ceased at 20 $\overset{o}{A}$ when the first order basal spacing became very diffuse. In contrast to this observed crystalline swelling, sodium montmorillonite will swell to twenty times its own volume in water. He also has shown that almost all the macroscopic swelling in montmorillonite takes place at water contents equivalent to a relative humidity of greater than 99 percent. To control the water content and measure the X-ray spacing in this range by direct

methods would involve very precise temperature control (74).

Norrish and Quirk (86) postulated from the result of their study that swelling of montmorillonite takes place in two rather distinct ways. First, below 22 Å the interlayer expansion is stepwise and very dependent on the exchangeable cation. For monovalent cations the number of water layers taken up is directly related to the hydration energy of the cations. Secondly where expansion occurs to greater than 35 Å it is continuous and independent of cation for monovalent cations. In this region montmorillonite is probably developing a diffuse double layer and behaving as a colloid. The swelling is then essentially osmotic and is expected to be independent of cation for ions of the same valence. The sudden jump in spacing from about 20 Å to about 40 Å is interesting and is probably associated with reversal of the force due to the charge on the montmorillonite sheets. At low spacings the force will be electrostatic and attractive, as in mica, whereas at high spacings the charge will result in a repulsive (osmotic) force. At high spacings this repulsive force is presumably balanced by van der Waals-London attractive forces. Norrish (84) also observed more or less diffuse equilibrium of the unit layers in swollen flakes by montmorillonite clays in contact with electrolyte solutions. These spacings decrease with increasing electrolyte concentrations in a range between about 130 to 19 Å. An evaluation of the unit layer interaction forces and energies shows that the double-layer repulsion forces cannot be cancelled by van der Waals attractive forces at each equilibrium distance without making unrealistic assumptions. Van Olphen (111) considered the attractive forces with special emphasis

on the cross linking of stacks of parallel layers by a relatively small number of nonparallel plates. Most investigators (84,114,115) studied the swelling pressure of montmorillonite paste. The spacings of the clay particles are in the range of 20 to 200 $\overset{o}{A}$. The swelling pressure of montmorillonite at equilibrium spacing below 20 $\overset{o}{A}$ is not well investigated. One purpose of this study is to investigate the swelling pressure in the range of 10 to 20 $\overset{o}{A}$.

MATERIALS

Sodium Montmorillonite

The sodium montmorillonite used was prepared for earlier investigations and the method of preparation has been described in detail elsewhere (33,97). A commercially available Wyoming bentonite, produced by the American Colloid Company and known by the trade name Volclay-SPV, was used. According to the producer it consists of 90 percent montmorillonite, essentially sodium montmorillonite, and 10 percent other materials such as feldspar, quartz and volcanic glass. The Volclay-SPV was cleansed of coarse grained impurities by a repeated (12 times) sedimentation process. An X-ray diffraction pattern from a dried sample of the suspension after the last sedimentation is shown in Figure 6.

Sodium montmorillonite was prepared from the purified bentonite by mixing a saturated sodium chloride solution with the suspension obtained from the sedimentation process. This mixture was stirred for 24 hours and the clay was then separated by means of a super-centrifuge. This process was repeated five times to assure replacement by sodium ions of all the cations associated with the montmorillonite. The free electrolyte was removed from the sample by dispersion in distilled water and centrifuging. This was repeated several times until the material was free of chloride ions. The physical and chemical properties were determined by standard procedures and are represented in Table 1.

Purified Volclay-SPV

2θ, degrees

3.2   3.5   4   5   6   7   8   9   10   15   20   30   40   ∞

d, Å
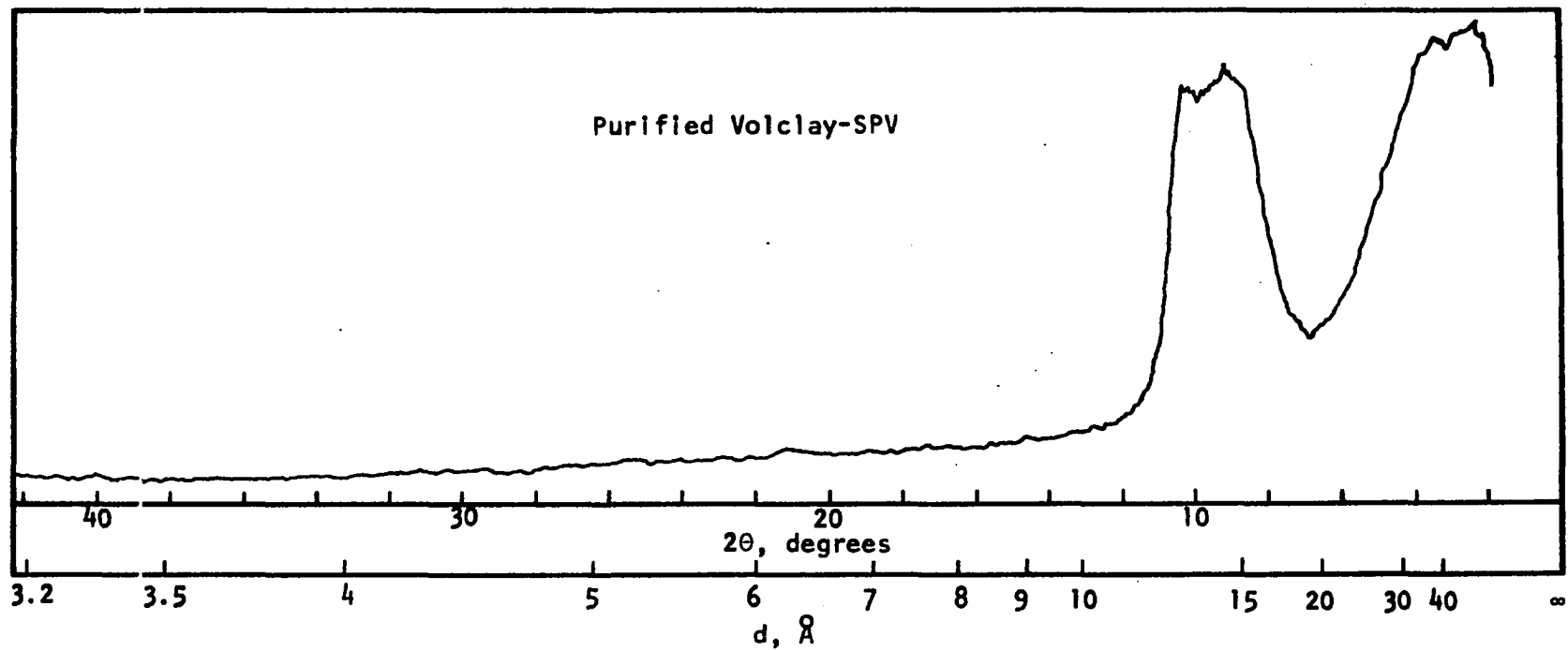
Figure 6.   X-ray diffraction chart of purified Volclay-SPV obtained by using filtered
chromium radiation (after Demirel, 33)

Table 1. Properties of the sodium montmorillonite

Physical and chemical properties	
Physical properties	
Liquid limit, %[a]	968
Plastic limit, %[b]	51
Plasticity index, %	917
Shrinkage limit, %[c]	17
Centrifuge moisture equivalent, %[d]	882
Chemical properties	
Cation exchange capacity, me/100 gm[e]	94
pH[f]	7.55

[a]ASTM Method D 423 - 61T.

[b]ASTM Method D 424 - 59.

[c]ASTM Method D 427 - 61.

[d]ASTM Method D 425 - 39.

[e]Ammonium acetate method.

[f]Glass electrode method using suspension of 1 gram of soil in 30 c.c. of distilled water.

Distilled Water

Distilled water used for preparation of the sample was obtained from a steam operated SLH-2 Barnstead still which produces, when fresh, practically carbon dioxide-free water with a pH approaching 7. For the adsorption experiments this distilled water was triple distilled just before introducing into the apparatus.

TESTING EQUIPMENT

High Pressure X-ray Goniometer Accessory

This accessory attached to an X-ray diffractometer was used to investigate first order basal spacing of sodium montmorillonite while under pressure. The apparatus was designed and initially tested by Olson (89). It is shown in Figure 7 and consists of the following major components: (a) body or cylinder, (b) end plate, (c) nose plate, (d) piston, (e) porous plug assembly, (f) compression spring, (g) steel ball, (h) beryllium window, (i) pedestal, (j) dovetail, (k) rotatable base, (l) fixed base, (m) and (n) adjusting screws, (o) quick-connected hydraulic coupling, (p) standpipe, (q) brass gasket and (r) thumb screws. Detailed drawings of the high pressure X-ray goniometer accessory appear in Olson's thesis (89). The fixed base of the accessory was designed to mount to the goniometer of a General Electric diffractometer.

Figures 8a and 8b show the complete system which includes (a) high pressure goniometer accessory, (b) flexible pressure hose of 0 - 10,000 psi capacity manufactured by Enerpac Test Systems, Butler, Wisconsin, (c) 10:1 ratio pressure intensifier using carbon dioxide gas on the low pressure side and hydraulic oil on the high pressure side, (d) 0 - 10,000 psi high range pressure gage (100 psi divisions), (e) 0 - 200 psi low range pressure gage (2 psi divisions), and (f) 10,000 psi cut-off valve. The maximum pressure range limited by the hydraulic system is about 5000 psi due to the O-rings used in the high pressure chamber. The maximum pressure that the beryllium window can sustain, according to the specifications of the manufacturer (Kawecki Berylco Industries, Inc.,

Figure 7. High pressure goniometer accessory (after Olson, 97)

NO.	DESCRIPTION	QUAN. REQ'D
1	BACK PLATE	1
2	1/4-20 UNC-2x1-1/4 CAP SCREW	1
3	1-3/8 I.D.x1-5/8 O.D. RUBBER "O" RING	1
4	3/4 O.D. HELICAL COMPRESSION SPRING	1
5	CYLINDER	1
6	PISTON	1
7	3/4 I.D.x1 O.D. RUBBER "O" RING	1
8	5/16 DIA. STEEL BALL	1
9	POROUS PLUG ASSEMBLY	1
10	0.005" BRASS GASKET	1
11	BERYLLIUM WINDOW	1
12	EDGE PLATE	1
13	3/8-16 UNC-2x1 SHOULDER SCREW	2
14	0.250 DIA. LOCATING SCREWS	2
15	PEDESTAL	1
16	#10-24 UNC-2x1-1/4 CAP SCREW	1
17	FIXED BASE	1
18	MOVEABLE BASE	1
19	TRANSLATIONAL ADJ. SCREW	1
20	TRANSLATIONAL ADJ. SCREW SUPPORT	1
21	ELASTIC NUT	1
22	TEFLON WASHER	4
23	DOVETAIL	1
24	#10-24 UNC-2x1/2 CAP SCREW	1
25	1/4-20 UNCx3/4 HD'LESS DOG PT. SET SCR.	1
26	ROTATIONAL ADJ. SCREW	1
27	ROTATIONAL ADJ. BRACKET	1
28	ROTATIONAL ADJ. YOKE	1

HIGH PRESSURE X-RAY GONIOMETER ACCESSORY

Figure 8a.   High pressure goniometer
            in working position
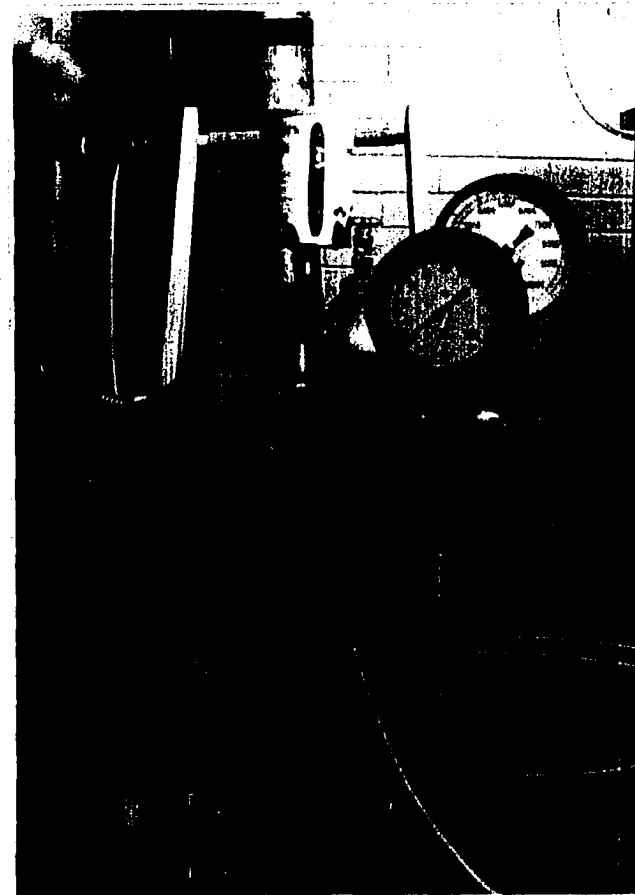
Figure 8b.   Pressure intensifier

Hazelton, Pennsylvania), is 25,000 psi. However, in this study the pressure was increased to a gage pressure of 5,000 psi, corresponding to a pressure on the beryllium window and on the sample equal to about 45,000 psi or about 3.1 kilobars. This is obtained by multiplying the area ratio of the piston to the area of the beryllium window. The area ratio of the apparatus is 9.121 and the calculation is shown in Appendix IV.

After finishing the experiment, the beryllium window was inspected and appeared to sustain no perceptible damage to its surface. The imperceptible damage of the beryllium surface may be due to the safety factor that the manufacturer provided for this product. The maximum gage pressure that the hydraulic hose can withstand is 10,000 psi and is not the limiting factor in the present system.

High-Vacuum X-ray Goniometer Accessory

The high-vacuum goniometer accessory is designed to use the same base and adjusting mechanisms as the high pressure X-ray goniometer accessory. Tapped holes are provided in the dovetail of the base to receive the pedestal of either instrument.

Figure 9 shows the essential features of the high-vacuum accessory: (a) pedestal, (b) base, (c) sample holder, (d) beryllium sleeve, (e) flanged cap, (f) connecting bolts, and (g) entry tube. Except for the beryllium sleeve, which serves as the window through which the X-rays pass, all parts are of stainless steel. The base, beryllium sleeve and flanged top were fabricated by Leemath Division of Image Systems, Long Island, New York, to the specifications of Olson (89).
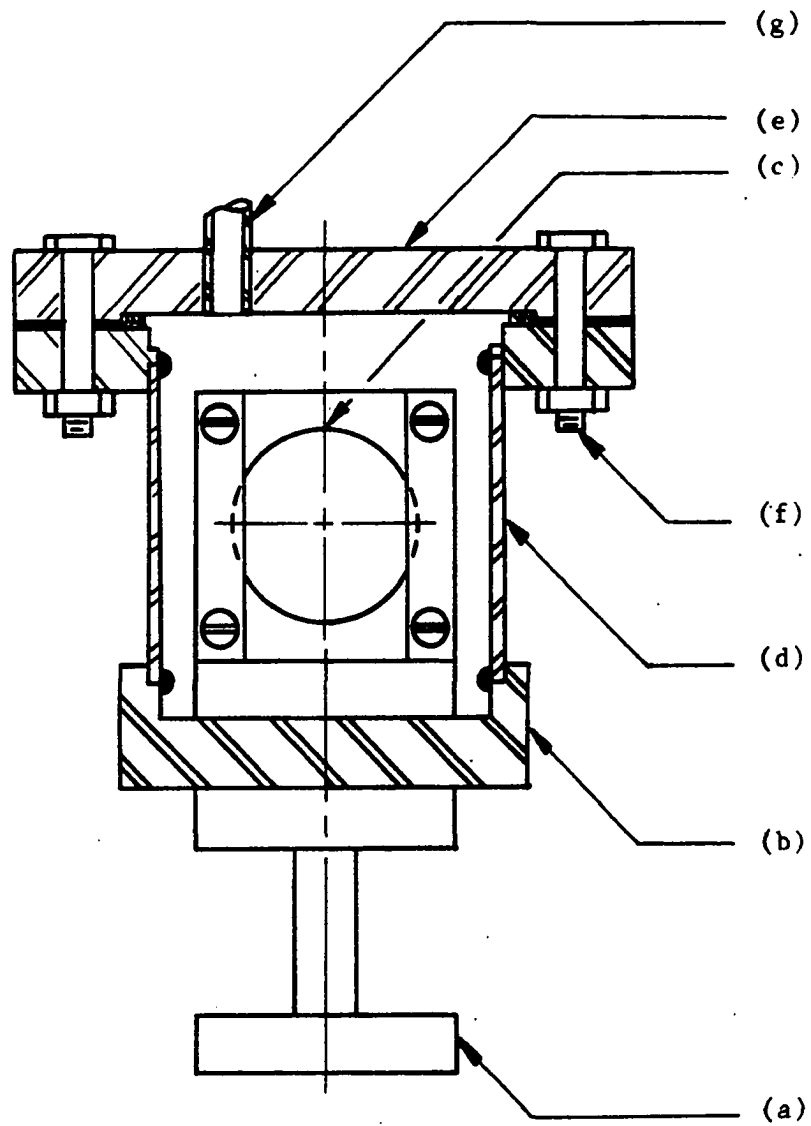
Figure 9.   High-vacuum X-ray goniometer accessory

Figure 10 shows a schematic of the entire system of which the vacuum chamber is a part: (a) mechanical vacuum pump, (b) oil diffusion pump, (c) vent tube, (d) vacuum chamber, (e) pressure sensor having 100 mm mercury capacity, (f) electronic pressure indicator, (g) pressure sensor temperature controller, (h), (i) and (j) high vacuum cut-off valves, (k) metering valve and (l) adsorbate reservoir. Items (e), (f) and (g) were manufactured by MKS Instruments, Inc., Burlington, Massachusetts.

The high-vacuum goniometer accessory is used to study the energy-volume relationships of clay-adsorbate systems using X-ray diffraction techniques while the sample is undergoing adsorption-desorption processes. From the data obtained the relationship between relative pressures and basal spacings can be drawn.
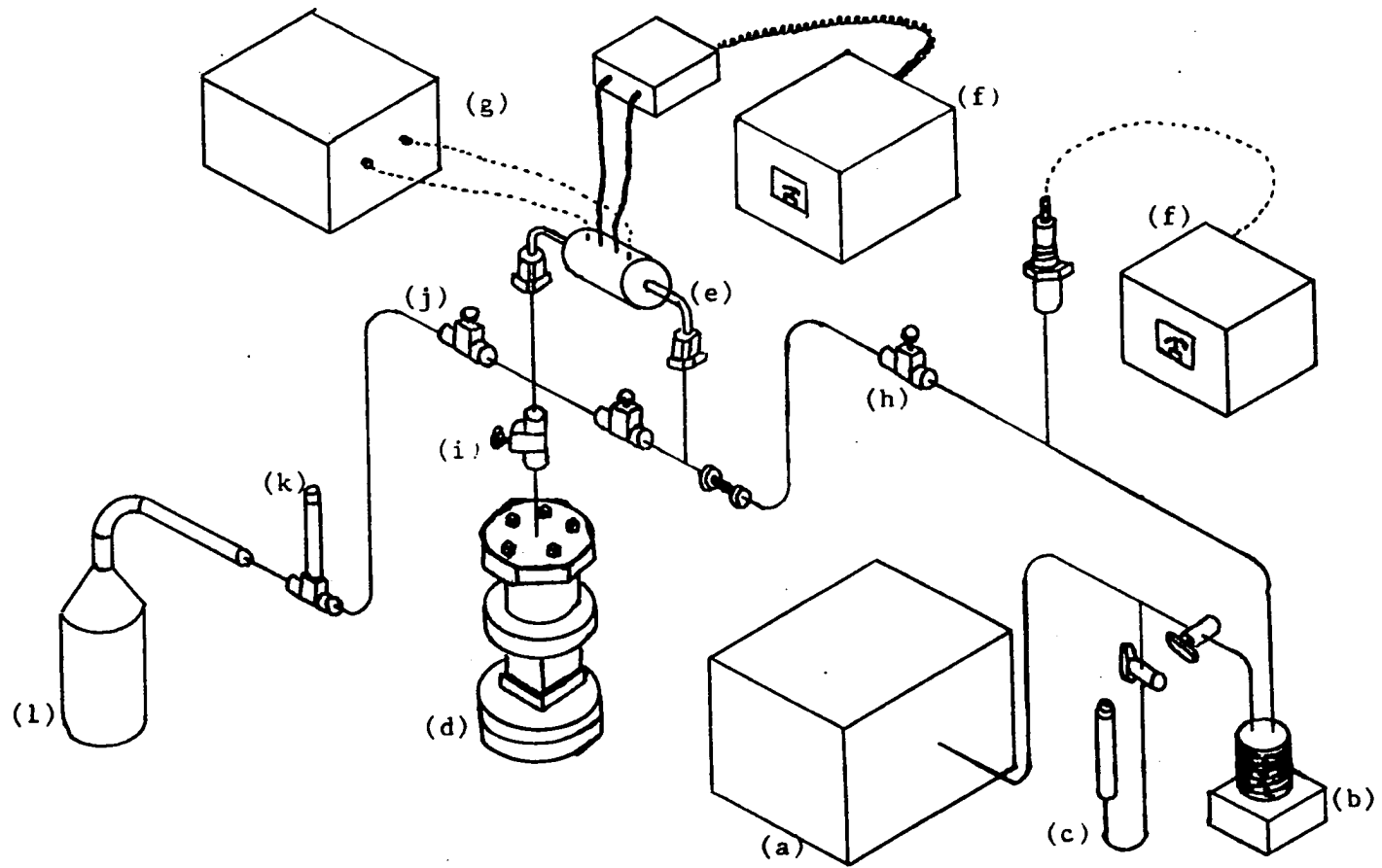
Figure 10. High-vacuum system

EXPERIMENTAL PROCEDURES

High Pressure Goniometer Accessory

The fixed base of the high pressure goniometer accessory was mounted with two screws at the central axis of the X-ray goniometer in the position normally occupied by the sample holder. The remainder of the previously assembled apparatus was then set into place upon the fixed base and the alignment of the accessory begun. The goniometer and monochromator having been previously precisely aligned following specifications of the manufacturer.

Alignment of the accessory was performed by using a piece of mica as a reference specimen. The mica sheet was cut and trimmed to fit the sample chamber of the accessory. The alignment proceeded by adjusting the screws of the goniometer accessory to achieve a maximum intensity of the diffracted beam at the value of $2\theta = 8.87$ degrees. This is the angle previously obtained from the same mica mounted in a conventional sample holder, and corresponds to a basal spacing of 9.97 Å. The copper tube used in this study is a GE model CA-8-L/Cu operated at 50 KV and 30 MA. A GE diffracted beam crystal monochromator utilizing a doubly curved LiF crystal was used in this investigation. According to Brindley (19), for clay mineral investigations, synthetic lithium fluoride is probably the most generally suitable monochromator. It is a very strong reflector and is completely stable under atmospheric conditions. The X-ray machine was run at a relatively slow scan rate of 0.4 degree per minute with a 1 degree beam slit, 0.2 degree detector slit, target-beam angle of 4 degrees, and a scintillation counter.

The adjustment of the high pressure goniometer accessory to obtain a maximum intensity of the diffracted beam at the value of $2\theta = 8.87$ degrees was performed by the following steps:

I. Rough adjustment

   a. Mount the fixed base of the accessory with the mica in the sample chamber.

   b. Set the goniometer to zero and turn on the X-ray machine. Allow 30 minutes for the X-ray tube to warm up and expand.

   c. Check the X-ray beam passing through the beryllium window with a fluorescent screen.

   d. Adjust translational screw so that the sample reduces the shadow one half.

   e. Adjust rotational screw for maximum shadow width.

   f. Repeat steps d and e until the one-half shadow width is obtained.

II. Fine adjustment

   a. Set the goniometer to the proper 2θ angle (8.87 degrees for the mica used).

   b. Adjust the translational screw for maximum intensity.

   c. Adjust the rotational screw for the maximum intensity.

   d. Repeat steps b and c until the intensity reaches its maximum value. The maximum intensity is indicated by movement of the pen on the recording chart.

After reaching the maximum intensity as described above, an X-ray diffraction test is run on the mica sample by scanning from 5 to 10

degrees; the maximum of the peak should be at 8.87 degrees.

This is the proper alignment of the goniometer pressure accessory. After alignment was completed the two knurled shoulder screws beneath the pedestal were loosened and the body (or cylinder) of the apparatus removed from its pedestal to facilitate loading of the sample. This does not disturb the alignment.

In order to load the sample into the sample chamber, the chamber was turned up and the two screws holding the nose plate in place were removed while the axis of the cylinder was vertical. The beryllium window and the 0.001 in. brass gasket were then removed, uncovering the porous nickel plug. A steel gage block with a stop at 1/16 in. depth was placed on top of the porous nickel plug and the nose plate reassembled, thereby depressing the piston and porous plug to a depth 1/16 in. below the level of the body of the apparatus, and forming the sample chamber. The porous plug was held in this position with a set screw from the side of the body and the nose plate was removed once more. The sample then was placed into the sample chamber.

The sodium montmorillonite used was mixed thoroughly with distilled water and allowed to equilibrate for about 24 hours before loading into the chamber. Loading of the sample was done by molding the prepared sodium montmorillonite paste into the chamber by the use of a spatula. After the loading operation was completed, the 0.001 in. brass gasket, beryllium window, and nose plate were assembled to the body of the device with the two nose plate cap screws. The entire assembly was remounted onto the goniometer pedestal with the two knurled shoulder screws, which

position the sample for X-rays. In order to insure that sufficient

moisture was available at all stages of the test, a plastic L-shaped

standpipe was threaded into the tapped hole formerly occupied by the set

screw and was filled with distilled water.

The high pressure hose of the pressure intensifier was bled of all

entrapped air and the hose connected at the top of the goniometer acces-

sory through the quick-connected coupling. CuK_α radiation was used to

X-ray the sample at 50 KV and 30 MA. After the X-ray spectrum of the

sample at zero pressure had been obtained, the first increment of pressure

was applied and held constant. X-raying of the sample was begun and

continued at periodic intervals until a state of equilibrium of the mont-

morillonite-water system was reached. Equilibrium was considered to

have been achieved when no further perceptible movement of the diffraction

peak occurred. This procedure was repeated after each increment of load

up to 5,000 psi gage pressure. A similar procedure was then followed

during the unloading path for each increment down to the point of zero

pressure. Minor temperature variations were found to have no effect on

the pressure readings because the CO_2 pressure regulator compensated for

pressure changes due to small variations of temperature. Thus the

pressure could be kept constant even though a temperature variation of

$\pm 1°F$ occurred. The temperature was maintained at $70 \pm 1°F$ ($21.1 \pm$

$0.6°C$).

High-Vacuum X-ray Chamber

Before mounting the specimen, the high-vacuum chamber must be aligned

in the correct position. This was done by the same procedure as for

aligning the apparatus for high pressure, again using a mica sample as reference.

Experimentation with the high vacuum accessory using water as the adsorbate was accomplished in the following manner:

a. The sodium montmorillonite sample was stirred in distilled water and the suspension dropped from a pipette onto a porous ceramic plate. The water was drained through the plate by means of suction from a vacuum pump, causing the clay particles to deposit on the plate. This was continued until a noticeable cake of montmorillonite paste was obtained. The ceramic plate was then allowed to dry in a desiccator, and placed in the sample holder within the vacuum chamber.

b. The entire system was made vacuum-tight and evacuated to 10^{-5} mm mercury with the valve (j) to the adsorbate reservoir closed. Degassing of the triple-distilled water in the adsorbate reservoir was accomplished by alternately freezing, thawing, and applying a vacuum, with valve (i) to the vacuum chamber closed. The system was degassed for about two weeks to evacuate to 10^{-5} mm mercury.

c. When the system reached 10^{-5} mm mercury pressure, water vapor was introduced into the adsorption chamber in small increments through the metering valve (k) and cut-off valve (j) during the adsorption run. Pressure readings were taken with the electronic manometer through the pressure sensor. After each increment of pressure change, the sample was repeatedly X-rayed

to determine the equilibrium first-order basal spacings. This process was continued until the saturation pressure of the adsorbate was reached at the temperature at which the test was conducted. The equilibrium was reached about 24 hours after the introduction of each pressure increment to the adsorption chamber.

d. During the desorption run, the adsorbate vapor was condensed into the adsorbate reservoir or evacuated to achieve pressure stages from saturation to the lowest pressure attainable by the system.

The temperature was controlled to be constant at 70°F (21.1°C) in this experimentation. This was achieved by using many fans to circulate the air in the air-conditioned room, and using an automatically controlled electric heater. It was found that temperature could be kept nearly constant and the change in the pressure readings was so small that it did not cause serious error for the values of relative pressure. Generally the variation in relative pressure due to temperature change was less than 0.02.

PRESENTATION AND DISCUSSION OF RESULTS

High-Vacuum X-ray Study

The data from the X-ray diffraction study of sodium montmorillonite during adsorption and desorption of water vapor are presented in Tables 2 and 3, respectively. The line widths of the diffraction peaks, B_o, at half-height were determined as sketched in Figure 11 for a single peak. In order to determine the widths of composite peaks, the composite peak was resolved by trial-and-error into two normal peaks sketched to approach symmetry and for an equivalence of areas A and B, as shown in Figure 12. The widths of the individual peaks, B_o, at half-height were determined as shown. The total width at each half-height was then averaged to obtain a measure of the total width B_T of the composite peak. The integrated intensity represented by the area under the peak was measured at equilibrium by use of a planimeter. In order to insure the constancy of the X-ray system, the machine was allowed to warm up for about 30 minutes prior to X-raying the specimen. The relative vapor pressures, first order basal spacings, line widths of the resolved peaks and of the composite peaks, and integrated intensities of the resolved peaks and of the composite peaks are given in Table 2 for the adsorption run and in Table 3 for the desorption run.

The variation of the first order basal spacings of composite peaks with relative vapor pressures is shown in Figure 13a. The variations of the line widths of composite peaks is shown in Figure 13b. Figure 13a shows that the initial average basal spacing was not obtained on the desorption run, indicating some water was left entrapped in the interlayer

Table 2. X-ray diffraction data for high-vacuum study, adsorption run

p mm, Hg	p_o^a mm, Hg	p/p_o	Resolved[b] d_{001} spacings, Å	Percentage area of the peaks after resolution, percent	B_o^c degrees	B_T^d degrees	A_o^e in^2	A_T^f in^2
0.000	18.765	0.00	9.9	69.7	0.80	1.02	3.6	5.3
			10.8	30.3	1.16		1.7	
0.748		0.04	9.9	70.2	0.80	1.02	3.6	5.1
			10.8	29.8	1.23		1.5	
1.572		0.08	9.9	70.0	0.85	1.05	3.7	5.3
			11.0	30.0	1.26		1.6	
3.222		0.17	9.9	66.7	0.88	1.14	3.7	5.5
			11.1	33.3	1.41		1.8	
5.160		0.28	10.2	60.2	1.11	1.78	3.8	6.4
			11.6	39.8	1.46		2.6	
5.720		0.31	10.3	67.7	1.29	1.90	4.2	6.2
			12.0	32.3	1.35		2.0	
6.240		0.33	10.9	79.7	1.78	2.16	6.1	7.7
			13.1	20.3	1.10		1.6	

[a] p_o = vapor pressure of water at 21.1°C = 18.765 mm Hg.

[b] d_{001} = first order basal spacings between the clay platelets.

[c] B_o = line width of resolved peak.

[d] B_T = line width of composite peak.

[e] A_o = integrated intensity of resolved peak.

[f] A_T = total integrated intensity of composite peak.

Table 2. (Continued)

p mm, Hg	p_o[a] mm, Hg	p/p_o	Resolved[b] d_{001} spacings, Å	Percentage area of the peaks after resolution, percent	B_o[c] degrees	B_T[d] degrees	A_o[e] in^2	A_T[f] in^2
6.450	18.765	0.34	11.1 13.6	83.2 16.8	1.82 1.06	2.10	6.3 1.3	7.6
7.400		0.39	11.3 14.1	87.2 12.8	1.79 1.15	2.00	7.1 1.1	8.2
7.810		0.42	11.4 14.2	86.5 13.5	1.80 1.20	2.04	7.5 1.2	8.7
8.804		0.47	11.9 15.0	87.4 12.6	1.61 1.20	1.74	9.2 1.3	10.5
9.400		0.50	12.0 15.1	86.4 13.6	1.55 1.35	1.70	9.7 1.5	11.2
10.350		0.55	12.2 15.2	82.0 18.0	1.42 1.32	1.66	7.5 1.7	9.2
10.820		0.58	12.3 15.2	83.6 16.4	1.39 1.33	1.63	7.2 1.5	8.7
11.750		0.63	12.5 15.3	75.5 24.5	1.34 1.32	1.75	7.8 2.5	10.3
12.100		0.65	12.6 15.4	76.0 24.0	1.32 1.32	1.72	8.0 2.5	10.5
13.240		0.71	13.9	100.0	2.08	2.08	12.7	12.7
13.660		0.73	14.5	100.0	1.94	1.94	13.4	13.4
14.150		0.75	14.9	100.0	1.65	1.65	14.0	14.0

47

Table 2. (Continued)

p mm, Hg	p_o^a mm, Hg	p/p_o	Resolved[b] d_{001} spacings, Å	Percentage area of the peaks after resolution, percent	B_o^c degrees	B_T^d degrees	A_o^e in^2	A_T^f in^2
14.750	18.765	0.79	15.2	100.0	1.35	1.35	16.4	16.4
15.350		0.82	15.2	100.0	1.24	1.24	16.3	16.3
15.730		0.84	15.4	100.0	1.16	1.16	17.6	17.6
17.050		0.91	15.5	100.0	1.02	1.02	18.1	18.1
17.540		0.93	15.5	100.0	1.01	1.01	18.8	18.8
17.950		0.96	15.5	100.0	1.00	1.00	19.0	19.0
18.200		0.97	18.8	89.0	0.92	1.03	17.5	19.7
			22.4	11.0	0.98		2.2	
18.765		1.00	19.0	84.6	0.86	0.96	15.4	18.8
			23.6	15.4	0.88		3.4	

Table 3. X-ray diffraction data for high-vacuum study, desorption run

p mm, Hg	$P_o{}^a$ mm, Hg	p/P_o	Resolved^b d_{001} spacings, Å	Percentage area of the peaks after resolution, percent	$B_o{}^c$ degrees	$B_T{}^d$ degrees	$A_o{}^e$ in^2	$A_T{}^f$ in^2
18.765	18.765	1.00	19.0	84.6	0.86	0.96	15.4	18.8
			23.6	15.4	0.88		3.4	
17.400		0.93	18.9	82.5	0.67	0.76	20.3	24.3
			22.8	17.5	0.75		4.0	
15.680		0.84	18.8	84.0	0.74	0.88	21.4	25.0
			22.5	16.0	0.88		3.6	
14.100		0.75	15.6	95.7	0.73	0.79	22.4	23.4
			17.4	4.3	0.50		1.0	
13.250		0.71	15.4	100.0	0.91	0.91	17.2	17.2
12.350		0.66	15.1	100.0	1.20	1.20	15.3	15.3
11.150		0.59	12.8	11.9	0.68	1.78	1.6	
			14.4	88.1	1.44		11.8	13.4
9.940		0.53	12.8	64.6	0.88	1.43	7.6	11.5
			14.4	35.4	0.96		3.9	

$^a P_o$ = vapor pressure of water at 21.1°C = 18.765 mm Hg.

$^b d_{001}$ = first order basal spacing between the clay platelets

$^c B_o$ = line width of resolved peak.

$^d B_T$ = line width of composite peak.

$^e A_o$ = integrated intensity of resolved peak.

$^f A_T$ = integrated intensity of composite peak.

Table 3 (Continued)

p mm, Hg	P_o[a] mm, Hg	p/p_o	Resolved[b] d_{001} spacings,	Percentage area of the peaks after resolution, percent	B_o[c] degrees	B_T[d] degrees	A_o[e] in^2	A_T[f] in^2
8.770	18.765	0.47	12.7	80.0	0.74	0.91	8.0	10.0
			14.0	20.0	0.66		2.0	
6.170		0.33	12.6	91.7	0.75	0.83	9.3	9.7
			13.6	8.3	0.34		0.4	
4.330		0.23	12.5	100.0	0.87	0.87	10.0	10.0
2.530		0.14	12.1	100.0	1.43	1.43	7.8	7.8
0.020		0.00	10.0	72.0	0.90	1.14	1.8	2.5
				18.0	0.58		0.7	
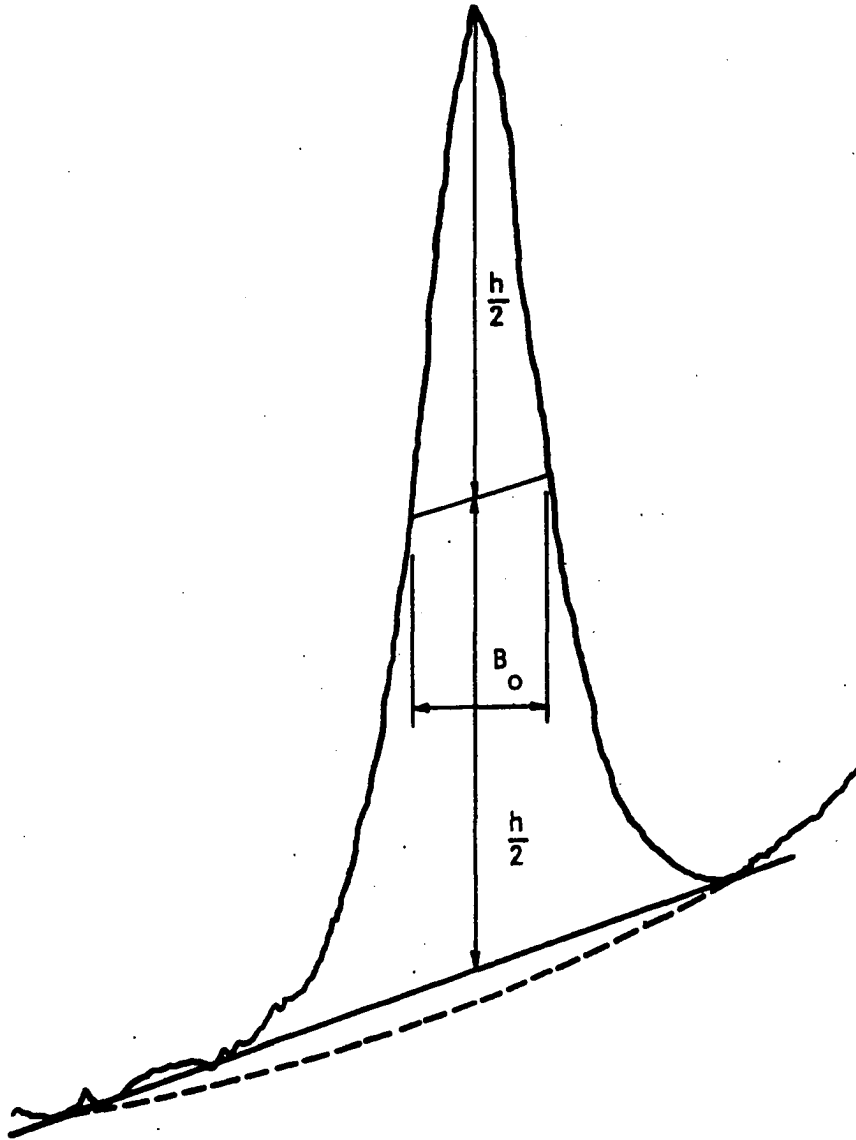
Figure 11. Sketch showing the determination of
X-ray diffraction peak

$$B_T = \frac{B_{T1} + B_{T2}}{2}$$

Figure 12.   Resolution of composite peak

Figure 13a. Variation of first order basal spacings
of composite peaks with relative pressure
of water vapor for sodium montmorillonite

Figure 13b. Variation of total line widths with
relative pressure of water vapor
for sodium montmorillonite
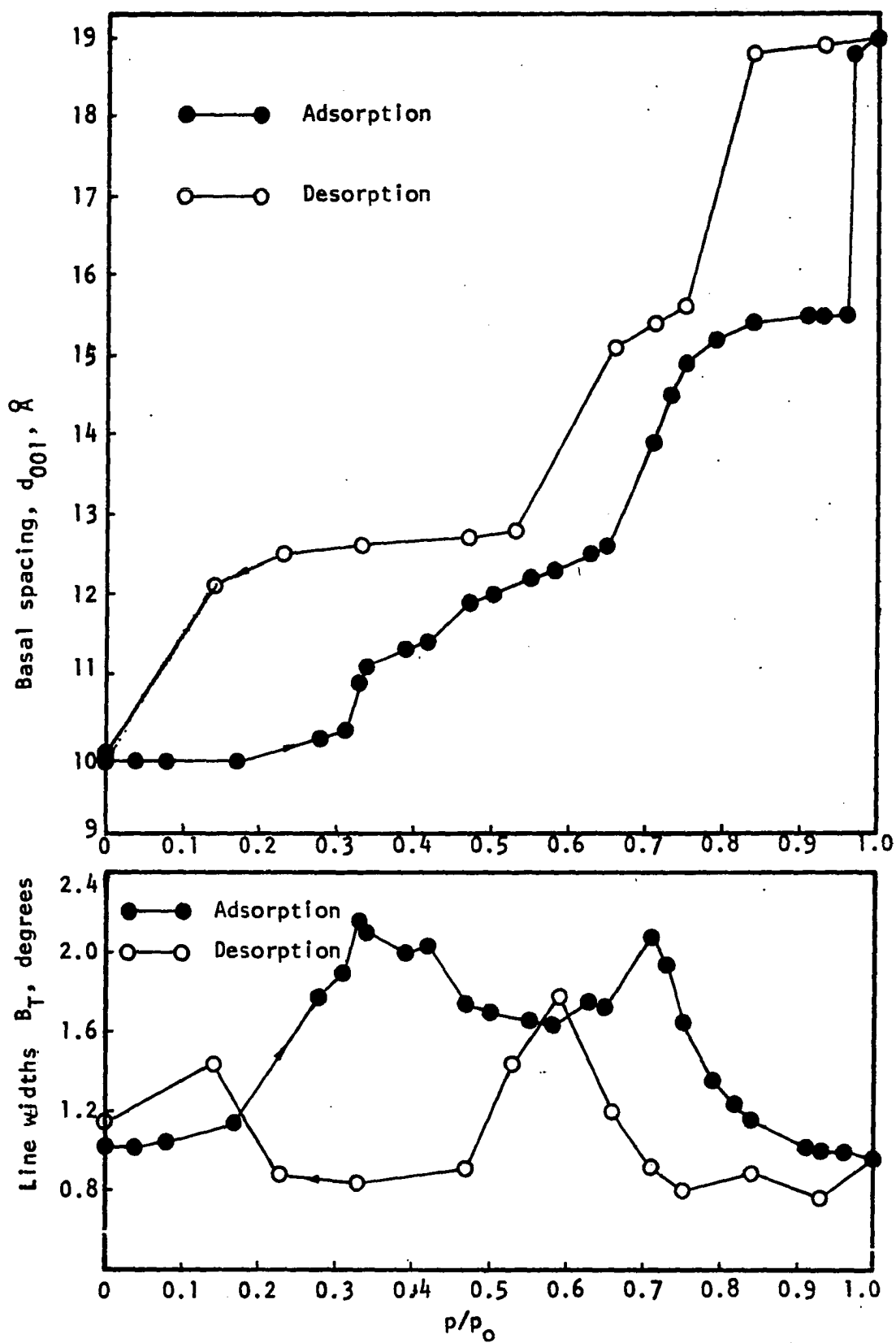
regions.

The data of the present study, Figure 13a, show that the change in the average basal spacing takes place in a continuous but nonuniform manner with change in relative pressure. The continuity is apparently due to the existence, simultaneously, of varying numbers of molecular layers of water, between clay platelets. The variation in total widths of the observed composite diffraction peaks are shown in Figure 13b. The variations are in part due to the lack of constancy of interlayer spacings (60, p. 517) and give an indication of the relative amounts of layers at the various spacings (67).

The curve of Figure 13b shows that line widths increase somewhat at low relative pressures, indicating some uptake of water in the interlayer regions although the average basal spacing remains constant at about 9.9 $\overset{o}{A}$. As the basal spacing increases there is a corresponding increase in line width to a maximum occurring near the center of the steeper portion of the basal spacing plot. The line widths then decrease as the basal spacing plot approaches a flatter portion. A minimum line width is reached at a relative pressure which corresponds to a basal spacing on the flat portion of the curve in Figure 13a. The minimum line width indicates that most of the clay platelets are nearly at the observed spacings. As the relative pressure increases another increment of expansion takes place and the line widths follow the same pattern as described above. Water take-up continues in this manner until the saturation pressure is reached.

The general shape of the adsorption and desorption plots in

Figure 13a is very similar to those presented elsewhere (33,43,76,80,97, 120). The adsorption curve displays a rather steep portion between relative pressures of 0.28 to 0.50 followed by a somewhat less steep portion. Another steeper portion begins at a relative pressure around 0.65. This corresponds to the region in which the second increment of platelet separation (or uptake of a second layer of interlayer water) begins to take place. Figure 13a also shows that the steeper portion between p/p_0 of 0.28 to 0.50 corresponds to the first increment of layer separation. The initial portion of the adsorption curve in Figure 13a, $p/p_0 = 0$ to $p/p_0 = 0.20$, indicates that the initial water adsorbed is mainly confined to the external surface of the clay platelets, so the basal spacing of the clay platelets does not change much in this region. This is consistent with studies of other investigators (7,80,97); for example, Barrer and MacLeod (7) explained that the initial water adsorbed is mainly confined to the external surface of the clay platelets. After an approximate threshold pressure is reached the water molecules penetrate more freely between the clay platelets and cause separation. With water vapor, a second stage of interlayer adsorption occurs and is reflected by the second steeper portion of the adsorption curve in Figure 13a. As p/p_0 approaches 1.00, capillary condensation is added to the interlayer adsorption. The X-ray data of Figure 13a show that a third increment of platelet separation also occurs at high relative pressures. The desorption curve exhibits three steep portions along the course of desorption. Each steep portion represents the removal of a layer of the interlayer water from the clay platelets.

Figure 13a also shows a hysteresis loop existing in adsorption and desorption run. This is consistent with the results obtained in the past investigations (33,43,76,80,97,120). Hysteresis was explained by many investigators. In the study of water vapor adsorption by montmorillonite, Mooney et al. (79,80), on the basis of irreversible hysteresis, assumed that the desorption branch represented the true equilibrium curve. Mooney et al. (79) found that, by repeated running the adsorption-desorption run on the same sample for many times, the desorption branch was more closely reproduced than was the adsorption branch. They explained the nonreproducibility of the adsorption curve when adsorption is begun on a practically dry clay, surface heterogeneities cause the system to be very sensitive to slight variations in the amount of residual water present. When desorbing from an almost saturated clay, slight variations in water content are no longer significant. Johansen and Dunning (55) suggested the lack of reproducibility of adsorption is due to an inability to desorb back to the beginning of the hysteresis loop, which is very near zero relative pressure. McBain (70) and Foster (39) explained the hysteresis on the basis of the shape and arrangement of the pores in which capillary condensation takes place. Since effective degassing can minimize the Zigsmondy type of hysteresis, the pore structure would probably be the main cause of hysteresis.

Barrer and MacLeod (7) studied the adsorption of various non-polar and polar gases and vapors, including water vapor, by a sodium-rich montmorillonite. They explained the hysteresis observed when polar gases and vapors are adsorbed in the interlayer regions. If nucleation of an

adsorbate-rich phase occurs around the periphery of crystallites poor
in adsorbate, this nucleation of an adsorbate-rich phase must be
associated with strain and interfacial free energies. These free
energies are positive, and so slow down the free development of the ad-
sorbate-rich phase until the pressure has exceeded the value for true
thermodynamic equilibrium between the vapor and separated montmorillonite
pletelets with and without interlayer adsorbate. On desorption the
development of the adsorbate-poor phase in the interlayer region is de-
layed by strain and interfacial free energy until the pressure has fallen
below that for true equilibrium. This results in a hysteresis loop.
They found the hysteresis observed on sorption of water vapor to be a
composite loop associated with both capillary condensation and interlayer
water. They also observed a hysteresis loop for adsorption-desorption
of nonpolar gases and vapors on their montmorillonite. Since the non-
polar adsorbates were adsorbed only on the external surface, the reasons
extended for hysteresis with polar adsorbates are not applicable. They
suggested that when clay particles are lubricated by a film of capillary
condensate some of the clay particles are drawn by surface tension forces
into a thixotropic structure. This more regular array then retains
capillary condensed adsorbate more firmly than would a purely random
array. When the film of capillary condensate becomes sufficiently dilute
it ceases to lubricate and hold the thixotropic structure together. The
array then becomes more random again and must give up the remaining con-
densate.

Hirst (51) also developed an explanation for hysteresis associated

with interlayer adsorption. Attraction forces between platelets prevent penetration of the adsorbate until a threshold pressure is reached. These forces are then overcome by forces leading to penetration and the platelets separate to admit a layer of adsorbate. The interlayer attraction is reduced by the expansion, so further separation requires less energy. However, the energy of adsorption is also less and a second layer of adsorbate does not enter until a higher pressure is reached. On desorption the platelets are initially separated and their attractive interaction weakened while the forces tending to separate them are high. The platelets cannot come together until the amount of interlayer adsorbate, and thus swelling pressure, are substantially reduced. Therefore, a hysteresis loop is observed.

According to Brunauer (22, p. 409) the adsorption process most probably causes a change in the pore volume which may be either reversible or irreversible. The pore volume change may result in different pore shapes and arrangements in the external surfaces of the montmorillonite sample. X-ray diffraction data, the initial adsorption curve of Figure 13a, show that at p/p_o of about 0.20 the uptake of water into the interlayer region begins.

Because the present data of the adsorption-desorption study of montmorillonite tend to be consistent with the data by other investigators, it is informative to consider some evidences from past studies in the discussion of the data of the present study. Hendricks and Jefferson (49) have shown that theoretically the X-ray diffraction from a powder should show that the basal spacing would vary continuously with water content,

and Hendricks et al. (50) found this to be so in their study. Mooney
et al. (80), from the X-ray data on desorption from Wyoming montmoril-
lonite and data of Hendricks et al. (50) on Mississippi and California
montmorillonites produces an almost perfect stepwise curve. Roderick
(97) studied the adsorption and desorption of water vapor for sodium
montmorillonite and his data are shown in Figure 14. The change between
the basal spacing plot and line width plot depends on many factors.
Roderick (97), after investigating the adsorption and desorption of water
vapor for sodium montmorillonite for many cycles, concluded that the
major factors responsible for the scatter of the X-ray data on adsorption
and desorption are: (a) the initial condition of the sample at the start
of the test, (b) the source and method of preparation of the material,
and (c) whether the data are collected during adsorption or desorption.
Other factors are the control of temperature and humidity and possibly
the size of the clay particles.

Arrangements of interlayer water

As adsorption on the internal surfaces of montmorillonites proceeds
the molecular layers of interlayer water buildup either in a laminar or
in other spatial geometric arrangements. In the first case the stable
thickness should be integral multiples of the diameter of a water molecule;
in the second they should conform to a geometry dictated by the size of
the water molecule. Hypothetical configurations for the water adsorbed
on the clay surface have been postulated by several investigators
(8,37,38,45,49,68), as discussed in the Review of Literature.

The continuity of the basal spacing versus relative pressure curve

Figure 14.   Variations of first order basal spacings
and line widths with relative pressure
of water vapor for sodium montmorillonite
(after Roderick, 97)
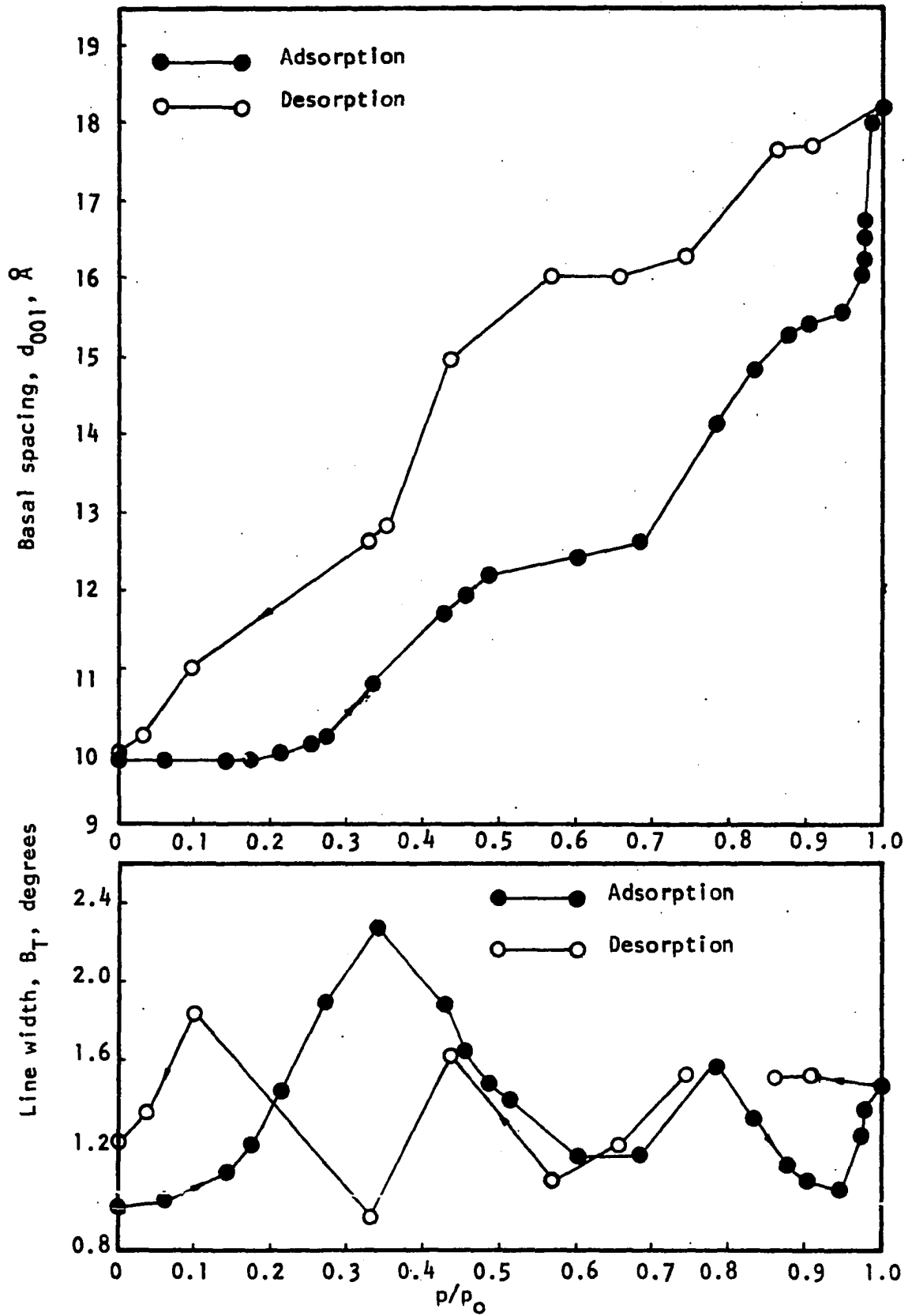
has been attributed to the simultaneous existence of clay platelets separated by various molecular layers of interlayer water. If all the interlayer water has been removed to zero relative pressure, a sharp peak will be observed corresponding to the collapsed basal spacing of sodium montmorillonite, about 9.6 Å (21). As the relative pressure increases some water begins to penetrate between some of the clay platelets.

Figure 15 shows the relationship between the total line widths of composite peaks and the first order basal spacings for the adsorption run of the present study. The basal spacings at three minimum line widths occur at 12.3 Å, 15.5 Å and 19.0 Å, more or less corresponding to the first, second and third layers of interlayer water. The minimum line width at the basal spacing of 19.0 Å occurred following a jump in the data near the saturation region, such that intermediate spacings were not obtained.

Using 9.60 Å as the collapsed basal spacing of sodium montmorillonite, basal spacings at various hypothesized configurations of interlayer water can be developed as shown in Table 4 (97). The three spacings of Figure 15, at 12.3, 15.5, and 19.0 Å, do not correspond to any of the postulated structures. Before this phenomenon is discussed, some assumptions used in this study will be introduced. Following Roderick (97), it is assumed that (a) the system of the present study may be treated as a random interstratification of two components of clay platelets with two different average basal spacings, (b) peak averaging between pure component positions is linear and in proportion to the components, such that (c) maximum line widths occur when the relative proportion of the two
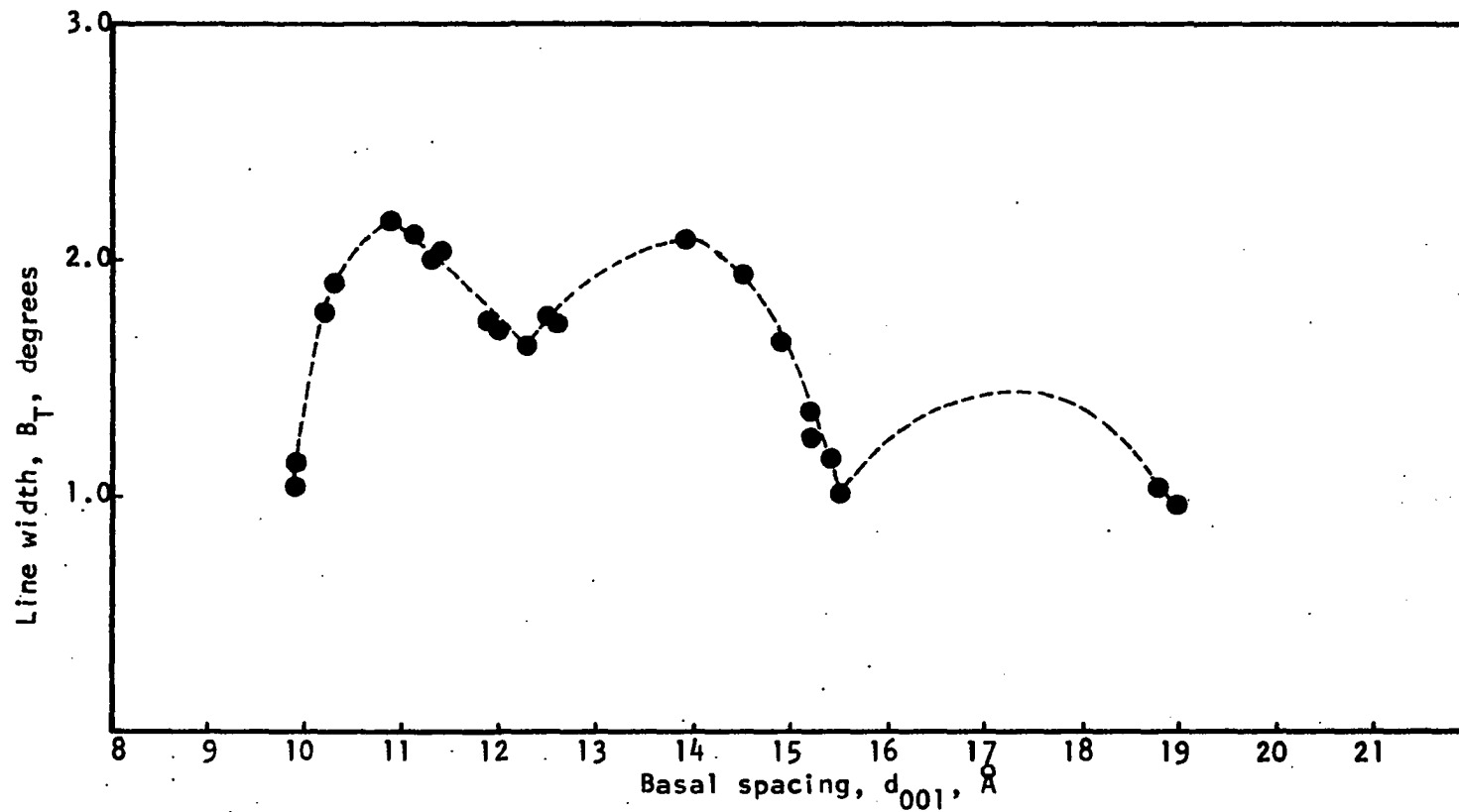
Figure 15. Variation of line widths with basal spacings of sodium montmorillonite, adsorption run

Table 4. Calculated first order basal spacings of sodium montmorillonite for various suggested interlayer water configurations (after Roderick, 97)

Number of molecular layers of water	Calculated basal spacing for laminated stacking,[a,b] Å	Ice configuration[c] Calculated basal spacing, Å		Barshad's configuration Calculated basal spacing, Å	
		Alternative 1	Alternative 2	Alternative 1	Alternative 2
0	9.60	9.60	9.60	9.60	9.60
1	12.36[d]	12.36[d]	12.36[d]	11.38	11.38
2	16.12	13.28	15.12	13.47	14.14
3	17.88	16.04	15.12	15.56[d]	16.90
4	20.64	16.96	16.96		
5	23.40	19.72[d]	19.72[d]		
6	26.16	20.64	22.48		

[a]Configuration of Hendricks and Jefferson (49).

[b]Third alternative of Barshad (9).

[c]Alternatives suggested by Demirel (33).

[d]Agrees most closely with observed spacings.

components are equal, (d) minimum line widths correspond to dominance of single component, and therefore should correspond to a basal spacing near that calculated from the proposed arrangement. If assumptions (b) and (c) hold, the maximum line widths should occur at a basal spacing which is the average of those calculated for two successive molecular arrangements of water between platelets, as for example midway between the positions for 0 and 1 layer of interlayer water, or 1 and 2 layers. The following discussion for the basal spacings at maximum and minimum line widths is based on the above assumptions.

The first maximum line width occurs at a basal spacing of about 10.90 Å, very close to the 10.98 Å average calculated for zero and one molecular layers of water. The first minimum line width occurs at about 12.30 Å which is close to the calculated value of 12.36 Å for one molecular layer of water. However, this line width is still relatively large, indicative of nonuniform spacing. The second maximum line width, after interpolation, appears to be at about 13.75 Å which is very near to 13.74 Å average for one and two layers of interlayer water. However, the second minimum line width is at about 15.50 Å or more because of the data gap, is somewhat higher than 15.12 Å calculated for two laminar layers of water, and corresponds most closely to Barshad's Alternative 1 for three layers of water. None of the alternatives account for any influence from the interlayer cation, and it would appear that there may be a change in the water structure as the distance from the mineral surface increases, plus a change in the position of the hydrated cation.

An additional light on this problem may be obtained by resolving

X-ray traces into two peaks as shown in Figure 12. The first order basal

spacings of the resolved peaks are plotted in Figure 16 for the adsorption

run only. The most intense resolved peak is named the primary peak and

the other resolved peak composing the same composite peak is called a

secondary peak. The more conventional method of plotting only one basal

spacing at the maximum unresolved intensity (C in Figure 12) gives only

the primary peak line in Figure 16.

According to Figure 16 the secondary peak tends to converge with the

primary peak as the relative vapor pressure increases to p/p_o = 0.85,

indicating that at this relative pressure essentially all clay platelets

have the same basal spacing. According to the data in Table 2 the

secondary peak also is sharpening as the relative pressure increases.

In Figure 16 it is evident that platelet adjustment starts as soon as

water vapor is introduced into the system, although the basal spacings of

the primary peaks are nearly constant up to p/p_o = 0.18. The changes

in the secondary peaks indicate that there is at least a partial change

in the basal spacings in some clay platelets, but the change is not uni-

form throughout the whole mass of the clay. The data in Figure 16 agree

with the previous conclusion, that the 9.9 and 12.3 Å peaks are composite

whereas 15.5 Å peak is not. The reason for the broadness at 12.3 Å peak

is therefore due to the interstratification with 15 Å, indicating 12.3 Å

may be too high. The change in the primary peak being gradual indicates

either interstratification or a variable water position, the first water

perhaps fitting in the tetrahedral faces as proposed by Barshad (8) and

discussed in the Review of Literature.

Figure 16.   Variation of first order basal spacings with
             relative pressure of water vapor after resolving
             into primary and secondary peaks for sodium
             montmorillonite, adsorption run
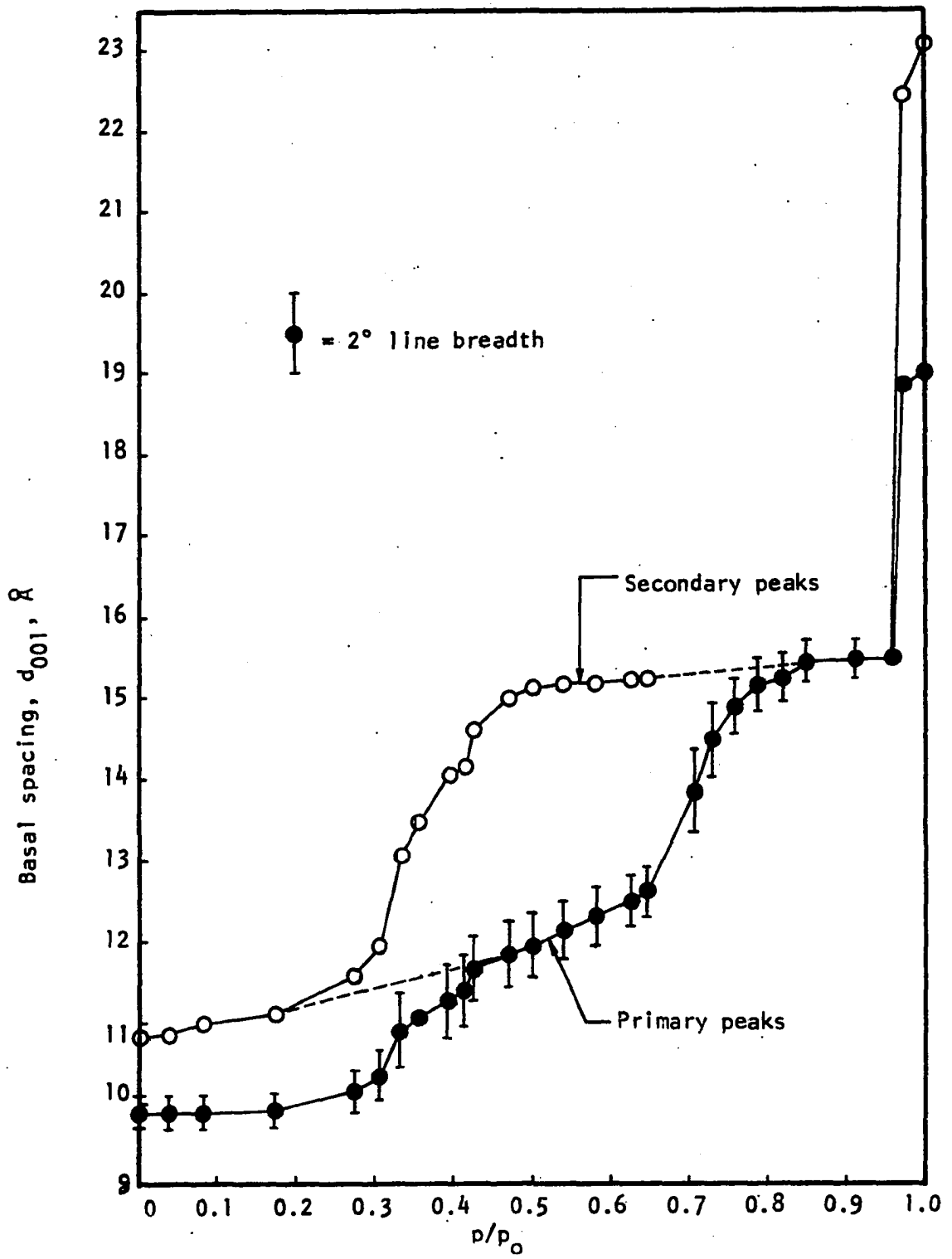
From the data of Table 2, at p/p_o = 0.71 there is one peak with a basal spacing of about 13.7 Å. However, from Figure 16, there are secondary peaks from p/p_o = 0.65 to p/p_o = 0.85. The presence of the secondary peak is indicated by the convergence of the curve for secondary peaks and that for the primary into a single peak. After convergence into a single peak at p/p_o = 0.85, the single peak continues until a relative pressure of 0.96 is reached. At p/p_o = 0.96 the basal spacing of the primary peak is 15.5 Å, that is in the second state of hydration. When the relative pressure is beyond 0.96, or when the third state of hydration begins, the integrated intensity of the peak is reduced and there is the appearance of a new secondary peak of higher basal spacing. When the relative pressure is greater than 0.96 there is an abrupt loss of the lower basal spacing and it was found that the integrated intensity was reduced as the sodium montmorillonite adsorbed more water beyond p/p_o of 0.96. The reduction in intensity suggests an increased degree of randomness in the interlayer water structure of the sodium montmorillonite.

The steepness in slope of the primary curve in Figure 16 indicates that the particles are adsorbing a discrete amount of interlayer water, after which the slope of the primary curve is flattened. The apparent smooth change from the basal spacing of 10.8 Å to 12.6 Å (dashed line in Figure 16) and 15.2 Å to 15.5 Å (dashed line in Figure 16) indicates a gradual changing of average interlayer spacing with a narrowing of the distribution, as indicated by line widths, at 12.3 and 15.5 Å.

Figure 17 shows the percentage area of primary peaks and secondary peaks with respect to the relative pressure. The area under the peak is
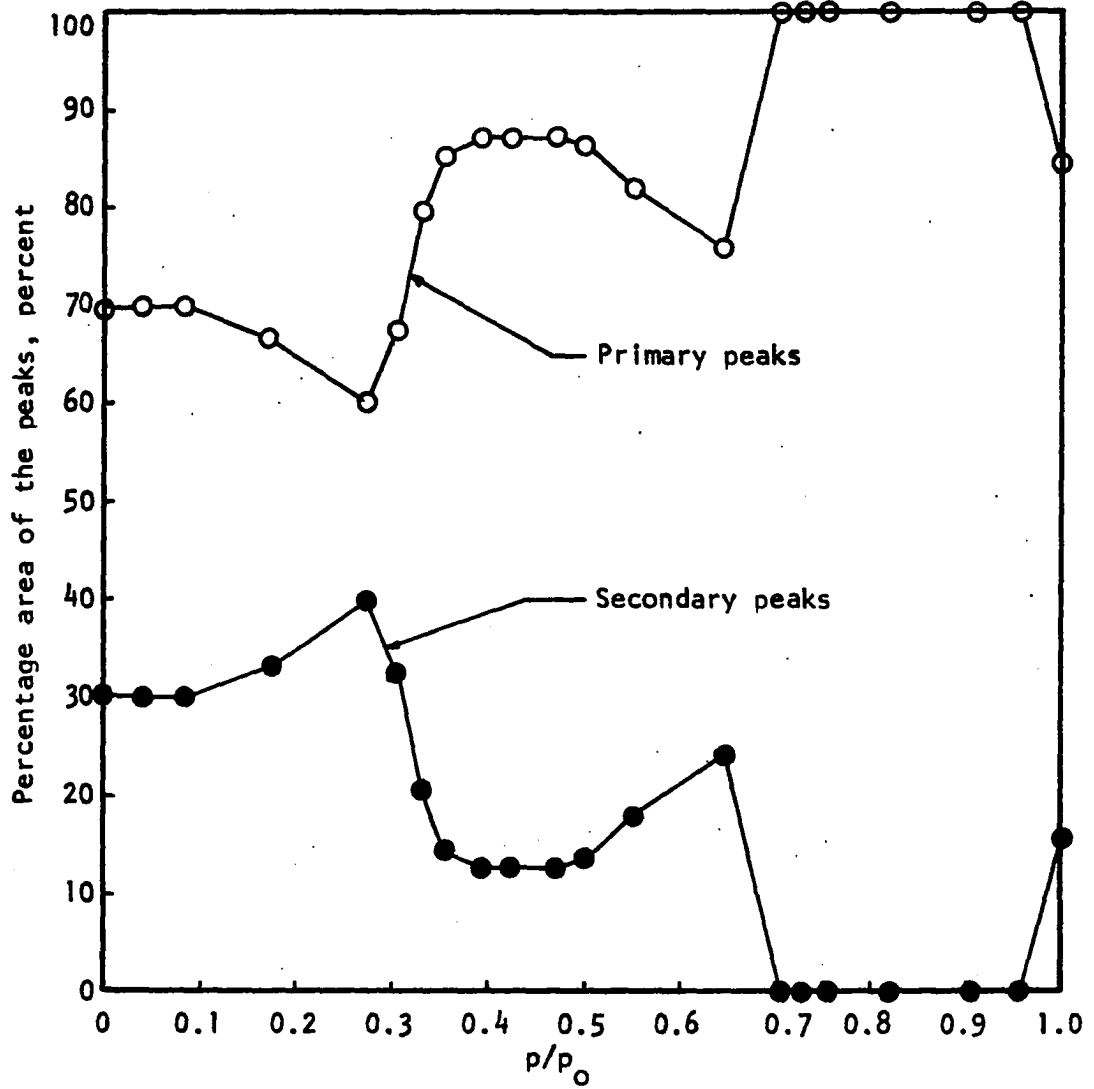
Figure 17. Percentage area of the composite peaks after resolving
into primary and secondary peaks with relative pressure
of water vapor for sodium montmorillonite, adsorption
run

a measure of intensity and thus indicates the relative amounts of clay

platelets that have the spacing corresponding to the peak position. From

Figure 17, at zero relative pressure the quantity of the clay platelets

initially at 9.9 $\overset{o}{A}$ spacing is about 70 percent of the total diffracted

platelets. This is only approximate since no correction has been made

for the structure factor, which is not known, or for the Lorentz-polariza-

tion factor. When the vapor pressure increases the platelets adjust

themselves in a complex manner and there are changes, mostly increases,

in the basal spacing within those platelets. The composite peaks with

two average basal spacings are obtained because of the water layers be-

tween the clay platelets are different. From Figures 16 and 17, at

particular relative pressures, p/p_0, there are two average basal spacings

resulting in a composite peak.

Figures 18a and 18b show the relationship between total integrated

intensity of composite peaks with relative vapor pressure. Figure 18a

shows that the total integrated intensity, in the unit of area under

the peak, increased with relative pressure. The total integrated inten-

sity of composite peaks expressed in the number of counts is shown in

Figure 18b. The integrated intensities in both figures, Figures 18a and

18b, are not corrected for the Lorentz-polarization factor. The one

corrected for the Lorentz-polarization factor is shown in the plot of

Figure 18c. The data for this correction are shown in Table 5a for the

adsorption run and Table 5b for the desorption run. The method of

calculation for the Lorentz-polarization factor is shown in Appendix ii.

A drop in intensity from p/p_0 = 0.50 to p/p_0 = 0.55 is due to the
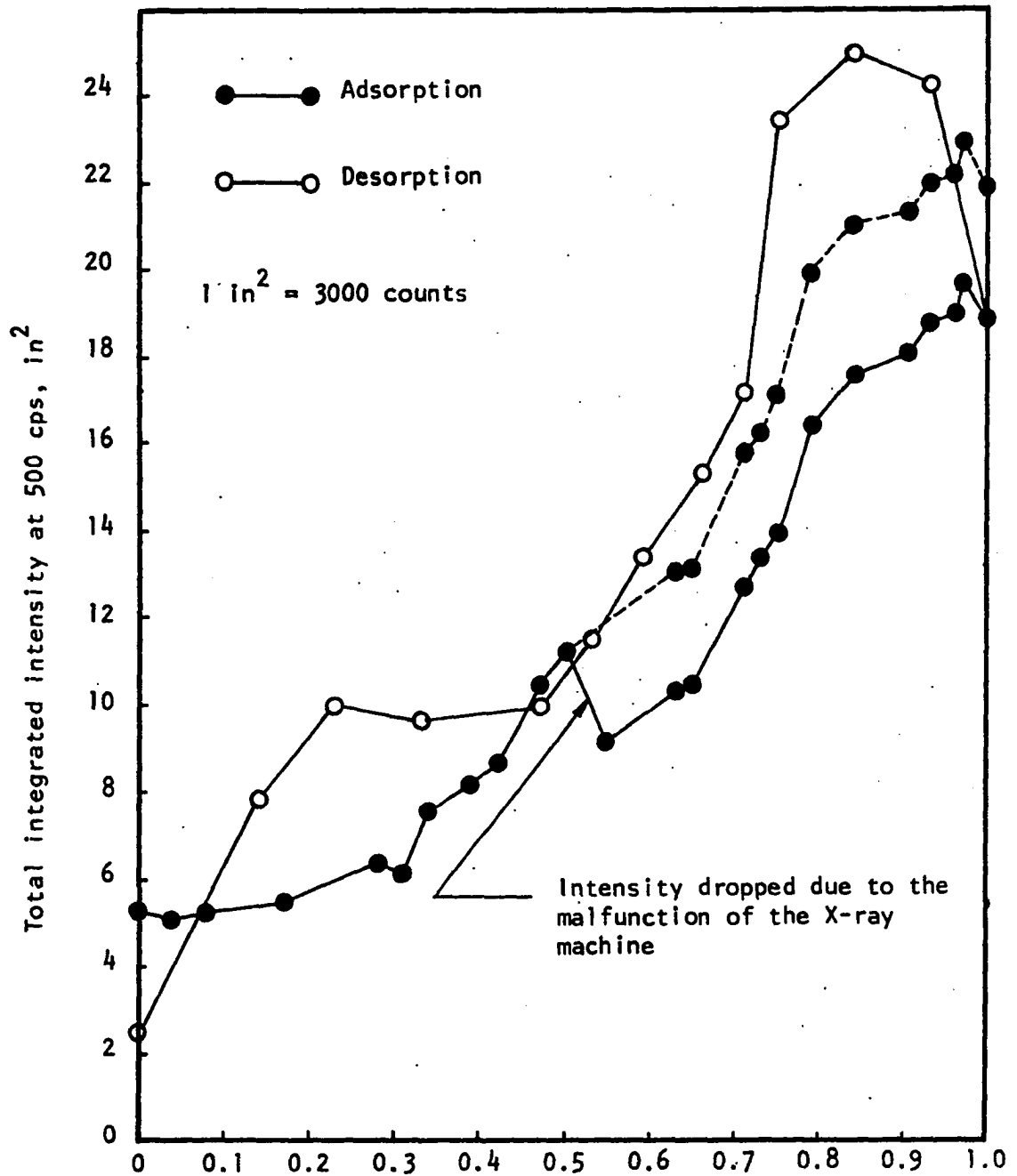
Figure 18a. Variation of peak area with relative pressure of water
vapor for sodium montmorillonite, before applying the
Lorentz-polarization factor
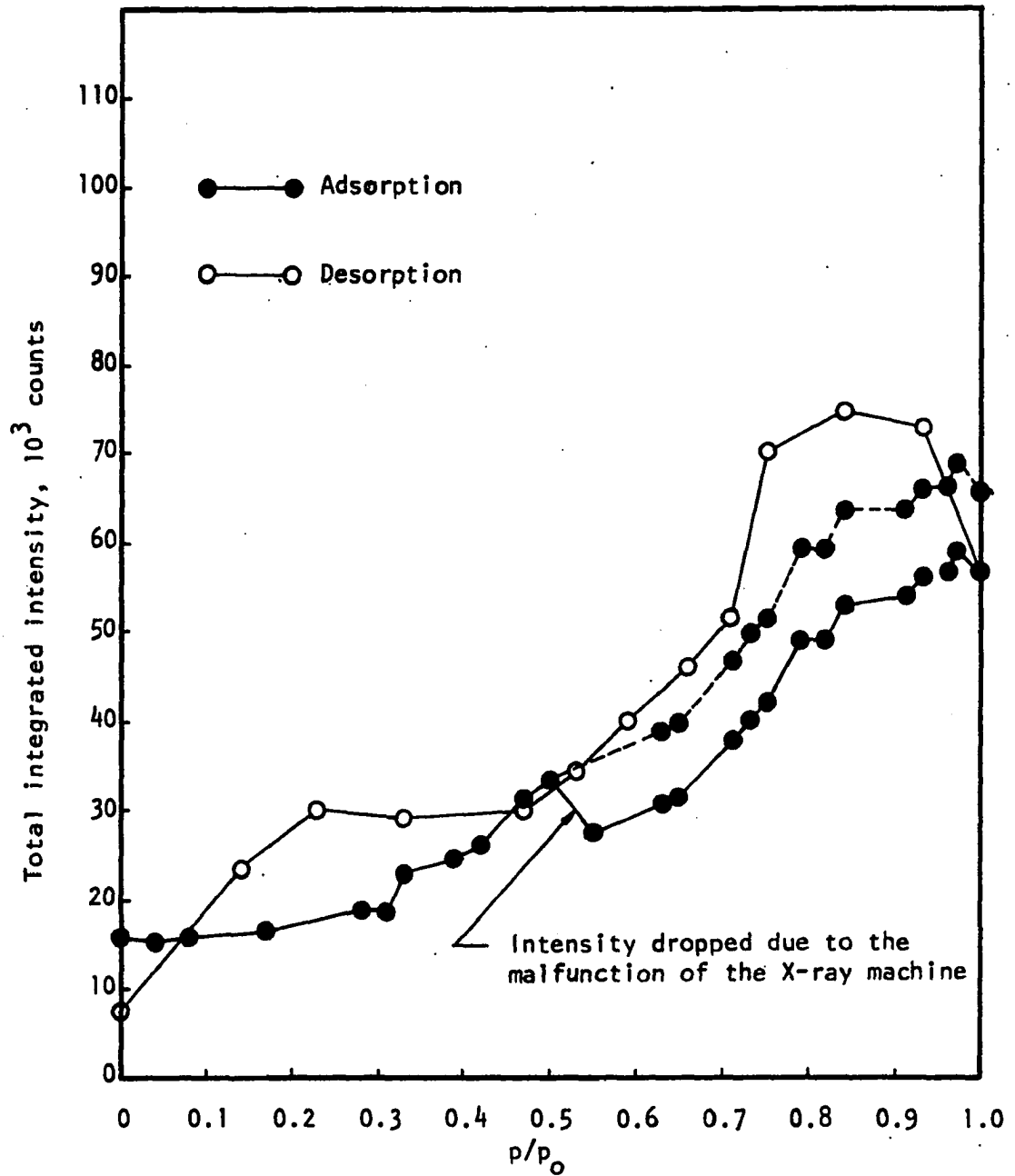
Figure 18b. Variation of integrated intensity with relative pressure of water vapor for sodium montmorillonite, before applying the Lorentz-polarization factor
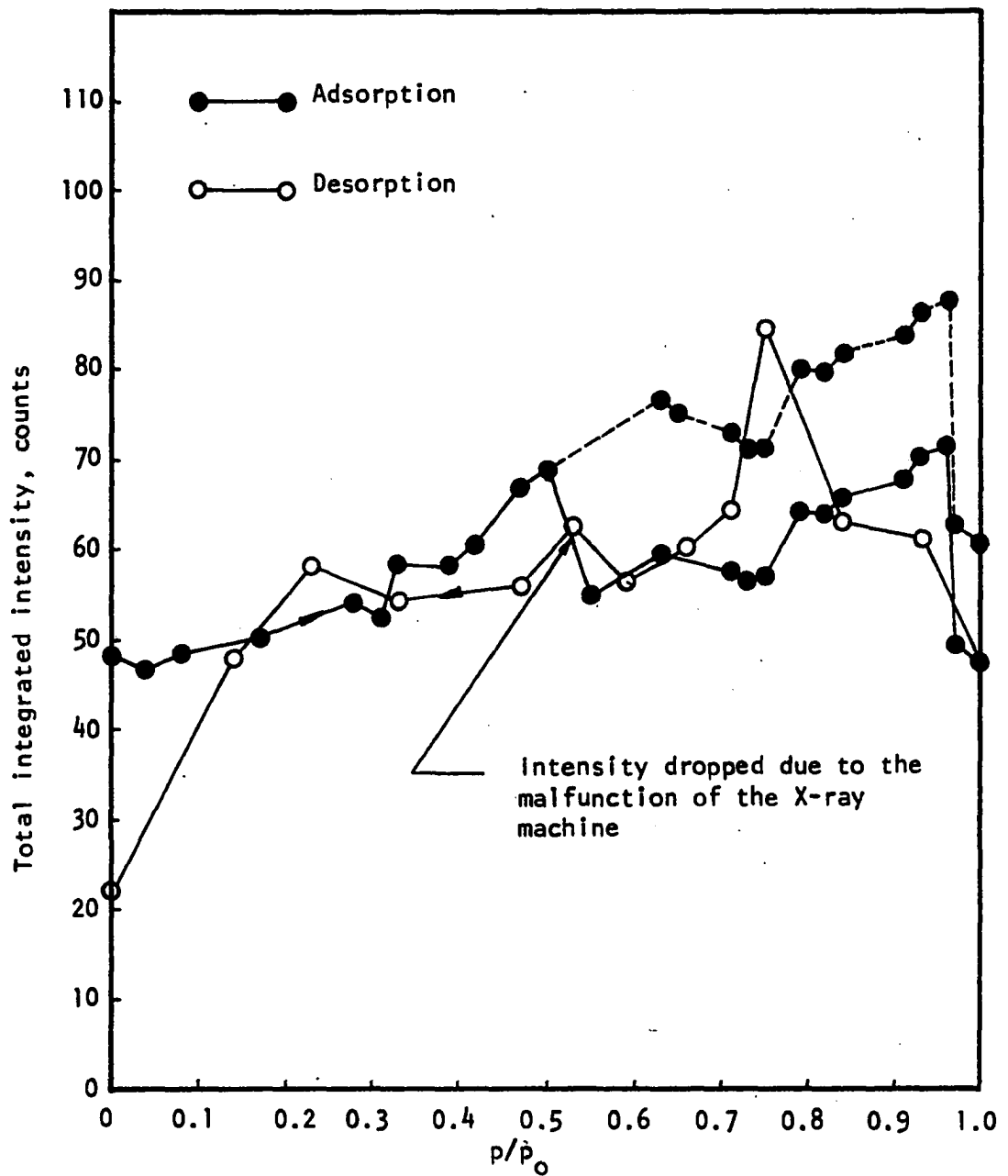
Figure 18c. Variation of integrated intensity with relative pressure of water vapor for sodium montmorillonite, after applying the Lorentz-polarization factor

Table 5a. Total integrated intensity corrected for the Lorentz-polarization factor[a], adsorption run

p/p_o	d_{001} Å	$\sin \theta$ [b]	LP[c]	I_{total} in²	I_{total} 10^3 counts	$I_{total}/(LP)$ in²	$I_{total}/(LP)$ counts	$\dfrac{I_{total}}{(LP)d_{001}}$
0.00	9.9	0.078	325.7	5.3	15.9	0.0162	48.6	4.9
0.04	9.9	0.078	325.7	5.1	15.3	0.0156	46.8	4.7
0.08	9.9	0.078	325.7	5.3	15.9	0.0162	48.6	4.9
0.17	9.9	0.078	325.7	5.5	16.5	0.0168	50.4	5.0
0.28	10.2	0.075	352.6	6.4	19.2	0.0181	54.3	5.3
0.31	10.3	0.075	352.6	6.2	18.6	0.0175	52.5	5.0
0.33	10.9	0.071	393.8	7.7	23.1	0.0195	58.5	5.3
0.34	11.1	0.069	417.1	7.6	22.8	0.0182	54.6	4.9
0.39	11.3	0.068	429.5	8.2	24.6	0.0190	57.0	5.0
0.42	11.4	0.068	429.5	8.7	26.1	0.0202	60.6	5.3
0.47	11.9	0.065	470.4	10.5	31.5	0.0223	66.9	5.6
0.50	12.0	0.064	486.3	11.2	33.6	0.0230	69.0	5.7

[a]See Appendix II.

[b]$\sin \theta = \lambda/2d = \dfrac{1.54}{2d} = 0.77/d.$

[c]LP = the Lorentz-polarization factor.

76

Table 5a (Continued)

p/p_0	d_{001} Å	$\sin \theta^b$	LP^c	I_{total} in^2	I_{total} 10^3 counts	$I_{total}/(LP)$ in^2	$I_{total}/(LP)$ counts	$\dfrac{I_{total}}{(LP)d_{001}}$
0.55	12.2	0.063	500.9	9.2	27.6	0.0183	54.9	4.5
0.58	12.3	0.063	500.9	8.7	26.1	0.0173	51.9	4.2
0.63	12.5	0.062	517.3	10.3	30.9	0.0199	59.7	4.7
0.65	12.6	0.061	534.5	10.5	31.5	0.0196	58.8	4.6
0.71	13.9	0.055	658.2	12.7	38.1	0.0192	57.6	4.1
0.73	14.5	0.053	709.0	13.4	40.2	010188	56.4	3.8
0.75	14.9	0.052	736.7	14.0	42.0	0.0190	57.0	3.8
0.79	15.2	0.051	765.9	16.4	49.2	0.0214	64.2	4.2
0.82	15.2	0.051	765.9	16.3	48.9	0.0213	63.9	4.2
0.84	15.4	0.050	797.0	17.6	52.8	0.0220	66.0	4.2
0.91	15.5	0.050	797.0	18.1	54.3	0.0227	68.1	4.3
0.93	15.5	0.050	797.0	18.8	56.4	0.0235	70.5	4.5
0.96	15.5	0.050	797.0	19.0	57.0	0.0238	71.4	4.6
0.97	18.8	0.041	1187.0	19.7	59.1	0.0165	49.5	2.6
1.00	19.0	0.041	1187.0	18.8	56.4	0.0158	47.4	2.4

Table 5b. Total integrated intensity corrected for the Lorentz-polarization factor[a], desorption run

p/p_o	d_{001} Å	$\sin \theta$ [b]	LP[c]	I_{total} in^2	I_{total} 10^3 counts	$(I_{total})/LP$ in^2	$(I_{total})/LP$ counts	$\dfrac{I_{total}}{(LP)d_{001}}$
1.00	19.0	0.041	1187.0	18.8	56.4	0.0158	47.4	2.4
0.93	18.9	0.041	1187.0	24.3	72.9	0.0204	61.2	3.2
0.84	18.8	0.041	1187.0	25.0	75.0	0.0210	63.0	3.3
0.75	15.6	0.049	830.0	23.4	70.2	0.0282	84.6	5.4
0.71	15.4	0.050	797.0	17.2	51.6	0.0215	64.5	4.1
0.66	15.1	0.051	765.9	15.3	45.9	0.0199	59.7	3.9
0.59	14.4	0.053	709.0	13.4	40.2	0.0188	56.4	3.9
0.53	12.8	0.060	552.6	11.5	34.5	0.0208	62.4	4.8
0.47	12.7	0.061	534.5	10.0	30.0	0.0187	56.1	4.4
0.33	12.6	0.061	534.5	9.7	29.1	0.0181	54.3	4.3
0.23	12.5	0.062	517.3	10.0	30.0	0.0193	57.9	4.6
0.14	12.1	0.064	485.3	7.8	23.4	0.0160	48.0	3.9
0.00	10.0	0.077	334.3	2.5	7.5	0.0074	22.2	2.2

[a]See Appendix II.

[b]$\sin \theta = \lambda/2d = 1.54/2d = 0.77/d$.

[c]LP = the Lorentz-polarization factor.

malfunction of the X-ray machine. However, beyond $p/p_o = 0.55$ the in-tensities follow the trend of increasing with relative pressure until the relative pressure of 0.97 is attained, then the intensity dropped in the vicinity of relative pressure close to 1.00. The dashed lines in these figures are extrapolated to show the probable trend of intensity in the case of proper function of the X-ray machine. The curves showing the relationship between intensity and relative pressure is not smooth; this will be discussed later.

The intensity of a diffraction peak is given by $I = \theta |F_1|^2 \phi$, where θ is the combined Lorentz-polarization factor which increases with de-creasing diffraction angle, F_1 is the layer structure factor, and ϕ is the mixing function dependent on the spacings of the constituent phases and the probability of occurrence of these spacings (67). Johns, Grim and Bradley (56) have shown, on the basis of Bradley's data (16), that the intensity of diffraction from three-layer clay minerals at an angle corresponding to 17 Å should exceed that reflected at 10 Å by a factor of approximately four. The intensity data they obtained are without correction for the Lorentz-polarization factor. The result is consistent with the data of the present study as shown in Figures 18a and 18b. The Lorentz-polarization factor θ alone will cause a 17 Å peak to be nearly three times as intense as a 10 Å reflection (60, p. 683). After correction for the Lorentz-polarization factor as shown in Tables 5a and 5b for adsorption and desorption cycles, the intensity ratio at 17 Å to that at 10 Å drops to about two. This increase in intensity is indicative of a change in layer structure factor. Local maxima and minima of observed

intensities are probably due to the mixing function ϕ, i.e. the relative proportions of layers at different spacings and the randomness of their distribution, and perhaps minor changes in preferred orientation. The drop in intensity when $p/p_o = 0$ on desorption run and $p/p_o = 1.0$ on both runs is due to the variable hydration of the clay particles in the system. This result is consistent to Figures 16 and 17 and line widths in Figure 13b.

Free Energy Changes

Free energy changes on adsorption

As pointed out in Equation (3), the free energy change of adsorption may be expressed as:

$$\Delta F = -\frac{RT}{M\Sigma} \int_{0}^{p/p_o} \frac{q}{p/p_o} \, d(p/p_o) \ .$$

Fu and Bartell (42), in their study of the surface areas of porous adsorbents, evaluated this equation at various values of p/p_o for the adsorption of vapors on porous solids. When q is the mass of vapor adsorbed per gram of solid, the value obtained in the free energy change, $\Sigma\Delta F$ in ergs/gm of solid, for adsorption from a relative pressure of zero to p/p_o. When the values of $\Sigma\Delta F$ were plotted against p/p_o a curve consisting of two portions was obtained; each portion could be represented by an equation of the form

$$\Sigma\Delta F = \alpha(p/p_o)^\beta \tag{7}$$

where ΔF is the change in free energy per unit area, α and β are constants

which are different for the two portions of the curve, p/p_o in the relative vapor pressure, and Σ is the area on which adsorption takes place. They pointed out that this method can be utilized to study the expansion and deformation of porous materials caused by adsorption of various vapors (42). For a given adsorbate-adsorbent system, α and β remain constant so long as there is no change in the mechanism of adsorption, such as capillary condensation or swelling. Where a change occurs, values of α and β change to another set of constant values. If only the external surface areas of the clay are involved in adsorption of the vapor, the relationship can be made to read:

$$\Sigma_{ext.} \ \Delta F = \alpha(p/p_o)^\beta \ . \tag{8}$$

The change in slope of the $\Sigma \Delta F$ curve observed by Fu and Bartell (42) was attributed to capillary condensation in the pores of the adsorbents. The exact point at which capillary condensation takes place cannot be determined, but it may be assumed to show its most pronounced effects at p/p_o values from greater than 0.90 to saturation. For clay minerals, while capillary condensation undoubtedly has some effects, swelling (interlayer expansion) manifests itself more profoundly throughout the entire adsorption range.

Fu and Bartell (42) found that if log ($\Sigma \Delta F$) was plotted against log (p/p_o), two straight-line portions were obtained. From the intersection of the two portions of the curve and from the hypothetical process they proposed, they were able to derive an expression for the specific surface of rigid porous adsorbents which did not involve assigning a molecular

area to the adsorbate. They tested their method with a variety of
adsorbents and adsorbates, and the specific surfaces obtained were found
to be in a very good agreement with those determined by the BET nitrogen
adsorption method.

In discussing their method, Fu and Bartell (42) states: "It is also
conceivable that, with suitable interpretations, this method can be
utilized to study the expansion or deformation of porous materials
caused by adsorption of various vapors." Sodium montmorillonite is a
porous material which undergoes expansion with adsorption of water vapor;
so it was felt that an analysis (33,97) similar to that of Fu and
Bartell (42) would be instructive. Therefore, the values of the integral

$$\int_{o}^{p/p_o} \frac{q}{p/p_o} \, d(p/p_o),$$

for increasing increments of p/p_o up to and including the saturation
point, were determined by the graphical integration of $\frac{q}{p/p_o}$ versus p/p_o
plot where $\frac{q}{p/p_o}$ was plotted on the ordinate axis and p/p_o was plotted
on the abscissa axis. The data of the adsorption isotherm were taken
from Roderick's investigation (97). The values from the graphical inte-
gration are multiplied by $-\frac{RT}{M} = -\frac{(8.314 \times 10^7)(297.5)}{18.02}$ to obtain
the free energy changes, $\Sigma\Delta F$ ergs/gm of sodium montmorillonite, due to
adsorption to a relative pressure of p/p_o. The values of $\Sigma\Delta F$ obtained
from Roderick's and Demirel's investigation are presented in Table 6.
These values were obtained by the method of graphical integration as out-
lined above.

Plots of log ($\Sigma\Delta F$) versus log (p/p_o) are presented in Figure 19 for

Table 6. Free energy changes per gram of sodium montmorillonite due to adsorption of water vapor (after Roderick, 97)

	Free energy change $(-\Sigma\Delta F)$, ergs/gm	
p/p_o	Sample No. 1[a] Roderick's study	Sample No. 2 Demirel's study
0.01	1.20×10^7	0.46×10^7
0.02	2.01	0.83
0.03	2.55	1.11
0.04	3.02	1.35
0.05	3.38	1.56
0.06	3.69	1.76
0.07	3.97	1.94
0.08	4.23	2.11
0.09	4.46	2.27
0.10	4.68	2.42
0.12	5.09	2.72
0.14	5.47	3.01
0.16	5.82	3.29
0.18	6.16	3.56
0.20	6.49	3.83
0.22	6.82	4.12
0.24	7.11	4.41
0.26	7.50	4.72

[a]This sample is the same as used in the present study.

Table 6.   (Continued)

p/p_o	Free energy change $(-\Sigma\Delta F)$, ergs/gm	
	Sample No. 1[a] Roderick's study	Sample No. 2 Demirel's study
0.28	7.85×10^7	5.04×10^7
0.30	8.21	5.38
0.34	9.01	6.13
0.38	9.90	6.94
0.42	10.78	7.81
0.46	11.75	8.71
0.50	12.70	9.61
0.54	13.66	10.55
0.58	14.62	11.54
0.62	15.78	12.57
0.66	16.93	13.69
0.70	18.19	14.89
0.75	19.88	16.49
0.80	21.63	18.18
0.85	23.52	19.95
0.90	25.46	21.83
0.95	27.54	23.92
0.98	29.03	25.27
1.00	30.33	26.44

Figure 19. Log-log plot of free energy change versus the relative pressure of water vapor for sodium montmorillonite, first adsorption run (after Roderick, 97)

Roderick's data and in Figure 20 for Demirel's data. Omitting the low

p/p_o portion which contains inaccuracy, each of the plots displays three

straight-line portions (implying equations of the type $\Sigma\Delta F = \alpha(p/p_o)^\beta$

for various portions) rather than two obtained by Fu and Bartell (42).

The significant characteristics of the plots have been described in

detail by Roderick (97). By combining the free energy change data of

Roderick (97) and of Demirel (33) with the X-ray data of the adsorption

run in this study, the free energy change involved in the expansion of

the basal spacing can be determined.

According to the previous discussion, composite peaks can be

resolved into two normal peaks. It is informative to derive an expression

showing the total free energy change per gram of sodium montmorillonite

for the whole peak is equal to that for the most probable peak under the

composite peak.

In the present system sodium montmorillonite clay consists of

platelets of different basal spacings. The equilibrium equation showing

the reaction of clay with distribution of structures (or spacings) with

water can be drawn as

$$\text{Clay with distributions of structures } (P_{H_2O} = 0) + \frac{q_{total}}{M} \ H_2O \ (\text{at } P_{H_2O}) \rightarrow$$

$$\text{Clay with distribution of structures } (\text{at } P_{H_2O}) \quad .$$

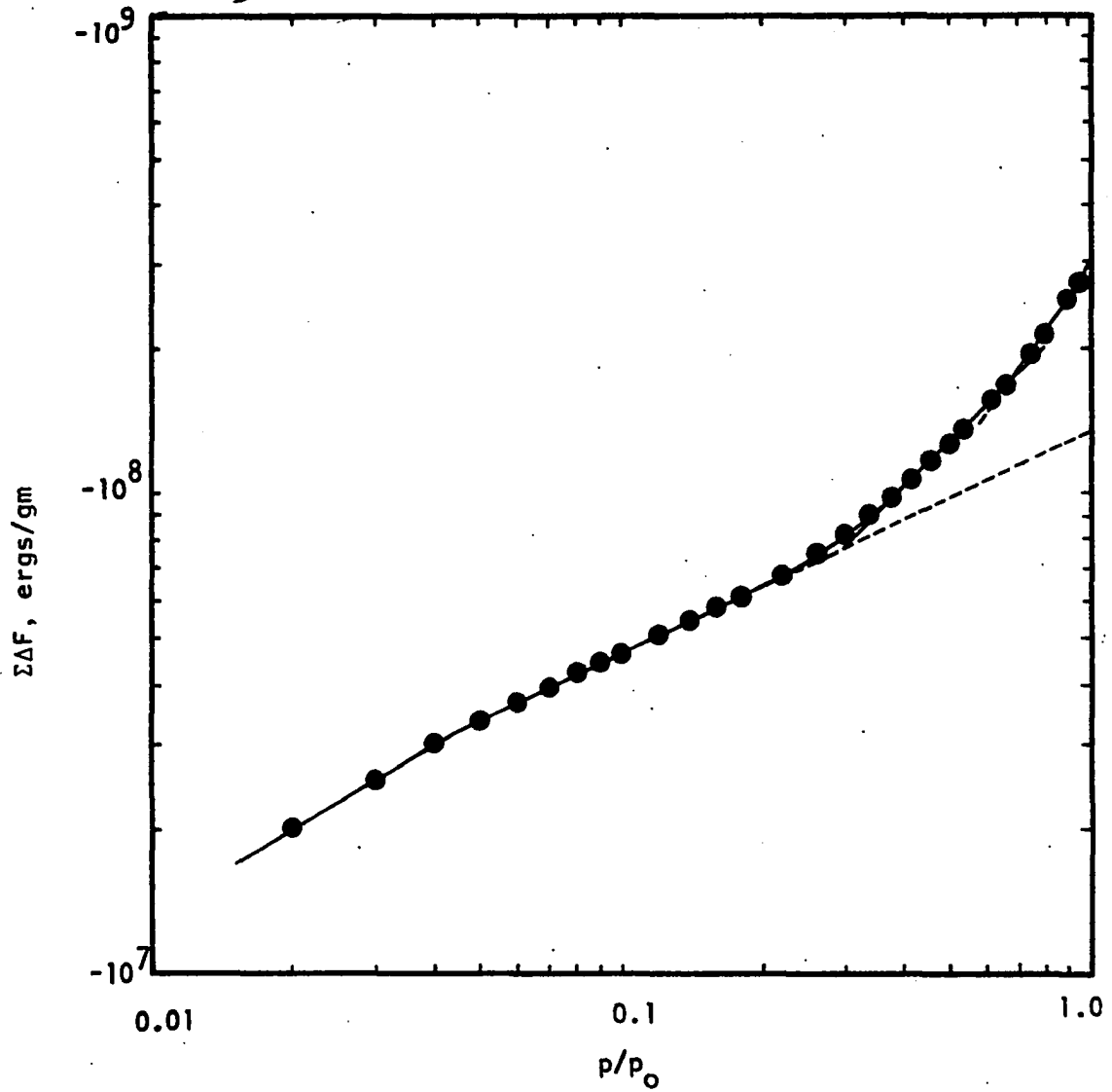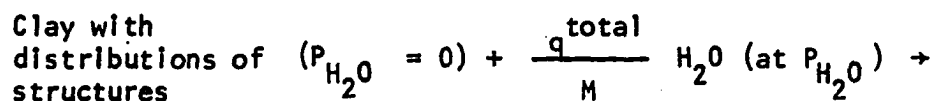Assume that H_2O (g) and H_2O everywhere in the clay are in

equilibrium, so
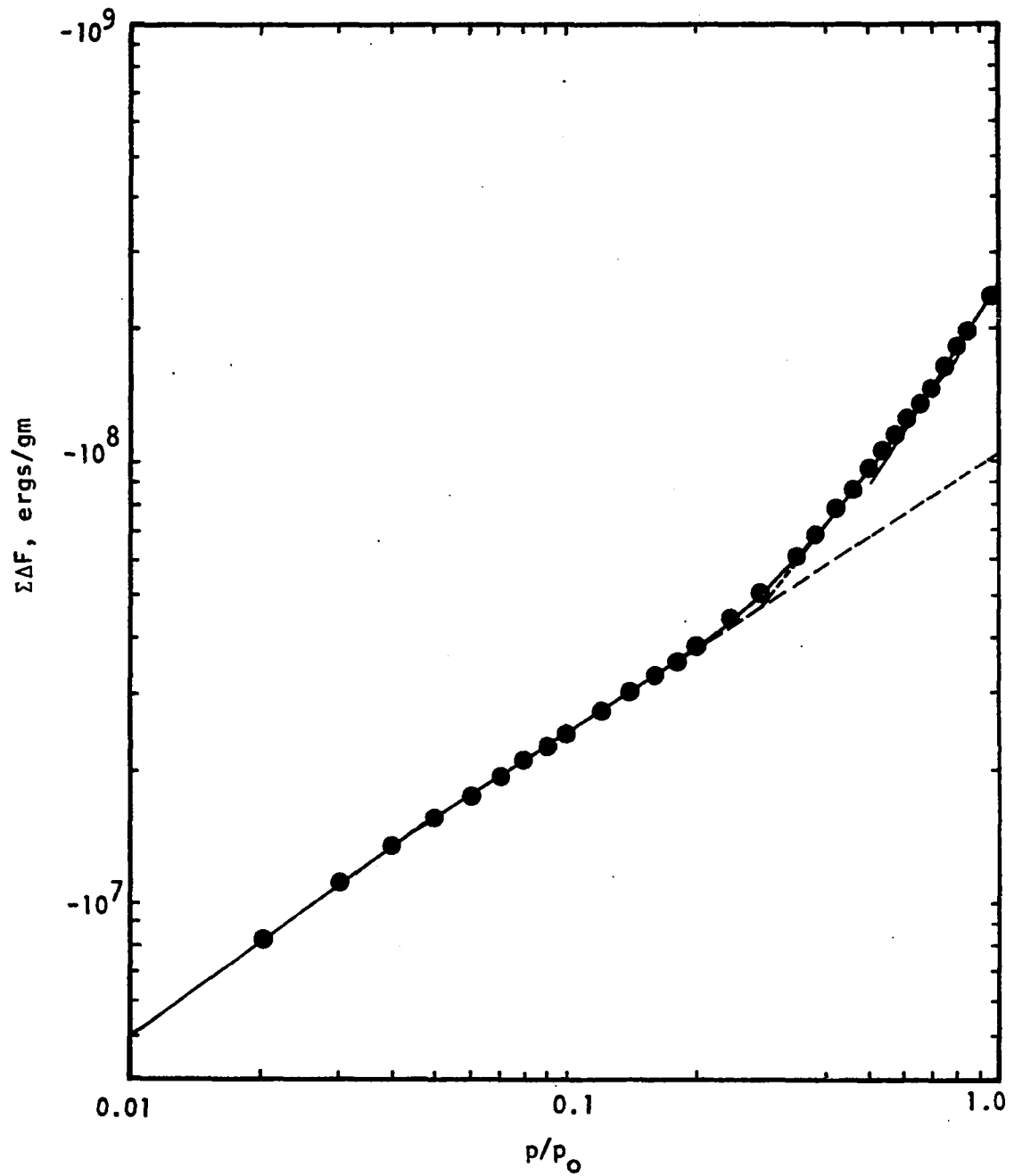
Figure 20. Log-log plot of free energy change versus the relative pressure of water vapor for sodium montmorillonite, adsorption run (after Demirel, 33)

$$\mu_{H_2O}^g \;=\; \mu_{H_2O}^{clay} \tag{a}$$

and

$$\frac{\partial F^{solid}}{\partial n_{H_2O}^{solid}}\Bigg)_{T,P,n_{clay}} = \mu_{H_2O}^{clay} = \mu_{H_2O}^g \tag{b}$$

By Integration

$$F^{solid}(P_{H_2O}) - F^{solid}(P_{H_2O} = 0) = \int_{P_{H_2O}=0}^{P_{H_2O}} \mu_{H_2O}^g \, dn_{H_2O}$$

$$= n_{H_2O}\,\mu_{H_2O}^g \Bigg|_{P_{H_2O}=0}^{P_{H_2O}} - \int_{P_{H_2O}=0}^{P_{H_2O}} n_{H_2O}\, d\mu_{H_2O}^g$$

At pressure of P_{H_2O}, $\quad n_{H_2O}\mu_{H_2O} = n_{H_2O}\mu_{H_2O}^{0,g} + n_{H_2O}RT\ln P_{H_2O}$

$$= F^{H_2O}(P_{H_2O}) \tag{c}$$

At $P_{H_2O} = 0$, $\quad n_{H_2O}\,\mu_{H_2O}^g = \lim_{n_{H_2O}\to 0} (n_{H_2O}\,\mu_{H_2O}^{0,g})$

$$+ RT \lim_{n_{H_2O}\to 0} (n_{H_2O}\ln P_{H_2O})$$

At low pressure or low n_{H_2O}, $P_{H_2O} = kn_{H_2O}$ (Henry's law)

$$\lim_{n_{H_2O} \to 0} n_{H_2O} \ln P_{H_2O} = \lim_{n_{h_2O} \to 0} n_{H_2O} \ln n_{H_2O}$$

$$\lim_{x \to 0} x \ln x = 0$$

So $\lim_{n_{H_2O} \to 0} n_{H_2O} \ln P_{H_2O} = 0$

Then $F^{solid} (P_{H_2O}) - F^{solid} (P_{H_2O} = 0) - F^{H_2O} (P_{H_2O})$

$$= - \int_{P_{H_2O}}^{P_{H_2O}} n_{H_2O} \, d\mu^g_{H_2O} \tag{d}$$

But

$$\mu^g_{H_2O} = \mu^0_{H_2O} + RT \ln P_{H_2O}$$

Therefore $\qquad d\mu^g_{H_2O} = RT \dfrac{dP_{H_2O}}{P_{H_2O}}$

Then

$$F^{solid}(P_{H_2O}) - F^{solid}(P_{H_2O} = 0) - F^{H_2O}(P_{H_2O})$$

$$= -RT \int_{P_{H_2O} = 0}^{P_{H_2O}} n_{H_2O} \frac{dP_{H_2O}}{P_{H_2O}} \tag{e}$$

Because

$$F^{solid}(P_{H_2O}) - F^{solid}(P_{H_2O} = 0) - F^{H_2O}(P_{H_2O}) = \Sigma \Delta F$$

Therefore

$$\Sigma \Delta F = -RT \int_{P_{H_2O}=0}^{P_{H_2O}} n_{H_2O} \frac{d\,P_{H_2O}}{P_{H_2O}} \tag{f}$$

but $q = n_{H_2O} M$ and let $P_{H_2O} = p$

Then

$$\Sigma \Delta F = -\frac{RT}{M} \int_0^P q \frac{dp}{p}$$

$$= -\frac{RT}{M} \int_0^{p/p_o} q \frac{d(p/p_o)}{p/p_o}$$

$$= -\frac{RT}{M} \int_0^{p/p_o} q \, d(\ln p/p_o)$$

$$= -\frac{RT}{M} \int_{o}^{p/p_o} \sum_i q_i d(\ln p/p_o) \quad \text{where i is a}$$

spacing index.

$$\Sigma \Delta F = -\frac{RT}{M} \left(\sum_i \int_{o}^{p/p_o} q_i d(\ln p/p_o) \right) \qquad (g)$$

This must hold for each spacing independently, therefore

$$\Sigma_i (\Delta F)_i = -\frac{RT}{M} \int_{o}^{p/p_o} q_i d(\ln p/p_o)$$

Assuming that $q_i/\Sigma_i \simeq$ constant

$$\text{Then} \quad \Delta F_i \simeq -\frac{RT}{M} \int_{o}^{p/p_o} \frac{q_i}{\Sigma_i} d(\ln p/p_o) = \text{constant} \qquad (h)$$

and Equation (h) holds for all spacings. Let $\Delta F_i = \Delta F_{mp}$, the free energy change for the most probable spacing. Then by combining Equations (g) and (h),

$$\Sigma \Delta F = (\Sigma_1 + \Sigma_2 + \ldots \Sigma_i) \Delta F_{mp}$$

where i = mp for the most probable spacing. Then

$$\Sigma \Delta F = \Sigma \Delta F_{mp} \qquad (i)$$

$q_i/\Sigma_i \simeq$ constant if the principal structural differences are be-tween the planes and not within the planes. This implies that q_i/Σ_i is nearly the same for the resolved basal spacings at relative pressure p/p_o. Under these conditions $\Delta F_{mp} = \Delta F$ for the total system. The importance of

the approximation $q_i/\Sigma_i \simeq$ constant diminishes with the distribution of spacings. The assumption that

$$\mu_{H_2O}^{clay} = \mu_{H_2O}^{g}$$

is essential to the thermodynamic treatment of the data.

The combination of the X-ray diffraction data of the present study and the free energy change data is shown in Table 7. In this Table the reduced values of the free energy change, $\Sigma\Delta F$, from the interpolation of Table 6 for Roderick's data are shown. The relationship between the free energy change of adsorption and the interlayer separation of the clay platelets is shown in Figure 21. The average unresolved platelet separation, h, at the same p/p_o for each $\Sigma\Delta F$ are obtained from Table 2 and Figure 13a. Figure 21 exhibits sharp breaks in the $\Sigma\Delta F$ versus h plot which corresponds closely with the slope change noted in Figure 19. The breaks occur at interlayer spacings of 12.7, 15.5 and 19.0 $\overset{o}{A}$, corresponding to layer separation distances, h, of 2.8, 5.6 and 9.1 $\overset{o}{A}$ if a collapsed basal spacing of sodium montmorillonite of 9.9 $\overset{o}{A}$ is assumed. The first two h values are very nearly integral multiples of 2.8 $\overset{o}{A}$, the diameter of a water molecule, giving additional evidence that the interlayer water builds up in a laminar fashion. The last two figures are consistent with the data from Figure 15, i.e. 12.3, 15.5 and 19.0 $\overset{o}{A}$. Complicating this interpretation, Demirel (33) and Roderick (97) obtained the first basal spacing, before introducing the vapor pressure, of 9.8 $\overset{o}{A}$. The first basal spacing of sodium montmorillonite thus may depend on the duration of evacuation and water entrapped in the clay.

Table 7. X-ray diffraction data and free energy changes for the absorption run

p/p_o	Unresolved d_{001} spacing $\overset{o}{A}$	$\Sigma \Delta F^a$ ergs/gm	h^b $\overset{o}{A}$	$\Sigma_e \Delta F^c$ ergs/gm	$\Sigma_i \Delta F^d$ ergs/gm
0.00	9.9	-1.2×10^7	0	-1.2×10^7	0
0.04	9.9	-3.02	0	-3.02	0
0.08	9.9	-4.23	0	-4.23	0
0.17	9.9	-5.99	0	-5.99	0
0.28	10.2	-7.68	0.3	-7.60	-0.08×10^7
0.31	10.3	-8.21	0.4	-8.00	-0.21
0.33	10.9	-8.81	1.0	-8.30	-0.51
0.34	11.1	-9.01	1.2	-8.50	-0.51
0.39	11.3	-10.12	1.4	-9.00	-1.12
0.42	11.4	-10.78	1.5	-9.30	-1.48
0.47	11.9	-11.99	2.0	-9.80	-2.19
0.50	12.0	-12.70	2.1	-10.10	-2.60
0.55	12.2	-13.90	2.3	-10.50	-3.40
0.58	12.3	-14.62	2.4	-10.80	-3.82
0.63	12.5	-16.07	2.6	-11.10	-4.97

[a] $\Sigma\Delta F$ = total free energy change interpolated from Table 6.

[b] h = interlayer separation.

[c] $\Sigma_e \Delta F$ = free energy change for external surface area interpolated from Figure 19.

[d] $\Sigma_i \Delta F$ = $\Sigma\Delta F - \Sigma_e\Delta F$ = free energy change for internal surface.

Table 7. (Continued)

p/p_o	Unresolved d_{001} spacing Å	$\Sigma\Delta F^a$ ergs/gm	h^b Å	$\Sigma_e\Delta F^c$ ergs/gm	$\Sigma_1\Delta F^d$ ergs/gm
0.65	12.6	-16.35×10^7	2.7	-11.20×10^7	-5.15×10^7
0.71	13.9	-18.53	4.0	-11.90	-6.63
0.73	14.5	-19.21	4.6	-12.00	-7.21
0.75	14.9	-19.88	5.0	-12.30	-7.58
0.79	15.2	-21.28	5.3	-12.50	-8.78
0.82	15.2	-22.39	5.3	-12.70	-9.69
0.84	15.4	-23.15	5.5	-12.90	-10.25
0.91	15.5	-25.88	5.6	-13.20	-12.68
0.93	15.5	-26.72	5.6	-13.40	-13.32
0.96	15.5	-28.04	5.6	-13.60	-14.44
0.97	18.8	-28.54	8.9	-13.70	-14.48
1.00	19.0	-30.33	9.1	-14.00	-16.33
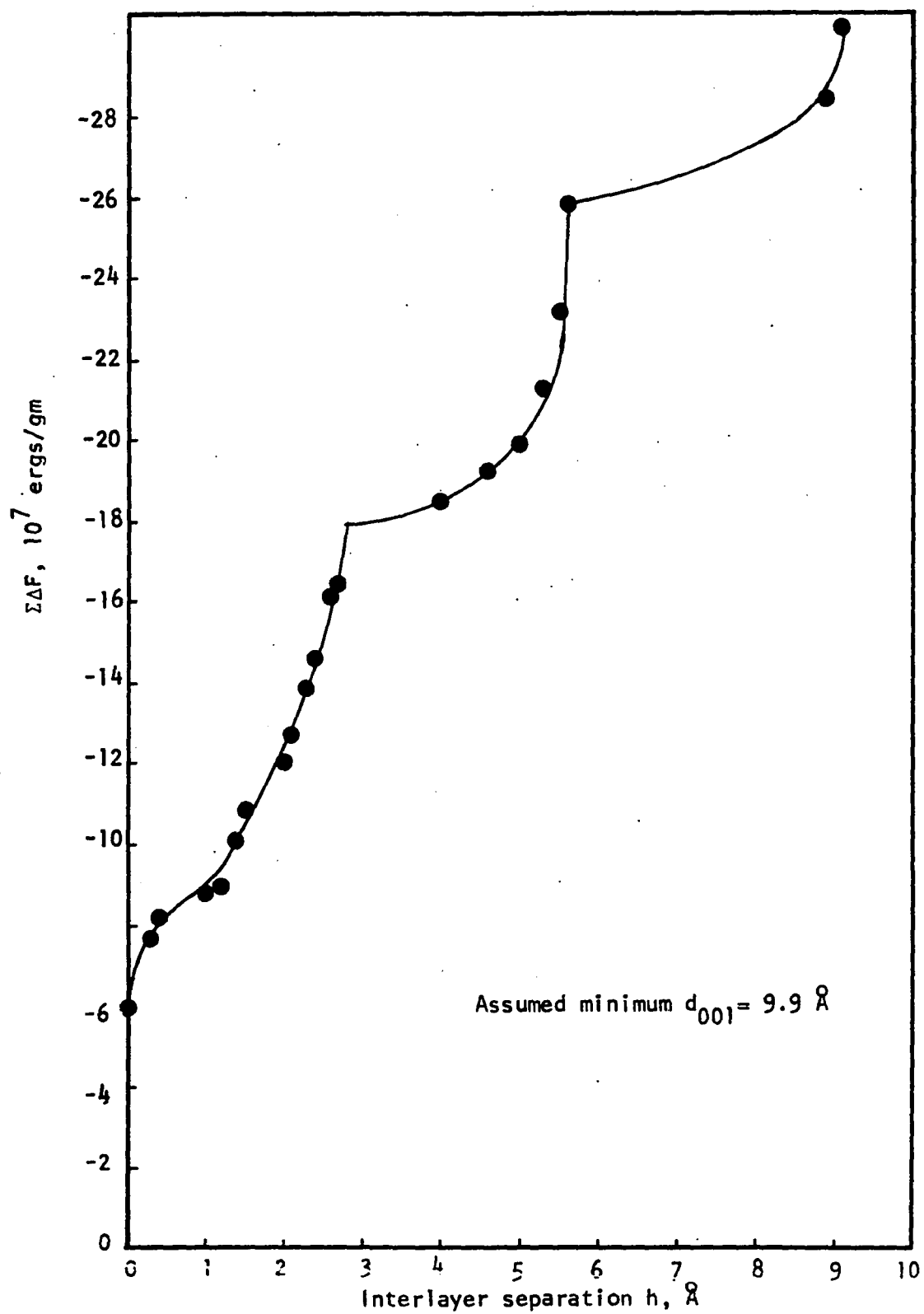
Figure 21. Plot of total free energy change versus interlayer separation for the adsorption run

Figure 21 shows that the free energy change due to adsorption on the external surface before interlayer expansion begins is about -6×10^7 ergs/ gm for sodium montmorillonite. The free energy change for adsorption during the first state of hydration is about $-(17.9-6) \times 10^7 = -11.9 \times 10^7$ ergs/gm, the free energy change during the second state of hydration is about -8.0×10^7 ergs/gm, and during the third state of hydration is about -4.4×10^7 ergs/gm. These free energy changes include that due to additional adsorption on the external as well as the internal surfaces of sodium montmorillonite. The free energy changes for various states of hydration are in the same order as those obtained by Roderick (97).

Expansion energies

If the free energy changes could be divided into two components, one for adsorption on external surfaces and another for adsorption on internal surfaces, it would be possible to evaluate the expansion energies, i.e. the free energy change due to adsorption on and separation of the internal surfaces.

The free energy change brought about by the adsorption, on a solid surface, of a film at equilibrium with a vapor at some pressure p may be expressed as

$$\Delta F = \gamma_{sv} - \gamma_{so} \quad \text{ergs/cm}^2 \tag{9}$$

where γ_{so} is the surface free energy of the solid surface in vacuum and γ_{sv} is that of the solid-vapor interface in equilibrium at pressure p (1, p. 264). When the solid-vapor interface is in equilibrium with the saturated vapor the free energy change is

$$\Delta F = \gamma_{sv^\circ} - \gamma_{so} \quad \text{ergs/cm}^2 \tag{10}$$

where γ_{sv° is the surface free energy of the solid-vapor interface at the saturation pressure p_o. According to Jura and Harkins (58) and to Boyd and Livingston (15), where a solid is wetted by liquid, γ_{sv° is equal to $(\gamma_{sl} + \gamma_{lv})$, γ_{sl} is the solid-liquid interfacial free energy and γ_{lv} is the surface free energy of the liquid in equilibrium with its own vapor. We have, therefore, at saturation:

$$\Delta F = \gamma_{sl} - \gamma_{so} + \gamma_{lv} \quad \text{ergs/cm}^2 \; . \tag{11}$$

If capillary condensation occurs the γ_{lv} term drops out of Equation (11). For the system of the present study the adsorption occurs only on the external surfaces of the clay at low relative pressures. In the relative pressure range of 0.05 to 0.18, the linear plot of log ($\Sigma\Delta F$) versus log (p/p_o) implies that the curve may be expressed by an equation of the type $\Sigma\Delta F = \alpha(p/p_o)^\beta$. Since only external areas Σ_e are involved, the free energy change is given by Equation (9) as

$$\Sigma_e \Delta F = \Sigma_e (\gamma_{sv} - \gamma_{so}) \quad \text{ergs/gm} \tag{9a}$$

If only the external areas were available for adsorption over for the entire relative pressure range it is proposed that the relationship $\Sigma_e \Delta F = \alpha(p/p_o)^\beta$ would continue to be obeyed. Under these circumstances the linear portion of the log ($\Sigma\Delta F$) versus log (p/p_o) plot between relative pressure of 0.05 to 0.20 would be extended to a p/p_o of 1.0 as shown by the dashed lines on Figure 19. The free energy change at saturation given by Equation (11) is:

$$\Sigma_e \Delta F = \Sigma_e (\gamma_{sl} - \gamma_{so} + \gamma_{sl}) \text{ ergs/gm} .$$ (11a)

If capillary condensation were to occur (still only external surface available), a behavior such as that observed by Fu and Bartell (42) would be expected. For a given adsorbate-adsorbent system, α and β remain constant so long as there is no change in the mechanism of adsorption. If changes in the mechanism of adsorption, such as capillary condensation or swelling occurs, values of α and β change to another set of constant values (42). According to Equation (11a) when there is capillary condensation the free energy change at saturation would be reduced by $\Sigma_e \gamma_{lv}$. With the present system this probably occurs very near the saturation pressure and cannot be located by log $(\Sigma \Delta F)$ versus log (p/p_o) plot.

On the basis of the above discussion, the free energy changes due to adsorption on external and on internal surfaces were divided, at least in the near-saturation region, by extending the linear portion of the plot in Figure 19 from $p/p_o = 0.05$ to the saturation presence (data from $p/p_o = 0.01$ to $p/p_o = 0.05$ are omitted due to inaccuracy of measuring the q-values). This linear portion of the plot in Figure 19 corresponds to the free energy change due to adsorption on the external surfaces. This is consistent to the X-ray data that no significant change in basal spacing occurs in this region from $p/p_o = 0$ to $p/p_o = 0.20$, and there is a slope change in Figure 19 at $p/p_o = 0.20$ indicating the change in mechanism of adsorption. The change in slope at $p/p_o = 0.20$ is due to the interlayer adsorption. The difference between $\Sigma \Delta F$ and $\Sigma_e \Delta F$ gives the free energy change $\Sigma_i \Delta F = \Sigma_i \phi$, where Σ_i is the internal surface area per gram and ϕ will be designated as the expansion energy per cm^2 of internal

surface and is given by:

$$\phi = \gamma_{sv} - \gamma_{so} + \Delta V \tag{12}$$

where ΔV is the free energy change per cm^2 of internal surface due to separation of layers against the force of interaction (92). The expansion energy ϕ can also be obtained by the expression

$$\phi = \frac{\Sigma \Delta F - \Sigma_e \Delta F_e}{\Sigma_i} \tag{13}$$

Figure 22 presents a plot of $\Sigma_i \phi$ obtained from Figure 21 for the adsorption versus platelet separation. Figure 22 is quite similar to Figure 21. The value of $\Sigma_i \phi$ is about -6×10^7 ergs/gm for the first expansion increment and decreases to about -12.7×10^7 ergs/gm and -16.3×10^7 ergs/gm for the second and the third expansion increments, respectively. Figure 22 shows that the free energy change due to the second state of hydration is as great as or slightly greater than that for the first state of hydration. The free energy change for the third state of hydration is substantially less than that for the other two. The reasons for the difference of the expansion energy can be given as follows. The expansion energy ϕ for the first state of hydration is the free energy change due to the disappearance of a solid surface and the formation of a solid-film interface plus that due to expansion against the interaction energy ΔV_1 when the clay platelets are in contact. The latter term will decrease the magnitude of the free energy change. In the second state of hydration, water must penetrate between the first water layer and the clay surface. No new surfaces are formed nor do any disappear. The free
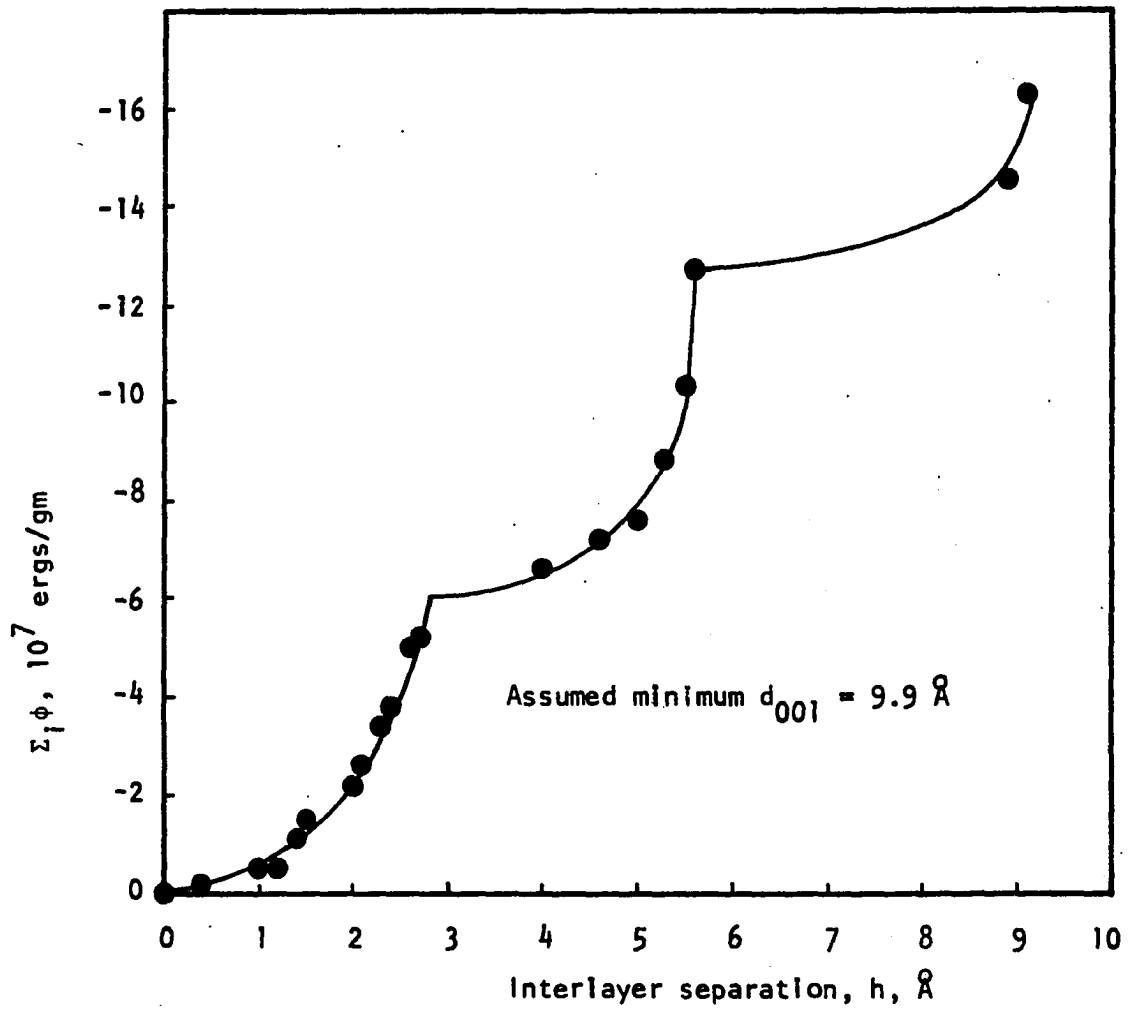
Figure 22. Plot of free energy change due to adsorption on
internal surfaces versus interlayer separation
for the adsorption run

energy change is due to extension of the film thickness and to the expansion against the interaction energy ΔV_2 when the clay platelets are separated by a layer of water after the first state of hydration. Again, the latter term decreases the magnitude of the free energy change. The free energy change due to the extension of the film thickness is probably less than that for disappearance of solid surfaces and formation of solid-film interface for the first state of hydration. However, since the platelet separation is greater, ΔV_2 is probably less than ΔV_1 and so the free energy change for the second state of hydration may be nearly the same as that for the first state. For the third state of hydration water may penetrate between the clay surface and existing interlayer water, but most probably enters between the layers of water for the first and second states of hydration. Again, no new surfaces appear and disappear. The free energy change is due to extension of the film thickness and to expansion against the interacting energy ΔV_3 when the clay platelets are separated by a layer of water after the second state of hydration. ΔV_3 is probably less than ΔV_2 and ΔV_1 because of increased separation. Since the free energy change on the hydration of the third state is considerably less than that for the second state, the change due to penetration between the first and second layers of water must be less than that for penetration between the clay surface and a water layer.

Swelling pressures

It was suggested by Roderick and Demirel (98) that there was a relationship between free energy data and swelling pressure exerted by montmorillonites. An estimate of the pressure required to prevent

separation of clay platelets due to the adsorption of water between the layers (or the swelling pressure exerted by the clay particles on uptake of interlayer water) was attempted using the X-ray diffraction and the free energy change data. The data from other investigators (33,80) will also be presented with those in the present study.

In order to attack the problem the thermodynamic relations between pressure and volume will be involved. Senich (101) derived an expression to calculate the swelling pressure from the free energy change data. Assuming that constant temperature is attained and assuming all work to be pressure-volume work, the free energy change can be related to pressure and volume as

$$dF = Vdp \tag{14}$$

where V is the molar volume and p is the external pressure. However, if we consider that the expansion is due only to the adsorption of vapor on the interlayer surfaces, the expansion may be made to read

$$\Sigma_i d\phi = Vdp$$

Assuming water is incompressible, the latter equation can be put into the following form:

$$d\phi = \frac{V}{\Sigma_i} dp = h_o dp \tag{15}$$

where ϕ is the expansion energy (change in free energy due to adsorption on, and separation of internal surfaces) per cm^2; V is the total volume of interlayer water at saturation pressure per gram of sodium montmorillonite; h_o is the maximum platelet separation; and p is the applied pressure. From Equation (15) we obtain:

$$\Sigma_i \int_{\phi=\phi_s}^{\phi} d\phi = \Sigma_i \int_{p=0}^{p} h_o dp \tag{16}$$

$$\text{or} \quad \Sigma_i \phi - \Sigma_i \phi_s = \Sigma_i h_o p$$

$$\text{or} \quad p = \frac{\Sigma_i \phi - \Sigma_i \phi_s}{h_o \Sigma_i} \tag{17}$$

where ϕ_s is the expansion energy when the clay is in equilibrium with saturated water vapor, p is the pressure required to prevent any platelet separation, and p = 0 is the pressure when maximum separation is reached.

The numerical values of swelling pressure can be calculated by assigning the appropriate internal area, Σ_i, per gram of sodium mont-morillonite in the above expression. The external areas, Σ_e, are determined from the adsorption isotherm data by Roderick (97). Table 8 presents the external areas, Σ_e, obtained from the adsorption run by using Equation (1) for various cross-sectional areas of the water molecules. The total surface area Σ is obtained from crystallographic data. The procedure to determine the total surface area from crystallographic data is shown in Appendix I. The area occupied per molecule for a closest packing arrangement is commonly used in surface area determinations; the corresponding area per water molecule would be 10.8 $\overset{o}{A}^2$. The data of the present study show that the interlayer water arranges in a laminar manner; the arrangement proposed by Hendricks and Jefferson (49) gives an area of about 11.5 $\overset{o}{A}^2$ per water molecule. On the other hand, Demirel (33) obtained a

Table 8. External surface areas per gram of sodium montmorillonite
calculated from water vapor adsorption data[a]

Cross-sectional area per water molecule, Å^2	External surface area Σ_e, m^2/gm $q_m = 0.023$
10.8^b	83.0
11.5^c	88.3
17.5^d	134.4
7.7^e	59.2

[a]Data obtained from Roderick (97, p. 87).

[b]Based on closest packing.

[c]Based on arrangements of Hendricks and Jefferson (49) and Barshad (9).

[d]Based on ice structure (33).

[e]Based on arrangement of Barshad (9).

cross-sectional area of about 17.5 Å^2 per water molecule from the combination of his X-ray and adsorption data which pointed out the ice structure of the adsorbed water. For the sake of comparison, all the areas of the water molecule mentioned are used to determine the internal surface areas, Σ_i, which are then used to determine the swelling pressure for various states of hydration.

The swelling pressures of sodium montmorillonite on the adsorption of water vapor for various degrees of adsorption are shown in Table 9. In this table the value of internal surface area, Σ_i, of 665 m^2/gm is assigned for reason of the laminar arrangement of the water molecules. Figure 23 presents a curve showing the relationship between swelling pressure and platelet separation. The breaks along the curve indicate the completeness of one state of hydration and the beginning of the succeeding state. The value of $\Sigma_i\phi_s$ used in the calculation of the swelling pressure is -16.33 ergs/gm (last figure of column 6 Table 7). From Figure 23 it is clear that the swelling pressure of sodium montmorillonite-water vapor system for the completeness of the first state of hydration and the second state are 179 and 63 tons/ft^2, respectively. When the third state of hydration has been completed the swelling pressure reduces to zero. The highest swelling pressure for the beginning of the hydration of the first state is 282 tons/ft^2. These values of swelling pressure are based on the laminar arrangement of interlayer water whose molecular area is 10.8 Å^2. Table 10 shows the expansion energy and swelling pressure due to adsorption of water vapor for sodium montmorillonite when different values of the molecular area of water are

Table 9. Swelling pressures of sodium montmorillonite due to adsorption of water vapor at various relative pressures

p/p_o	d_{001} spacing Å	h Å	$\Sigma_i \phi$ ergs/gm	$\Sigma_i \phi - \Sigma_i \phi_s$ ergs/gm	Swelling pressure $p = [\dfrac{\Sigma_i \phi - \Sigma_i \phi_s}{h_o \Sigma_i}]^a$ dynes/cm^2	Swelling pressure tons/ft^2
0.00	9.9	0	0	16.33×10^7	270×10^6	282
0.04	9.9	0	0	16.33	270	282
0.08	9.9	0	0	16.33	270	282
0.17	9.9	0	0	16.33	270	282
0.28	10.2	0.3	-0.08×10^7	16.25	269	281
0.31	10.3	0.4	-0.21	16.12	266	278
0.33	10.9	1.0	-0.51	15.82	261	273
0.34	11.1	1.2	-0.51	15.82	261	273

$^a\Sigma_i$ = Internal surface area of sodium montmorillonite in m^2/gm = 665 m^2/gm,

$\Sigma_i \phi_s$ = Expansion energy when the clay is in equilibrium with saturated water vapor

= -16.33 ergs/gm (last figure of column 4),

h_o = maximum platelet separation when the clay is in equilibrium with saturated water vapor

= 9.1 Å.

Table 9. (Continued)

p/p_o	d_{001} spacing $\mathring{A}$	h $\mathring{A}$	$\Sigma_i \phi$ ergs/gm	$\Sigma_i \phi - \Sigma_i \phi_s$ ergs/gm	Swelling pressure $p = [\dfrac{\Sigma_i \phi - \Sigma_i \phi_s}{h_o \Sigma_i}]a$ dynes/cm^2	Swelling pressure tons/ft^2
0.39	11.3	1.4	-1.12×10^7	15.21×10^7	251×10^6	262
0.42	11.4	1.5	-1.48	14.85	245	256
0.47	11.9	2.0	-2.19	14.14	234	244
0.50	12.0	2.1	-2.60	13.73	227	237
0.55	12.2	2.3	-3.40	12.93	214	223
0.58	12.3	2.4	-3.82	12.51	207	216
0.63	12.5	2.6	-4.97	11.36	188	196
0.65	12.6	2.7	-5.15	11.18	185	193
0.71	13.9	4.0	-6.63	9.70	160	167
0.73	14.5	4.6	-7.21	9.12	151	158
0.75	14.9	5.0	-7.58	8.75	145	151
0.79	15.2	5.3	-8.78	7.55	125	130
0.82	15.2	5.3	-9.69	6.64	110	115
0.84	15.4	5.5	-10.25	6.08	100	104

Table 9. (Continued)

p/p_o	d_{001} spacing Å	h Å	$\Sigma_i \phi$ ergs/gm	$\Sigma_i \phi - \Sigma_i \phi_s$ ergs/gm	Swelling pressure $p = [\dfrac{\Sigma_i \phi - \Sigma_i \phi_s}{h_o \Sigma_i}]^a$ dynes/cm^2	Swelling pressure tons/ft^2
0.91	15.5	5.6	-12.68×10^7	3.65×10^7	60×10^6	63
0.93	15.5	5.6	-13.32	3.01	50	52
0.96	15.5	5.6	-14.44	1.89	31	32
0.97	18.8	8.9	-14.48	1.85	31	32
1.00	19.0	9.1	-16.33	0	0	0
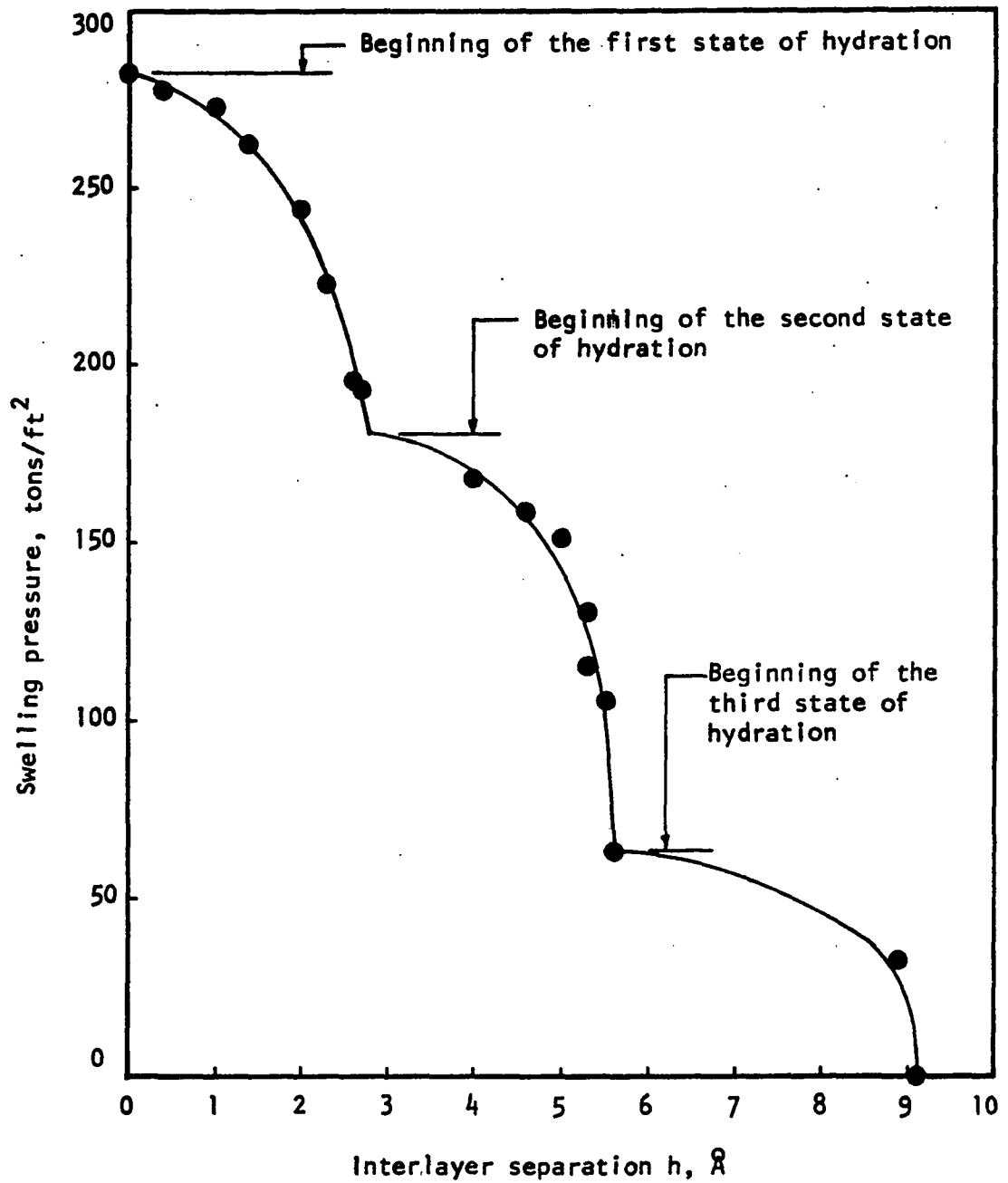
Figure 23. Relationship between swelling pressure and interlayer separation of sodium montmorillonite on adsorption of water vapor

Table 10. Expansion energies and swelling pressures due to adsorption
of water vapor on the interlayer surfaces of sodium mont-
morillonite for various hydration states

Hydration State	Area assigned to a water molecule, Σ_f, Å^2	Internal surface area Σ_f, m^2/gm	Expansion energy, ϕ, ergs/cm^2	Swelling pressure, p, dynes/cm^2	Swelling pressure, p, tons/ft^2
I	10.8	665	--	270×10^6	282
	11.5	660	--	272×10^6	284
	17.5	614	--	292×10^6	305
II	10.8	665	-9.0	171×10^6	179
	11.5	660	-9.0	172×10^6	180
	17.5	614	-9.7	185×10^6	193
III	10.8	665	-19.1	60×10^6	63
	11.5	660	-19.1	60×10^6	63
	17.5	614	-20.4	65×10^6	68
IV	10.8	665	-24.5	--	--
	11.5	660	-24.7	--	--
	17.5	614	-26.5	--	--

assigned in Equation (1). The values of the swelling pressure for the first, second and third states of hydration are shown. The swelling pressure can be obtained from direct calculation by Equation (17) or from Figure 23 (for laminar configuration of interlayer water).

The expansion energy at saturation may be due in part to capillary condensation in external pores. This would tend to make the values given when the third state of hydration has completed are somewhat larger than the actual case; the energy change due to adsorption on internal surfaces during the hydration of the third state would probably be somewhat less than that indicated in Table 10. The expansion energies given in Table 10 for the hydration of the first two states seem not to be affected by capillary condensation.

Van Olphen (110) estimated the pressure required to remove a mono-layer of water from clay surfaces by dividing the free energy change per cm^2 on desorption by the thickness of one molecular layer of water. Using the desorption data of Mooney et al. (79,80), van Olphen (109) found that the net energy required to remove the last few layers of water from clay platelets to be between 50 and 100 ergs/cm^2 for montmorillonite. The estimated equivalent pressure required will be about 2000 tons/ft^2 for an energy change of 50 ergs/cm^2 (see Appendix III). This represents a consolidation pressure rather than a swelling pressure, that is a swelling pressure plus hysteresis. Van Olphen also calculated the pressure required to remove all the water layers from calcium mont-morillonite is about 5300 tons/ft^2. This is equivalent to the free energy change of 140 ergs/cm^2. Applying this procedure to the

adsorption data of the present study, the pressure required to prevent

the uptake of water would be $\Delta F/2.8 \times 10^{-8}$, where $\Delta F = 40.55$ ergs/cm^2 for

the adsorption run (97). This value of free energy change yields a

pressure of about 1534 tons/ft^2 to prevent swelling due to the first

interlayer water (the first hydration state). The difference between the

two pressures may be attributed to hysteresis. The calculation of the

consolidation pressure by van Olphen's method, which does not divide the

free energy change into that due to external adsorption and internal

adsorption, is shown in Appendix III.

In order to consider the swelling pressure solely due to adsorption

on the internal surfaces, the amount of water adsorbed between the unit

cells of sodium montmorillonite is calculated from the X-ray data. The

area of the unit cell is taken as $5.16 \times 8.94 = 46.13$ Å^2, where $a_o =$

5.16 Å and $b_o = 8.94$ Å, a_o and b_o are the dimensions of the sodium mont-

morillonite unit cell. From the X-ray data at various values of relative

pressure the amount of water adsorbed between the unit cell can be calcu-

lated as shown in Table 11. The q-values from the adsorption isotherm

data of Roderick (97) are also included in the Table for comparison.

The relationship between $\dfrac{q_i}{p/p_o}$ versus p/p_o is shown in Figure 24, where

q_i is the amount of water adsorbed between the unit cells of the sodium

montmorillonite and $\dfrac{q_i}{p/p_o}$ is the change in internal adsorption per

change in relative pressure. The drop of $\dfrac{q_i}{p/p_o}$ at $p/p_o = 0.94$ is due

to the insignificant change of the basal spacing as the relative pressure

increases. This happens in the transition zone of the end between the

second state of hydration and the beginning of the third state.

Table 11. Calculated values of internal adsorption between the
platelets of the sodium montmorillonite

$p/p_o{}^a$	q^a gm/gm, 10^{-3}	basal spacing d_{001}, Å	plate separation h, Å	V water cm^3, 10^{-23}	$q_i{}^b$, 10^{-3} gm/gm	$\dfrac{q_i}{p/p_o}$
0.006	5.10	9.89	0.00	0.00	0.00	0.00
0.017	7.81	9.89	0.00	0.00	0.00	0.00
0.022	9.08	9.89	0.00	0.00	0.00	0.00
0.059	12.44	9.90	0.01	0.046	0.377	0.006
0.112	16.33	9.91	0.02	0.092	0.754	0.007
0.150	19.26	9.92	0.03	0.138	1.132	0.008
0.179	22.09	9.93	0.04	0.185	1.517	0.008
0.215	25.72	9.95	0.06	0.278	2.27	0.010
0.259	32.21	10.09	0.20	0.923	7.56	0.029
0.298	30.48	10.44	0.55	2.537	20.76	0.070
0.354	56.08	11.11	1.22	5.630	46.11	0.130
0.425	72.48	11.62	1.73	7.980	65.31	0.154
0.494	87.78	11.97	2.08	9.590	78.52	0.159
0.596	115.80	12.38	2.49	11.490	94.11	0.158
0.665	146.20	12.88	2.99	13.790	112.90	0.170
0.737	183.60	14.67	4.78	22.05	180.51	0.245
0.868	242.30	15.45	5.56	25.65	210.05	0.242
0.939	292.20	15.50	5.61	25.88	211.94	0.226
1.000	512.20	19.04	9.15	42.21	345.68	0.346

[a]Data from Roderick (97).

[b]q_i = internal amount of water between platelet calculated from
plate separation and dimensions of the plate and assuming
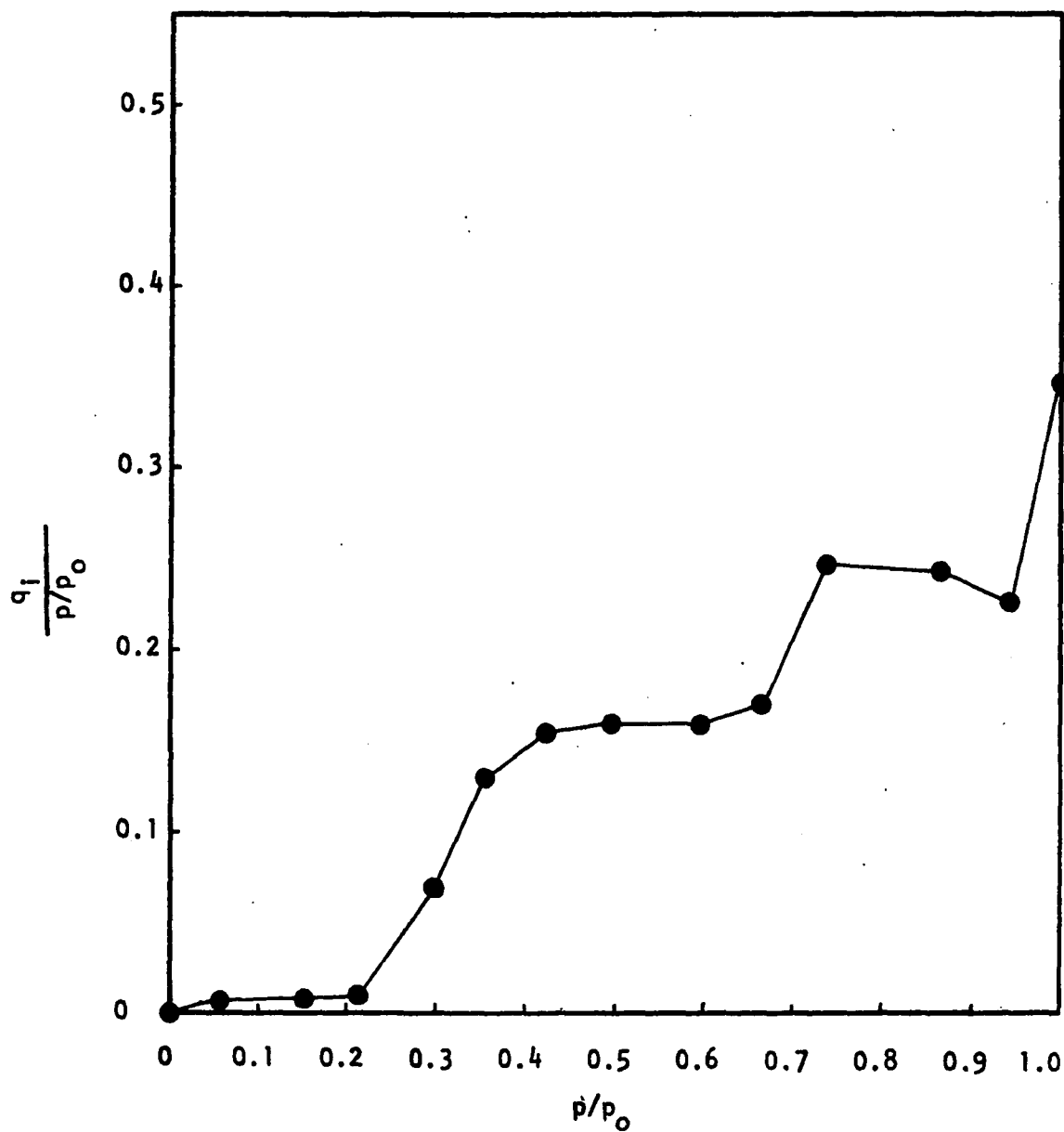that the specific gravity of water at 21.1°C is 0.998 gm/cc.

Figure 24.   Plot for graphical integration of Equation (4)
for the internal adsorption on sodium mont-
morillonite as calculated in Table 11

The free energy change for the internal adsorption is determined by the same method as in Roderick's study and this is shown in Appendix III. The first, second, and third states of hydration are complete at the relative pressures of 0.58, 0.93 and 1.00, respectively. These states of hydration may correspond to the formation of the first, second and third layers of interlayer water. The swelling pressures calculated from the plot of Figure 24 are 930, 611 and 368 tons/ft^2 for the beginning of the first, second and third states of hydration, respectively. Table 12 presents the swelling pressure calculated by van Olphen's method for various conditions using the data of Roderick (97) and Demirel (33) comparing the swelling pressure calculated by the graphical method in this study. The difference between the swelling pressures obtained from Roderick's data and Demirel's data in columns 3 and 4 of Table 12 is due to the difference of the q-values at the same relative pressure for the independent investigations of both studies. Even though at critically controlled temperature and at the same relative pressure, the amount of water adsorbed on and between the platelets was not the same. The variation of the q-values is due to the different manner of adsorption of water vapor on the platelets. The platelets of sodium montmorillonite is extremely thin, the diameter-to-thickness ratio of the platelets varies from 150 to 500 (75). So the platelets behave like a thin flexible film and water has difficulties in penetrating between the platelets. Also pertinent to this discussion is the variation of total surface areas of the clays that will be discussed in detail in the next section. The variation of the swelling

Table 12. Comparison of swelling pressure of montmorillonites obtained from adsorption data by various methods and investigators

Hydration state	Swelling pressure, tons/ft^2					
	Van Olphen's Method			Graphical Method		
	Roderick's data[a]	Roderick's data[b]	Demirel's data[b]	Roderick and Demirel's data[c]	Present study	Senich's data[d]
I	930	1534	1314	313	282	394
II	611	763	713	190	179	280
III	368	476	444	47	63	184

[a]Considering the internal adsorption only, see Figure 24 and Table 11.

[b]Considering both internal and external adsorptions.

[c]Data from Roderick and Demirel (98).

[d]Results for calcium montmorillonite (101).

pressures in columns 5 and 6 of Table 12 is because of the difference in the X-ray data of Roderick and Demirel (98) and of the present study. The results in Table 12 show that swelling pressures calculated by van Olphen's method are many times higher than that calculated by the graphical method. The difference is probably due to the constant stepwise decrease of the swelling pressure as assumed in the van Olphen's method. In the graphical method the swelling pressure decreases in a nonuniform manner and not in a stepwise pattern (see Figure 23). The swelling pressures of calcium montmorillonite calculated by Senich (101) are also presented in the Table for comparison.

Comment on the surface area calculated by other investigators

From the crystallographic data the total surface area is found to be 748 m^2/gm as shown in Appendix I. The data of the surface area from water vapor adsorption obtained by other investigators are shown in Table 13. Those investigators in column 1 of Table 13 reported different values of surface area obtained from water-vapor adsorption on sodium montmorillonite. The values reported in column 3 are considerably different from that calculated from the crystallographic data.

According to Mooney et al. (79), it is found that the area obtained for water adsorption is 440 m^2/gm. This corresponded to the q_m value of 0.112 gm/gm for their data. The X-ray data of others (17,50) and of their own indicate that not more than one layer of water molecules is present between the platelets at this water content. The X-ray data of the present study and the adsorption isotherm data of Roderick (97) showed that only one layer water existing between the platelets of sodium

Table 13. Surface areas of sodium montmorillonite calculated from water-adsorption by various investigators[a]

Investigators	Materials	Areas reported from water-vapor adsorption, m^2/gm	Re-calculated total surface area[b], m^2/gm
Goates and Hatch (44)	Sodium Vol-clay, Wyoming	203	373
Johansen and Dunning (55)	Sodium mont-morillonite	303	573
Orchiston (91)	Sodium mont-morillonite	336	639

[a]The total surface area of sodium montmorillonite calculated from the crystallographic data is 748 m^2/gm (see Appendix I).

[b]External surface area of 33 m^2/gm is assigned to all investigations.

montmorillonite when the q_m is 0.110 gm/gm (interpolation from Roderick's data). This immediately suggests, therefore, that in the case of the expanding-lattice clay, montmorillonite, the BET theory gives not the monolayer capacity on each surface of the expanded platelets but the adsorption of only one layer of molecules occurs between pairs of platelets, plus the small contribution from a monolayer on edges and external surfaces. In the determination of external surface area it is necessary to perform the adsorption isotherm experiment on the sample using nitrogen as an adsorbate. The external surface area can then be calculated by using Equation (1), since nitrogen does not penetrate the interlayer region. Mooney et al. (79) gave the value for nitrogen adsorption as 33 m^2/gm in their study. Because only one molecular layer of interlayer water exists between the platelets of sodium montmorillonite and because water is adsorbed on both internal and external areas, the area obtained from water adsorption represents the external area plus one-half of the internal area. The total surface area from their data then would be calculated as 2(440) - 33 = 847 m^2/gm. Thus, the surface areas reported by others (44,55,91) in Table 13 are not total surface areas, but they are the external area plus one-half of the internal area. The total surface areas can be obtained if the area for nitrogen adsorption is assigned and the calculation is followed as outlined above. Using the value of 33 m^2/gm for nitrogen adsorption, the calculated total surface areas are obtained as shown in column 4 of Table 13.

The calculated total surface areas still vary over a considerable range, and are less than the crystallographic area, 748 m^2/gm. According

to Olson and Mesri (90), the diameter-to-height ratio of montmorillonite

platelet varies from 150 to 500, allowing it to behave like a highly

flexible film. Because of the large area of the plate in comparison to

the plate thickness, it is difficult for the adsorbate to penetrate and

coat all the area between the platelets. Capillary condensation can also

affect the amount of adsorbate penetrating between the platelets such

that the platelets may not be completely covered by the adsorbate. The

source and method of preparation of the sample therefore probably affect

the surface area.

High Pressure X-ray Study

Two samples were tested in the high pressure X-ray goniometer

accessory, one a single crystal of a sodium-tetraphenyl boron-degraded

phlogopite,[1] and the other a sodium montmorillonite.

The peak for the first order basal spacing of the degraded sodium

phlogopite under zero pressure is shown in Figure 25. The basal spacing

of degraded sodium phlogopite is about 14.8 $\overset{o}{A}$. As the pressure was in-

creased there is a slight change in the peak position at 14.8 $\overset{o}{A}$. At the

pressure of 330 tons/ft^2 there appeared another small peak at the basal

spacing of 12.2 $\overset{o}{A}$ as well as the peak at 14.8 $\overset{o}{A}$. The peak at 12.2 $\overset{o}{A}$ then

grew bigger as the pressure increased, while the one at 14.8 $\overset{o}{A}$ decreased.

A typical double peak under pressure is shown in Figure 26. When the

maximum instrument pressure of 3860 tons/ft^2 was reached the peaks

appeared as shown in Figure 27. There is a small change in the peak

_____

[1]Sample supplied by Dr. A. D. Scott, Dept. of Agronomy, Iowa State
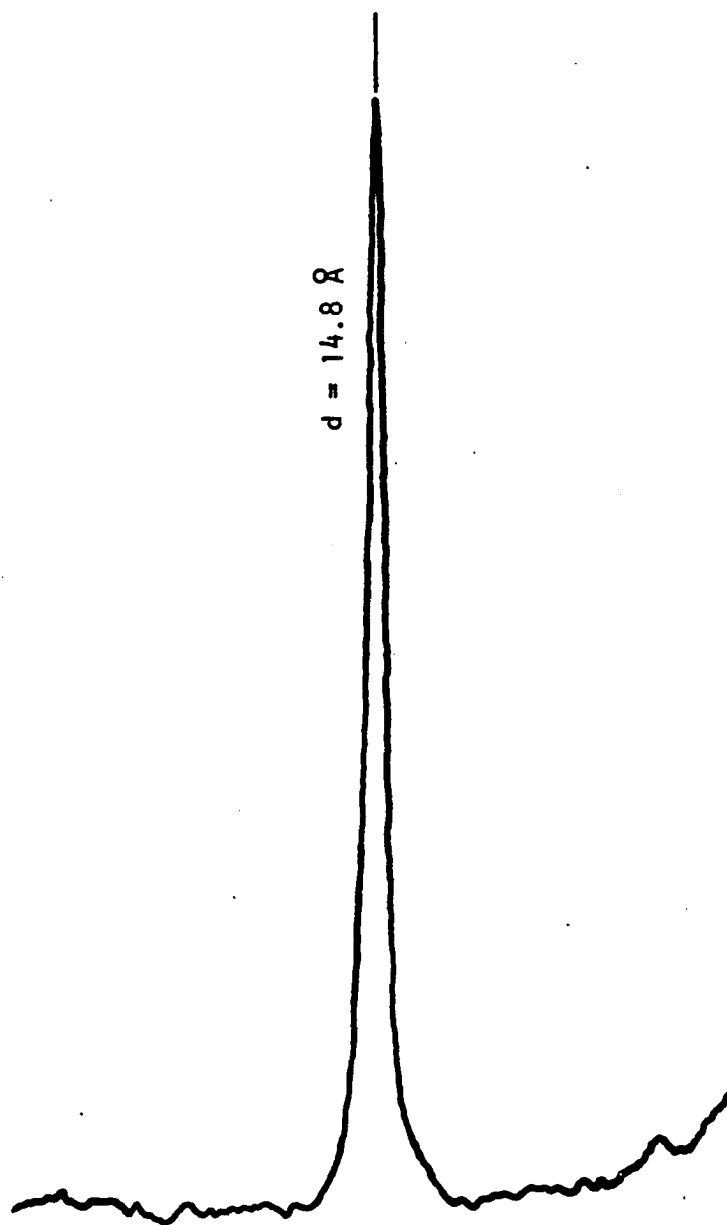University.

d = 14.8 Å

Figure 25. First order peak of the degraded sodium
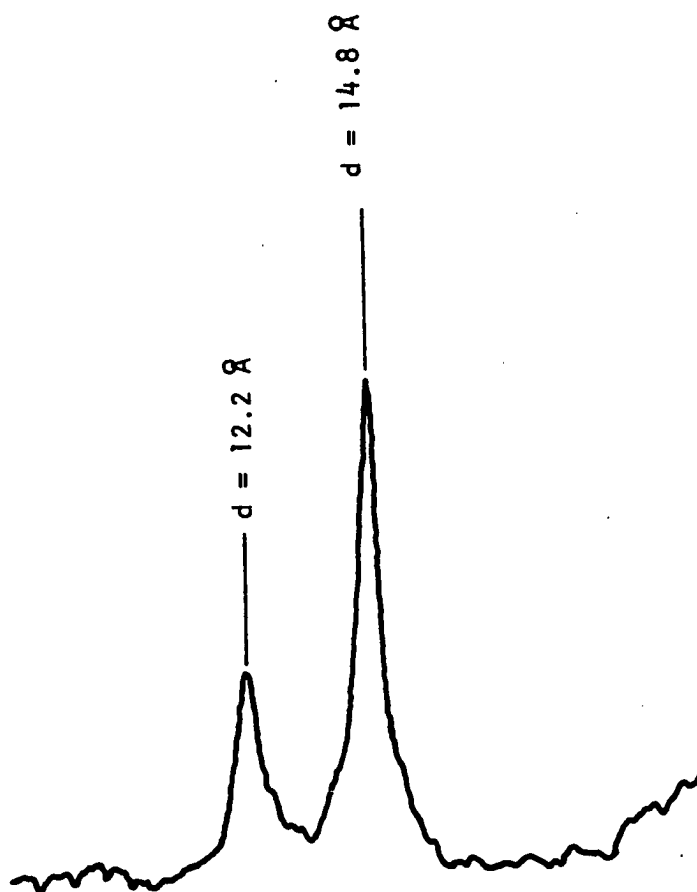phlogopite under zero pressure

Figure 26. Typical double peaks of the degraded sodium phlogopite under pressure
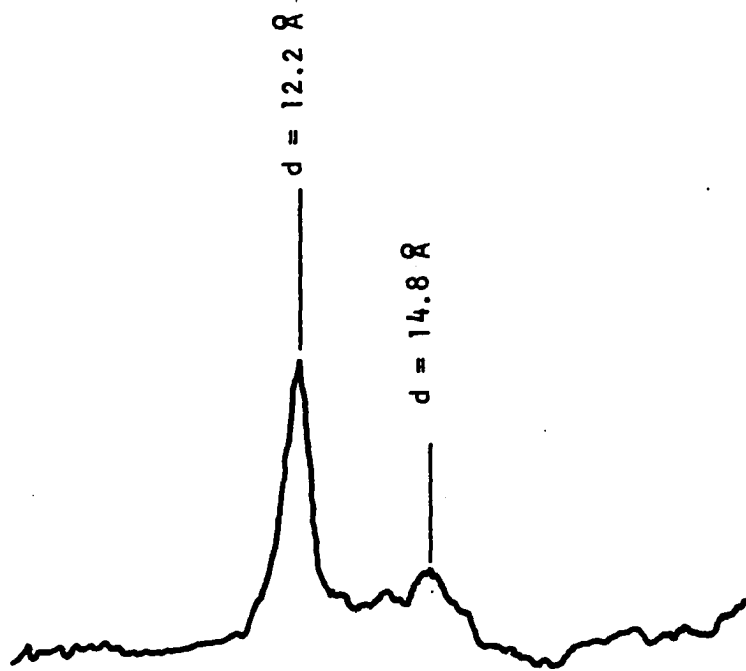
Figure 27. Peaks of the degraded sodium phlogopite at the
maximum pressure of 3860 tons/ft^2

position with the increasing pressure due to elastic response. Perhaps most significant, however, is the co-existence of the peaks at 14.8 Å and 12.2 Å, indicating that two different basal spacings may occur simultaneously in a single crystal of degraded sodium phlogopite under pressure.

The data from the X-ray diffraction study of sodium montmorillonite under pressure are presented in Tables 14 and 15 for loading and unloading paths, respectively. The values tabulated for the basal spacings, line widths and total integrated intensities are the averages of three observations for each run. After maintaining a constant pressure for about 24 hours, the specimen was X-rayed and it was found that the basal spacings, line widths and integrated intensities remained more or less constant with time. The widths of the diffraction peaks B_T at half-height were determined as sketched in Figure 11 for a single peak. For composite peaks the widths of the peaks B_T at half-height were determined as sketched in Figure 12. Resolution of the composite peaks was attempted as previously described for high vacuum X-ray data. The integrated intensities of the peak were determined by use of a planimeter to measure areas of the resolved peaks as before.

Column 1 of Tables 14 and 15 shows the pressure on the sodium montmorillonite sample without correction for apparatus friction. The calculation of the pressure is illustrated in Appendix IV.

The resolved first-order basal spacings are plotted against the uncorrected pressure are shown in Figure 28 for the loading path and Figure 29 for the unloading path. From both figures it is found that the

Table 14.   X-ray diffraction data for high pressure study, loading path

Pressure on sample tsf[a]	Resolved d_{001} spacings Å	Percentage area of the peaks after resolutions, percent	B_o[b] degrees	B_T[c] degrees	A[d] in^2
13.2	20.5	88.0	0.77	0.85	5.7
	23.9	12.0	0.44		
28.2	20.1	82.7	0.74	0.90	6.9
	23.2	17.3	0.50		
39.4	20.1	83.1	0.70	0.95	7.4
	23.1	16.9	0.54		
72.2	19.7	86.0	0.74	0.87	8.2
	22.9	14.0	0.55		
105.1	19.5	88.7	0.73	0.87	12.3
	22.7	11.3	0.64		
137.9	19.3	89.5	0.69	0.87	13.5
	22.2	10.5	0.50		
203.6	16.5	17.3	0.74	1.18	14.4
	19.2	82.7	0.86		
331.6	16.2	34.1	0.58	1.42	16.4
	19.0	65.9	0.86		
492.5	16.1	52.9	0.66	1.49	18.4
	18.6	47.1	0.77		
650.1	16.1	62.7	0.70	1.24	19.1
	18.4	37.3	0.72		
814.5	16.1	100.0	1.15	1.15	21.1
968.6	16.1	100.0	1.06	1.06	26.4
1153.3	16.0	100.0	1.06	1.06	21.8
1293.7	15.9	100.0	1.16	1.16	28.5

[a] 1 tsf = 0.9765 kg/cm^2 = 9765 kg/m^2 = 0.958 bar.

[b] B_o = line widths of individual normal peaks after resolution.

[c] B_T = line width of single peak without resolution.

[d] A = total integrated intensity.

Table 14. (Continued)

Pressure on sample tsf[a]	Resolved d_{001} spacings $\overset{o}{A}$	Percentage area of the peaks after resolutions, percent	B_o[b] degrees	B_T[c] degrees	A[d] in^2
1454.6	13.2	21.2	1.10	1.24	26.8
	15.8	78.8	0.96		
1612.2	13.1	23.7	1.26	1.58	26.9
	15.7	76.7	1.01		
1930.7	13.0	32.3	1.05	1.91	31.9
	15.5	67.7	1.00		
2249.2	12.8	32.7	0.94	2.06	35.5
	15.5	67.3	1.24		
2567.7	12.9	46.2	0.98	2.20	37.8
	15.2	53.8	1.06		
2886.2	12.7	53.7	1.14	2.26	43.1
	15.1	46.3	1.04		
3204.7	12.6	56.7	1.06	2.07	41.4
	15.0	43.3	1.24		

Table 15. X-ray diffraction data for high pressure study, unloading path

Pressure on sample tsf[a]	Resolved d_{001} spacings Å	Percentage area of the peaks after resolutions, percent	B_o[b] degrees	B_T[c] degrees	A[d] In²
3204.7	12.6	56.7	1.06	2.07	41.4
	15.0	43.3	1.24		
2567.7	12.9	54.5	1.00	2.08	49.6
	15.3	45.5	1.12		
1930.7	13.2	44.4	0.99	2.18	88.0
	15.5	55.6	1.04		
1293.7	13.4	29.0	1.22	1.50	105.8
	15.7	71.0	0.94		
968.6	15.8	100.0	1.15	1.15	126.3
650.1	16.0	100.0	0.98	0.98	139.5
331.6	16.2	72.5	0.78	1.15	184.9
	18.9	27.5	0.90		
8.5	20.8	100.0	0.93	0.93	150.6
0	21.7	100.0	0.88	0.88	159.6

[a] 1 tsf = 0.9765 kg/cm² = 9765 kg/m² = 0.958 bar.

[b] B_o = line widths of individual normal peaks after resolution.

[c] B_T = line width of single peak without resolution.
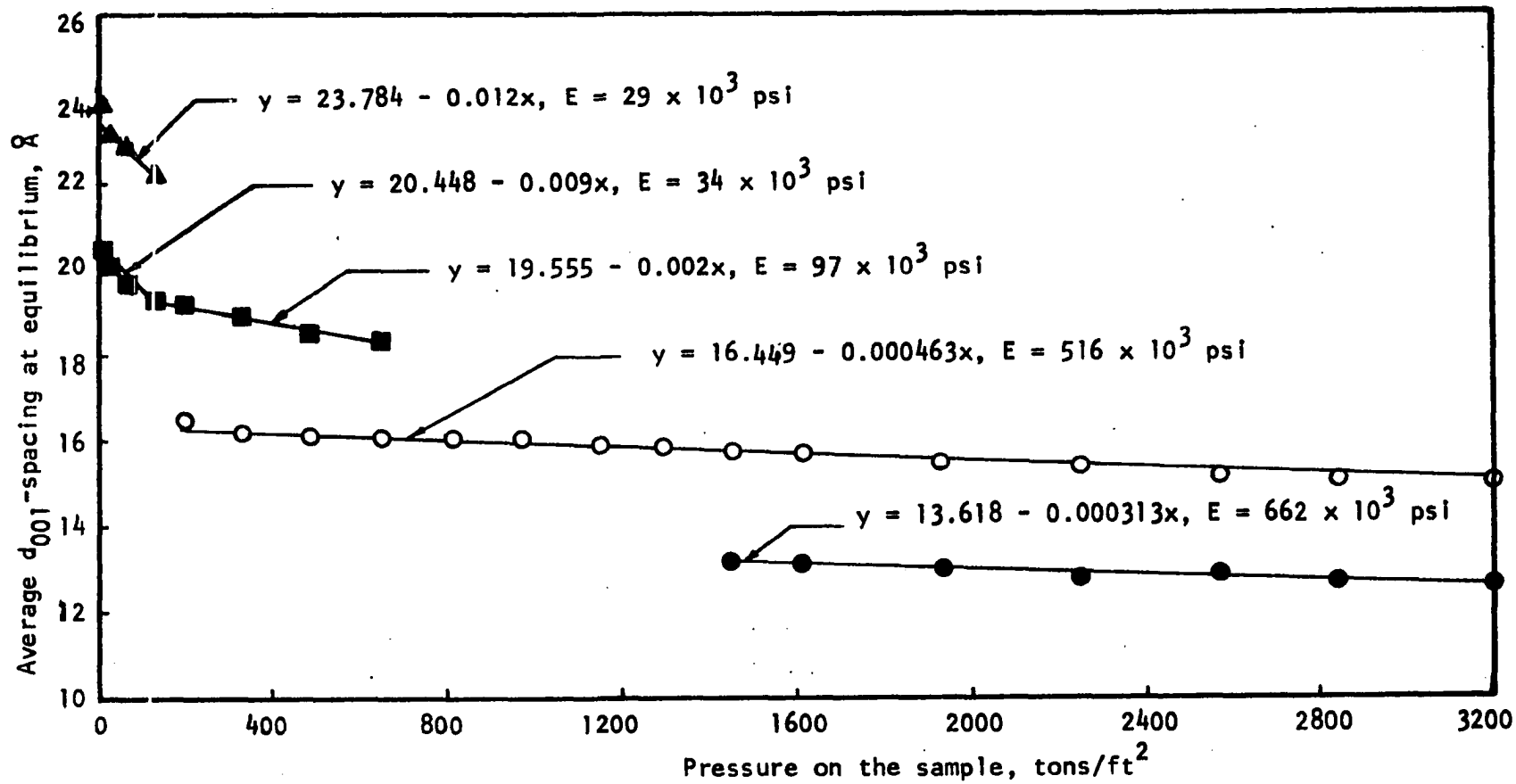
[d] A = total integrated intensity.

Figure 28.   Variation of the d_{001}-spacing with the pressure on the sodium montmorillonite sample, loading path
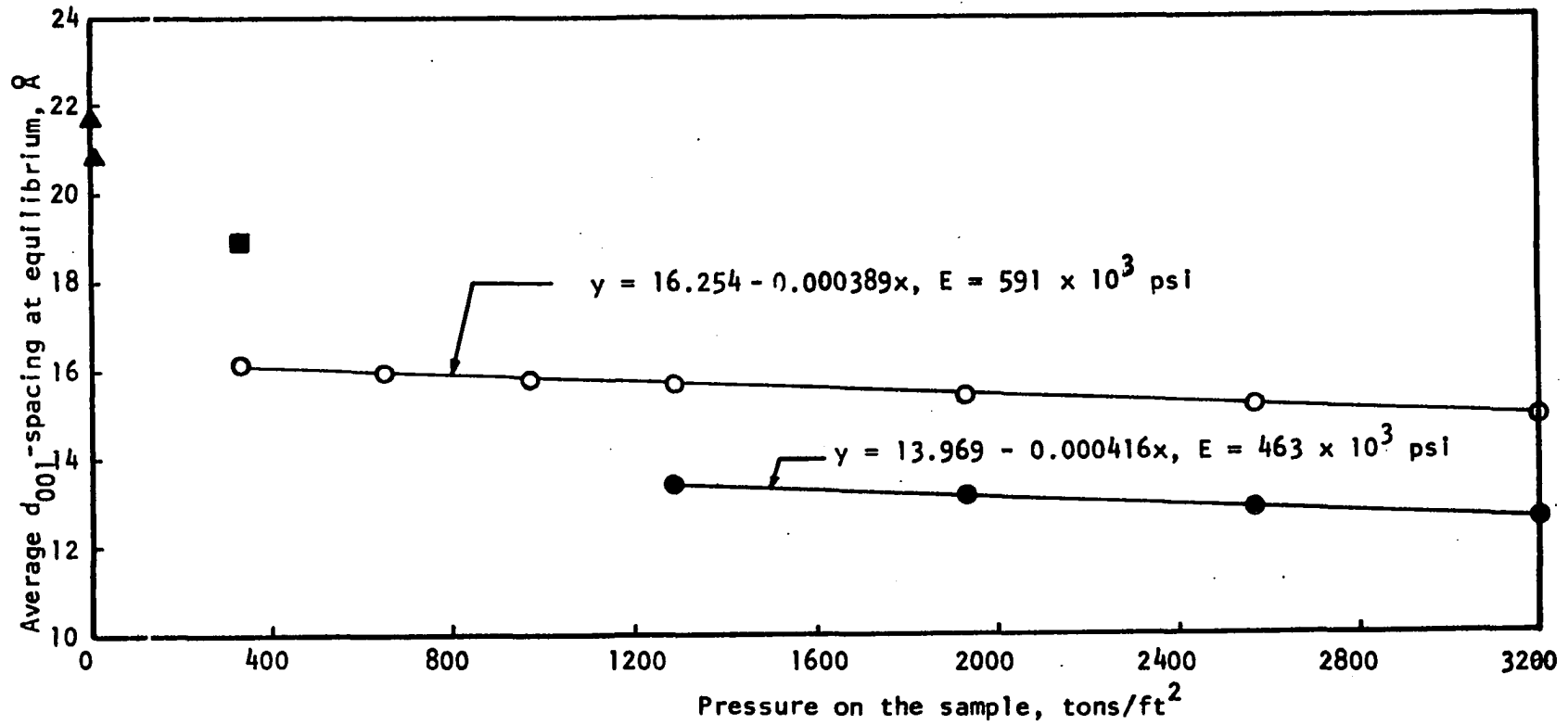
Figure 29. Variation of the d_{001}-spacing with the pressure on the sodium montmorillonite sample, unloading path

relationship between the first order basal spacing and the pressure yields several straight lines with different slopes. The smoothness of those plots tends to substantiate the method of peak resolution, and indicates a maximum error of $\pm$ 0.2 Å in resolved d_{001}-spacing. In Figure 28 (loading path) there are five straight-line portions with progressively decreasing slopes at higher pressures. The first three lines show some scatter and change in slope, perhaps related to the higher water content and less stable structure. The fourth and fifth lines, representing two and one molecular layers of water, respectively, show excellent linearity suggestive of a more rigid elastic structure. Relationships follow the same trend during unloading (Figure 29) as in the loading path, the two bottom-most lines again showing excellent linearity. Only a few points, insufficient to establish linear relationships, were obtained for the higher basal spacings representing the third and fourth layers of inter-layer water. However, the linear relationships between pressures and basal spacings for both loading and unloading paths indicate an elastic property of the sample from which may be obtained moduli of elasticity for each configuration of interlayer water. The linear regression equations for the seven straight-line portions are shown in Figures 28 and 29. If the apparatus friction is constant it will affect the intercepts but not the slopes of the lines, and thus should not influence the moduli of elasticity. The procedure for calculation of the modulus of elasticity is shown in Appendix V.

The modulus of elasticity probably represents a slight rearrangement of water molecules under pressure. This is analogous to the modulus of

elasticity for any solid, and should be unvarying so long as the structure is not significantly changed. However, if the modulus of elasticity involves a change in structure of water molecules, it should change. The closeness of the values for one and two layers of water perhaps correlates with a similarity in swelling pressure increment.

If friction were not constant with pressure, perhaps by increasing as clay squeezes out, during the loading path the friction would increase linearly whereas during unloading it would be constant. This would give higher moduli of elasticity for loading, and the valid values would be from unloading path. However, data indicate no consistent difference. Table 16 shows the variation of modulus of elasticity for various pressure ranges for both loading and unloading conditions.

In order to find the apparatus friction, linear equations for loading. and unloading paths were solved simultaneously to determine the pressure to achieve a specific basal spacing. Thus for $y = 15$ Å (two layers of interlayer water) and $y = 12.6$ Å (one layer of interlayer water):

Loading: $15 = 16.449 - 0.000463x$; $x = 3129.7$ tsf

Unloading: $15 = 16.254 - 0.000389x$; $\underline{x = 3223.7}$ tsf

$$2F^1 = -94.0 \text{ tsf}$$

Loading: $12.6 = 13.618 - 0.000313x$; $x = 3252.4$ tsf

Unloading: $12.6 = 13.969 - 0.000416x$; $\underline{x = 3290.1}$ tsf

$$2F = -38.5 \text{ tsf}$$

The friction is negative from the above calculation. Repeating at $y = 16$ Å and 13.2 Å,

---

[1]See Appendix VI.

Table 16. Moduli of elasticity of various load increments and loading conditions

Number of water layer	Basal spacing (loading or unloading)	Pressure range during loading tsf	$E_{loading}$ psi	Pressure range during un-loading tsf	$E_{unloading}$ psi
4	23.9 to 22.2	0 - 140	29×10^3	--	--
3	20.5 to 19.3	0 - 140	34×10^3	--	--
	19.3 to 18.4	140 - 650	97×10^3	--	--
2	16.2 to 15.0	330 - 3200	516×10^3	330 - 3200	591×10^3
1	13.4 to 12.6	1450 - 3200	662×10^3	1290 - 3200	463×10^3

Loading: $16 = 16.449 - 0.000463x$; $x = 969.8$ tsf

Unloading: $16 = 16.254 - 0.000389x$; $\underline{x = 653.8}$ tsf

$2F = 316.8$ tsf

Loading: $13.2 = 13.618 - 0.000313x$; $x = 1004.8$ tsf

Unloading: $13.2 = 13.969 - 0.000416x$; $\underline{x = 1848.6}$ tsf

$2F = -843.8$ tsf

Thus apparatus friction appears to be negligible compared to other factors affecting the modulus of elasticity.

The effect of preferred orientation due to loading is considered next. Initially, localized contact pressures may be larger than the indicated pressure reading; this effect should decrease with increasing pressure because of better particle reorientation, after which it should remain constant. This also would give a lower modulus of elasticity for the loading path, which again is not consistent with the data. Another possibility is that friction decreases with increasing pressure, due to expansion of the cylinder and injection of oil along the wall (clearance = 0.0004 in). This would give a lower modulus of elasticity for loading, which is consistent for 16 Å spacings but not for 12 Å spacings.

Another possibility is that friction decreases nonlinearly, indicated by a slight shift of data points along the 16 Å line at a pressure of about 1800 tons/ft^2. This suggests that friction decreases above 1800 tons/ft^2, above which the loading and unloading curves are essentially identical on both 16 Å and 12 Å peaks. The latter indicates that friction is negligible at high pressures. It also should be noted that friction must be very low to obtain a response at low applied pressures.

The effect of pressure on the percent of the total integrated intensity assigned to each peak is shown in Figure 30 for loading path and Figure 31 for unloading path. In these figures it can be seen that the whole curve of Figure 30 (loading path) shifts to the left in Figure 31 (unloading path), the pressure required to achieve a given basal spacing being greater for the loading path than for the unloading path. The lateral shift required to superimpose the curves for a single peak first order basal spacing of about 16 $\overset{o}{A}$ in 330 tons/ft^2, and indicates the hysteresis between the loading and the unloading paths for this sodium montmorillonite sample. Hysteresis consists of apparatus friction, difficulty in getting water in and out of clay, and elastic hysteresis. If, as previously indicated, apparatus friction is negligible, the hysteresis effect may be assigned mainly to the difficulty with which water is forced out or reenters between the platelet layers, presumably because of trapping.

The amount of hysteresis increases with the applied pressure and reduction in the number of water layers, as shown in Figure 32, which is obtained from superimposition of Figures 30 and 31. The ordinate axis of the plot of Figure 32 is labelled as pressure retention, and represents the amount of hysteresis in units of pressure, or the difference between swelling pressure and pressure to cause ejection of water, the latter being the larger.

The apparatus had insufficient capacity to attain a single 13 $\overset{o}{A}$ peak indicative of a single layer of water; however, extrapolation of a line through the last 7 points in Figure 30 indicates it would require loading

Figure 30. Variation of the percentage integrated intensity of the peaks after resolution with pressure on the sample of the sodium montmorillonite, loading path
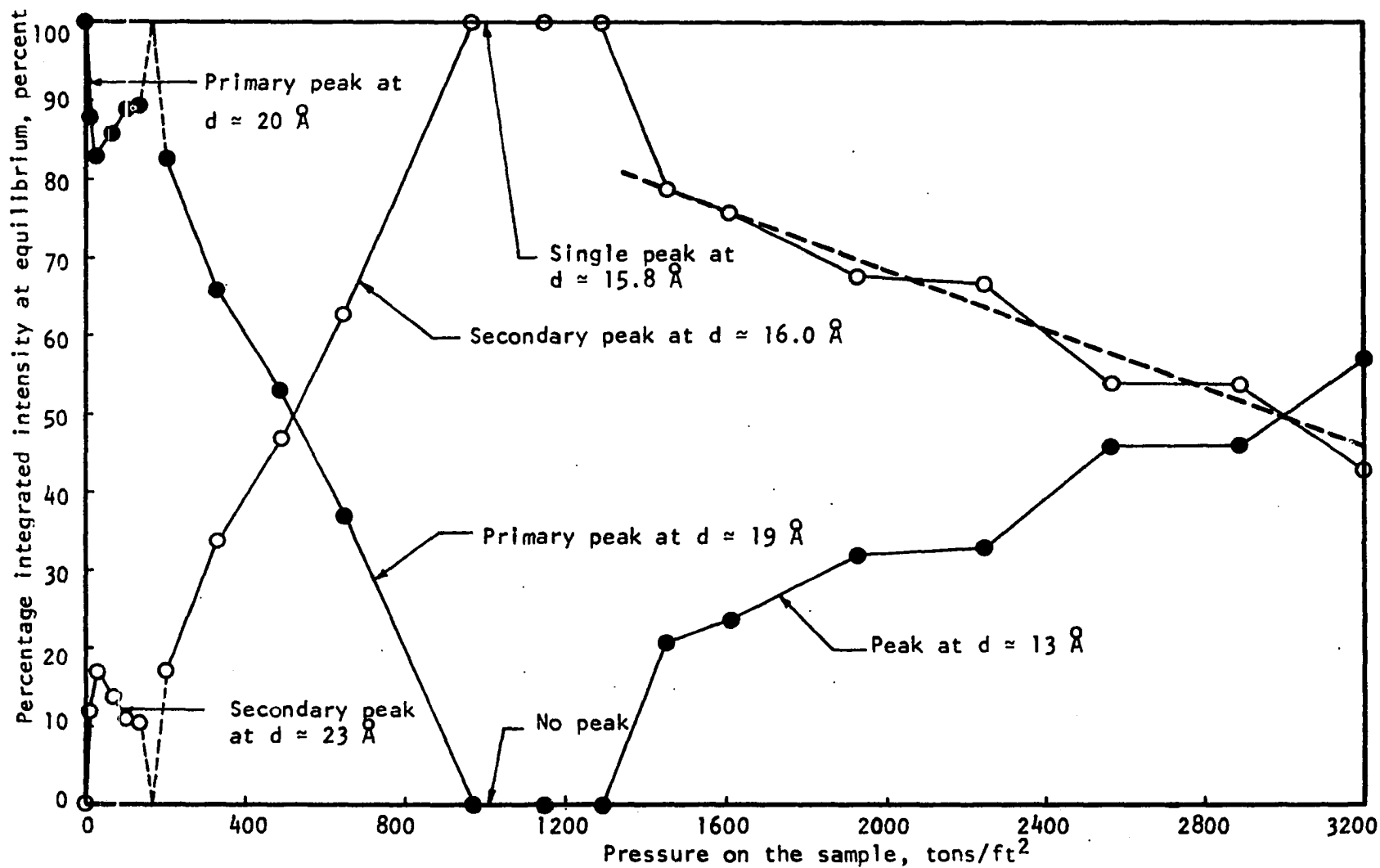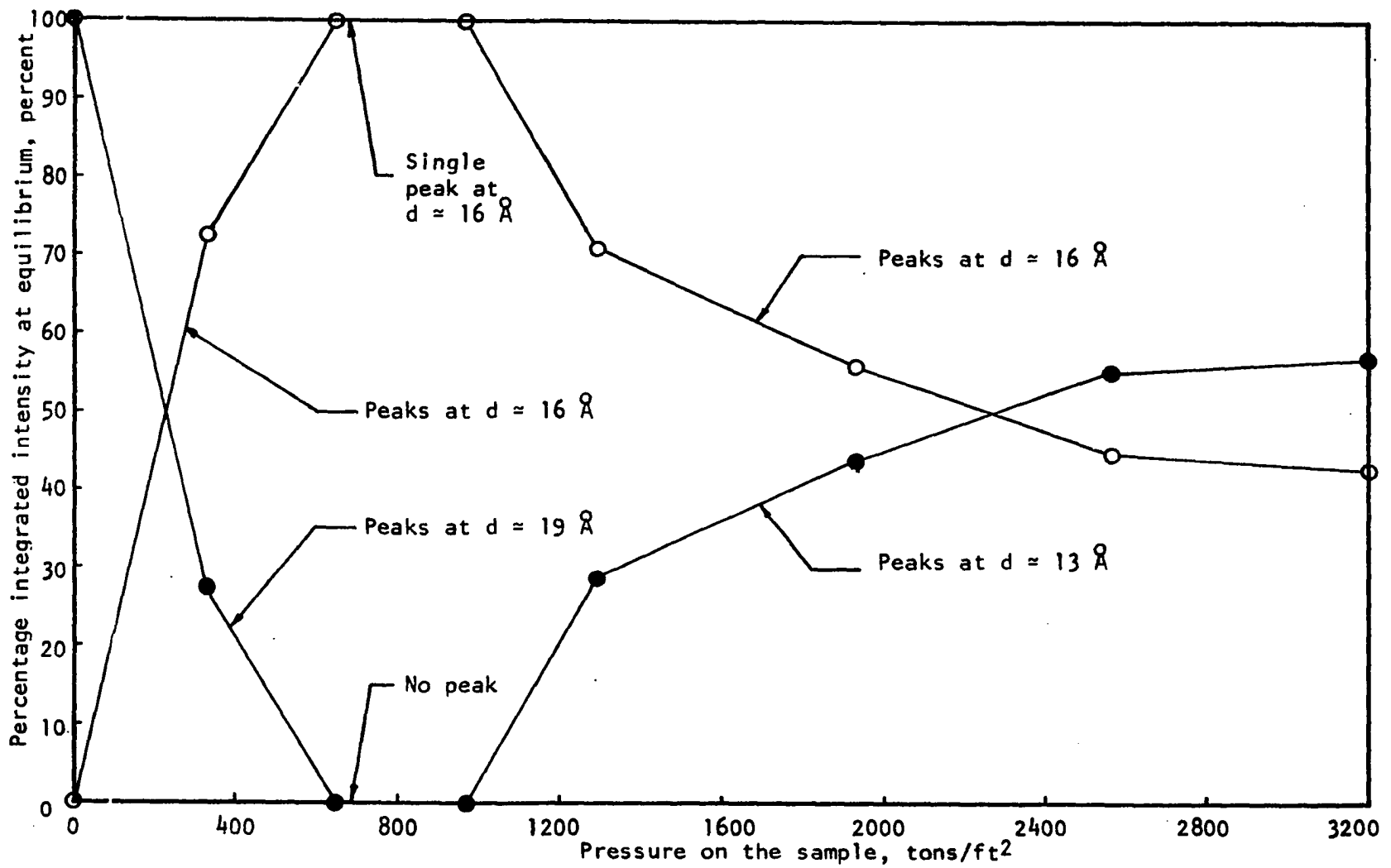
Figure 31. Variation of the percentage integrated intensity of the peaks after resolution with pressure on the sample of the sodium montmorillonite, unloading path
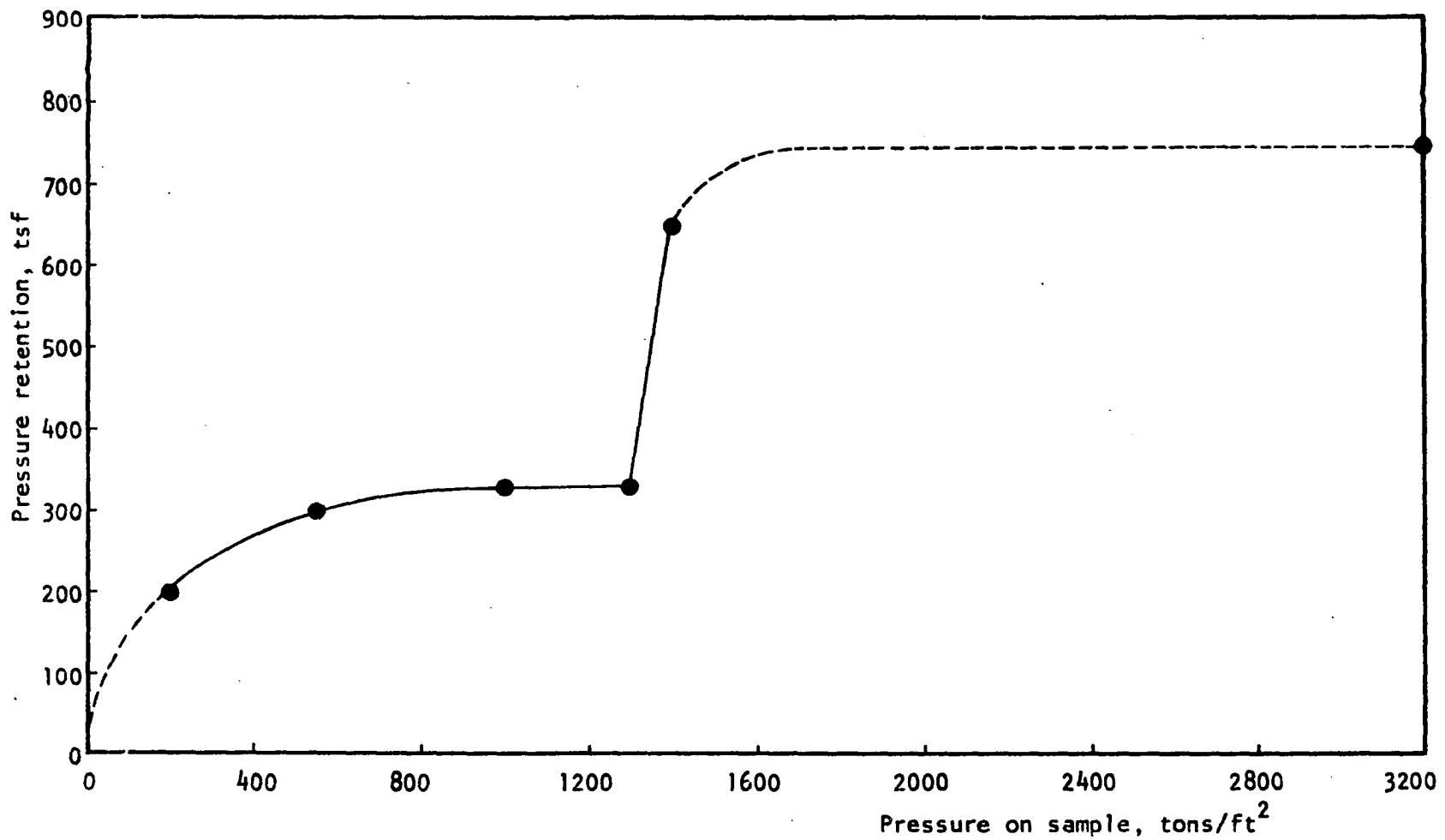
136

Figure 32. Relationship between pressure on the sample and pressure retention of the sodium montmorillonite in the high pressure chamber

of the order of 5,500 tons/ft^2 to bring the basal spacing between the platelets of sodium montmorillonite down to about 13 Å or one layer of interlayer water.

The relationships between total integrated intensity of the composite peak and the applied pressure are shown in Figures 33a, 33b and 33c. Figure 33a presenting the total integrated intensity in units of area under the peak, and Figures 33b and 33c showing the variation in total integrated intensity with pressure in counting units before and after correction for the Lorentz-polarization factor, respectively. The correction data for the Lorentz-polarization factor is tabulated in Tables 17a for the loading path and 17b for the unloading path. The calculation utilizing the Lorentz-polarization factor is illustrated in Appendix II.

From these three Figures it is evident that total integrated intensity increases with pressure during loading, indicating a changing structure factor and/or increased preferred orientation of the particles, the particles tending to adjust themselves into a parallel arrangement normal to the direction of the applied loading. In the unloading path, as shown in the second branch of Figure 33, the integrated intensity increased with decreasing pressure, indicating that preferred orientation was retained during unloading.

The relationships between total intensity and pressure during cyclical loading and unloading are shown in Figures 34a and 34b. Loading past the second cycle caused little change in total intensity but reduced hysteresis in the response of basal spacings to pressure.

Figure 33a. Variation of the total area under the peak with the pressure on the sample of sodium montmorillonite before correction for the Lorentz-polarization factor

Figure 33b. Variation of the total integrated intensity of the peaks with the pressure on the sample of sodium montmorillonite before correction for the Lorentz-polarization factor
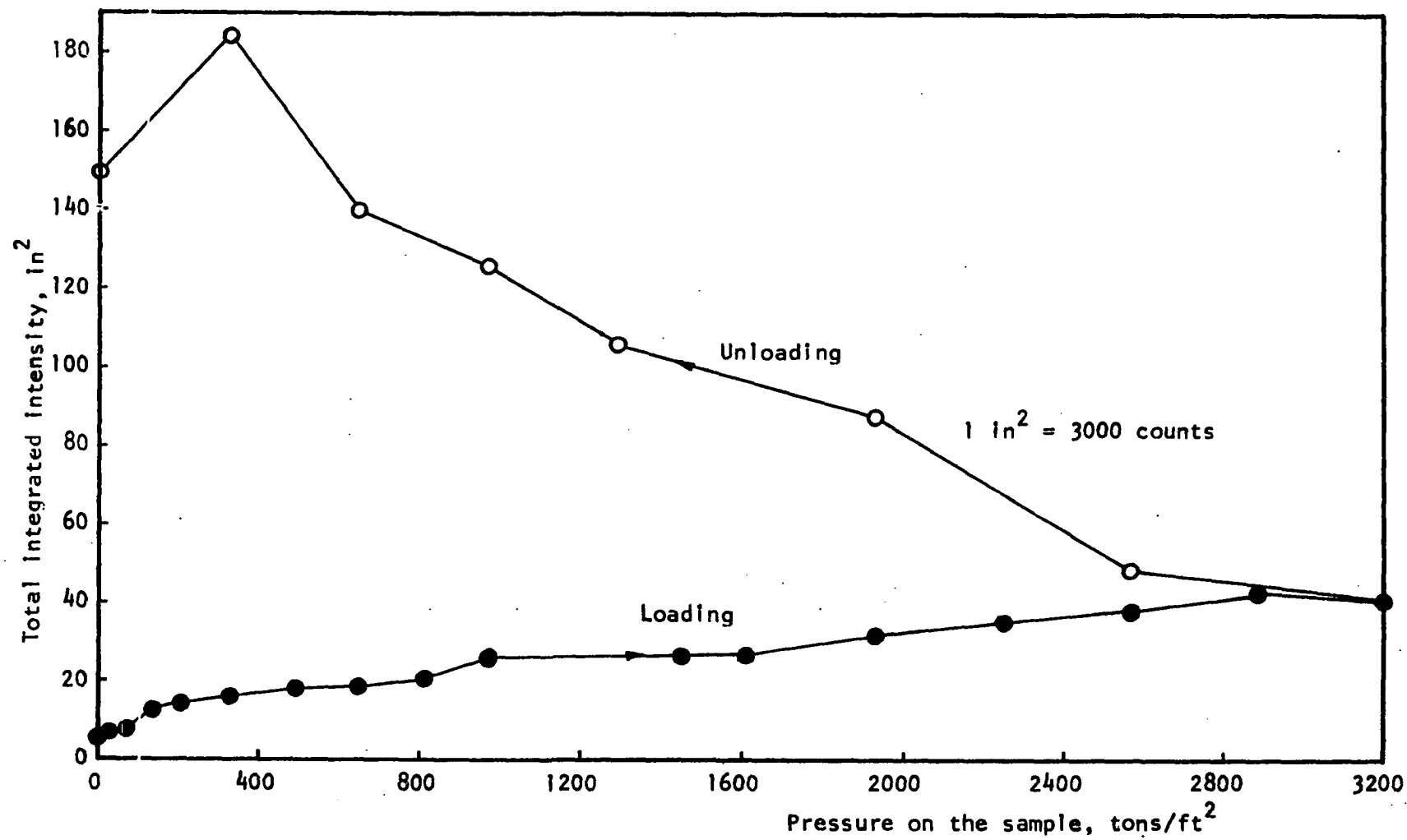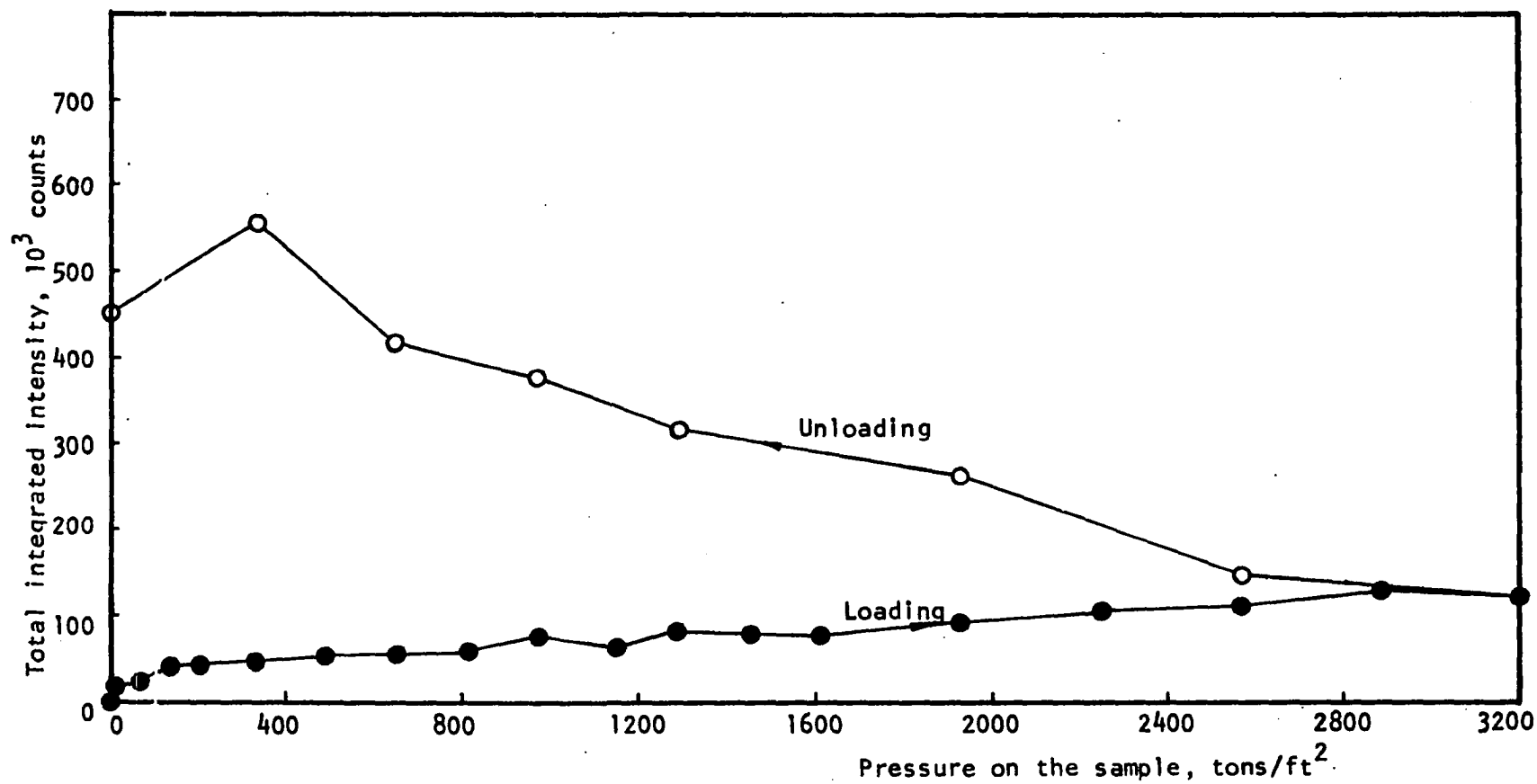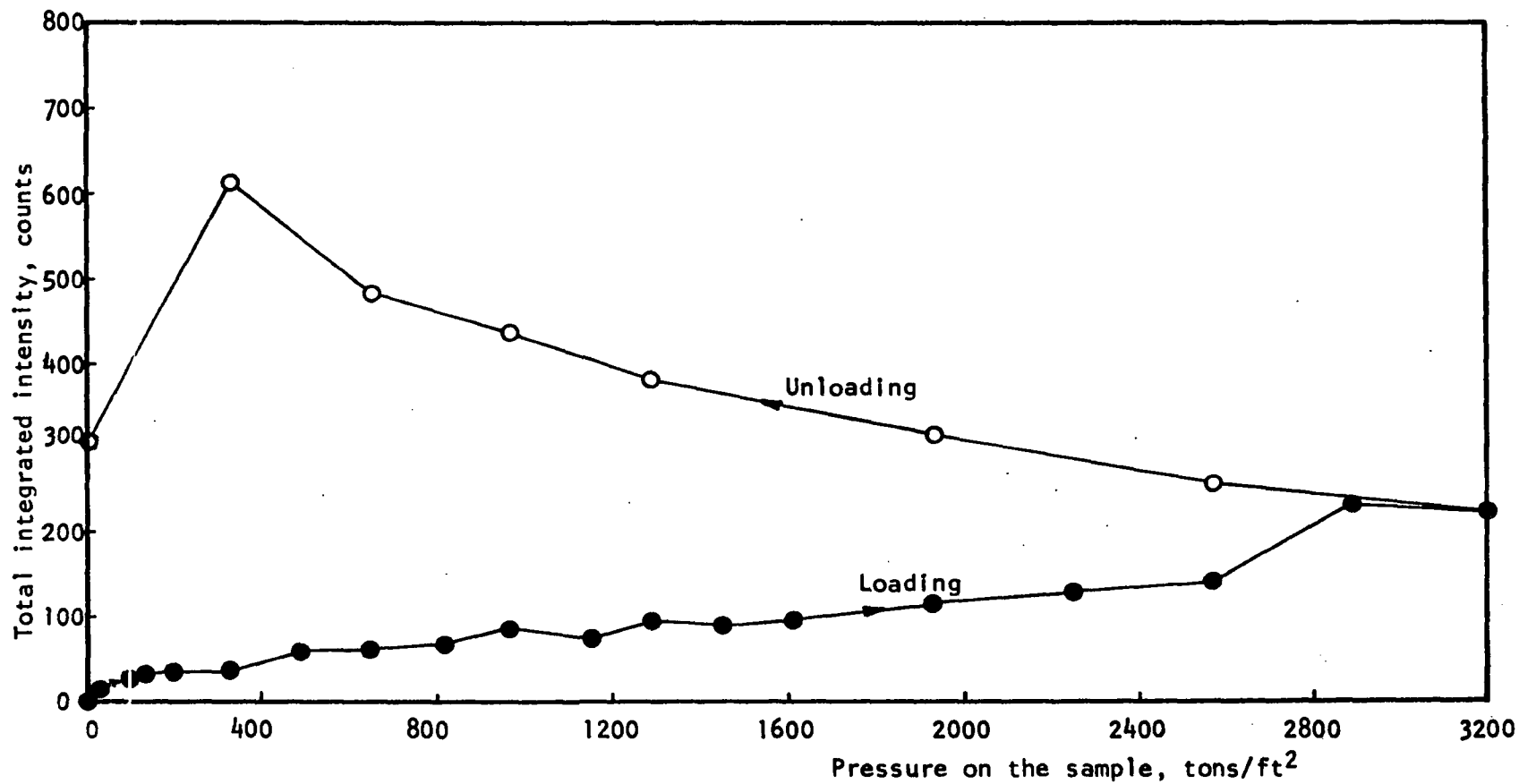
Figure 33c. Variation of the total integrated intensity of the peaks with the pressure on the sample of sodium montmorillonite after correction for the Lorentz-polarization factor

Table 17a. Total integrated intensity corrected for the Lorentz-polarization factor[a], loading path

Pressure on sample tsf	d_{001} Å	$\sin\theta$ [b]	LP[c]	I_{total}		$I_{total}/(LP)$		$\dfrac{I_{total}}{(LP)\,(d_{001})}$
				in^2	10^3 counts	in^2	counts	
13.2	20.5	0.037	1458	5.7	17.1	0.0039	11.7	0.57
28.2	20.1	0.0038	1382	6.9	20.7	0.0049	14.7	0.73
39.4	20.1	0.038	1382	7.4	22.2	0.0053	15.9	0.79
72.2	19.7	0.039	1312	8.2	24.6	0.0062	18.6	0.94
105.1	19.5	0.039	1312	12.3	36.9	0.0093	27.9	1.43
137.9	19.3	0.039	1312	13.5	40.5	0.0102	30.6	1.58
203.6	19.2	0.040	1247	14.4	43.2	0.0115	34.5	1.79
331.6	19.0	0.040	1247	16.4	49.2	0.0131	39.3	2.06
492.5	16.1	0.047	902.4	18.4	55.2	0.0203	60.9	3.78

[a]See Appendix II.

[b]$\sin\theta = \lambda/2d = 1.54/2d = 0.77/d$.

[c]LP = Lorentz-polarization factor.

Pressure on sample tsf	d_{001} Å	$\sin \theta^b$	LP^c	I_{total} in^2	I_{total} 10^3 counts	$I_{total}/(LP)$ in^2	$I_{total}/(LP)$ counts	$\dfrac{I_{total}}{(LP)(d_{001})}$
650.1	16.1	0.047	902.4	19.1	57.3	0.0211	63.3	3.93
814.5	16.1	0.047	902.4	21.1	63.3	0.0233	69.9	4.34
968.6	16.1	0.047	902.4	26.4	79.2	0.0292	87.6	5.44
1153.3	16.0	0.048	865.1	21.8	65.4	0.0251	75.3	4.70
1293.7	15.9	0.048	865.1	28.5	85.5	0.0329	98.7	6.20
1454.6	15.8	0.048	865.1	26.8	80.4	0.0309	92.7	5.86
1612.2	15.7	0.049	830.0	26.9	80.7	0.0324	97.2	6.19
1930.7	15.5	0.049	830.0	31.9	95.7	0.0384	115.2	7.43
2249.2	15.5	0.049	830.0	35.5	106.5	0.0427	128.1	8.26
2567.7	15.2	0.050	797.0	37.8	113.4	0.0474	142.2	9.35
2886.2	12.7	0.060	552.6	43.1	129.3	0.0779	233.7	18.40
3204.7	12.6	0.060	552.6	41.4	124.2	0.0749	224.7	17.83

143

Table 17b. Total integrated intensity corrected for the Lorentz-polarization factor[a], unloading path

Pressure on sample tsf	d_{001} Å	$\sin \theta^b$	LP^c	I_{total} in^2	I_{total} 10^3 counts	$(I_{total})/(LP)$ in^2	$(I_{total})/(LP)$ counts	$\dfrac{I_{total}}{(LP)(d_{001})}$
3204.7	12.6	0.061	534.5	41.5	124.2	0.0774	224.7	17.83
2567.7	12.9	0.059	571.6	49.6	148.8	0.0867	260.1	20.16
1930.7	15.5	0.049	830.0	88.0	264.0	0.1060	318.0	20.51
1293.7	15.7	0.049	830.0	105.8	317.4	0.1274	382.2	24.34
968.6	15.8	0.048	865.1	126.3	378.9	0.1459	437.7	27.70
650.1	16.0	0.048	865.1	139.5	418.5	0.1612	483.6	30.22
331.6	16.2	0.047	902.4	184.9	554.7	0.2046	613.8	37.88
8.5	20.8	0.037	1458.0	150.6	451.8	0.1032	309.6	14.88
0	21.7	0.035	1630.0	159.6	478.8	0.0979	293.7	13.53

[a] See Appendix II.

[b] $\sin \theta = \lambda/2d = 1.54/2d = 0.77/d$.

[c] LP = Lorentz-polarization factor.

144

Figure 34a. Variation of total intensity (B_T x H) with the pressure on the sodium montmorillonite sample for the cyclic loading, loading path

Legend:
- ●————● First cycle
- ○————○ Second cycle
- ▲————▲ Third cycle
- ■————■ Fourth cycle

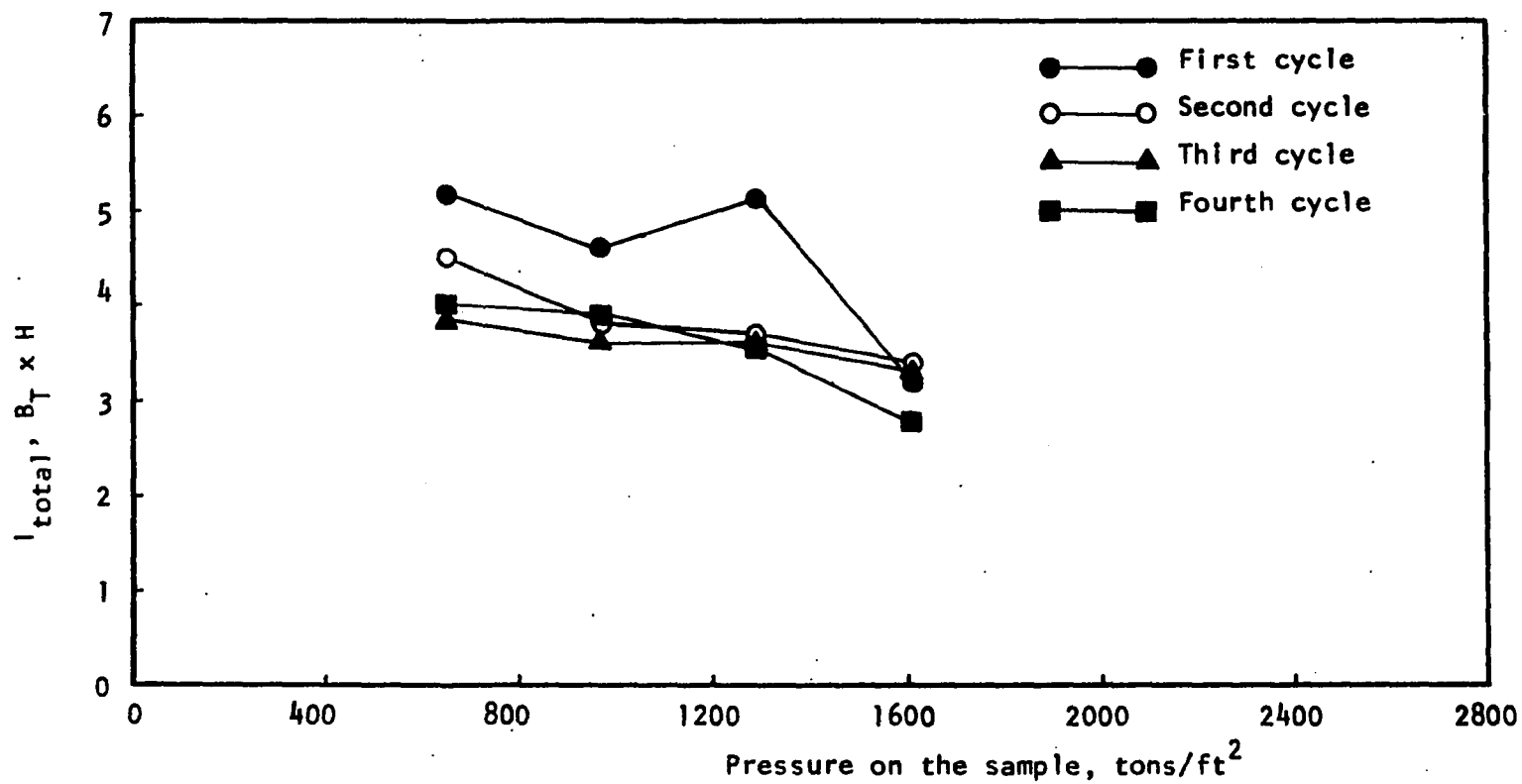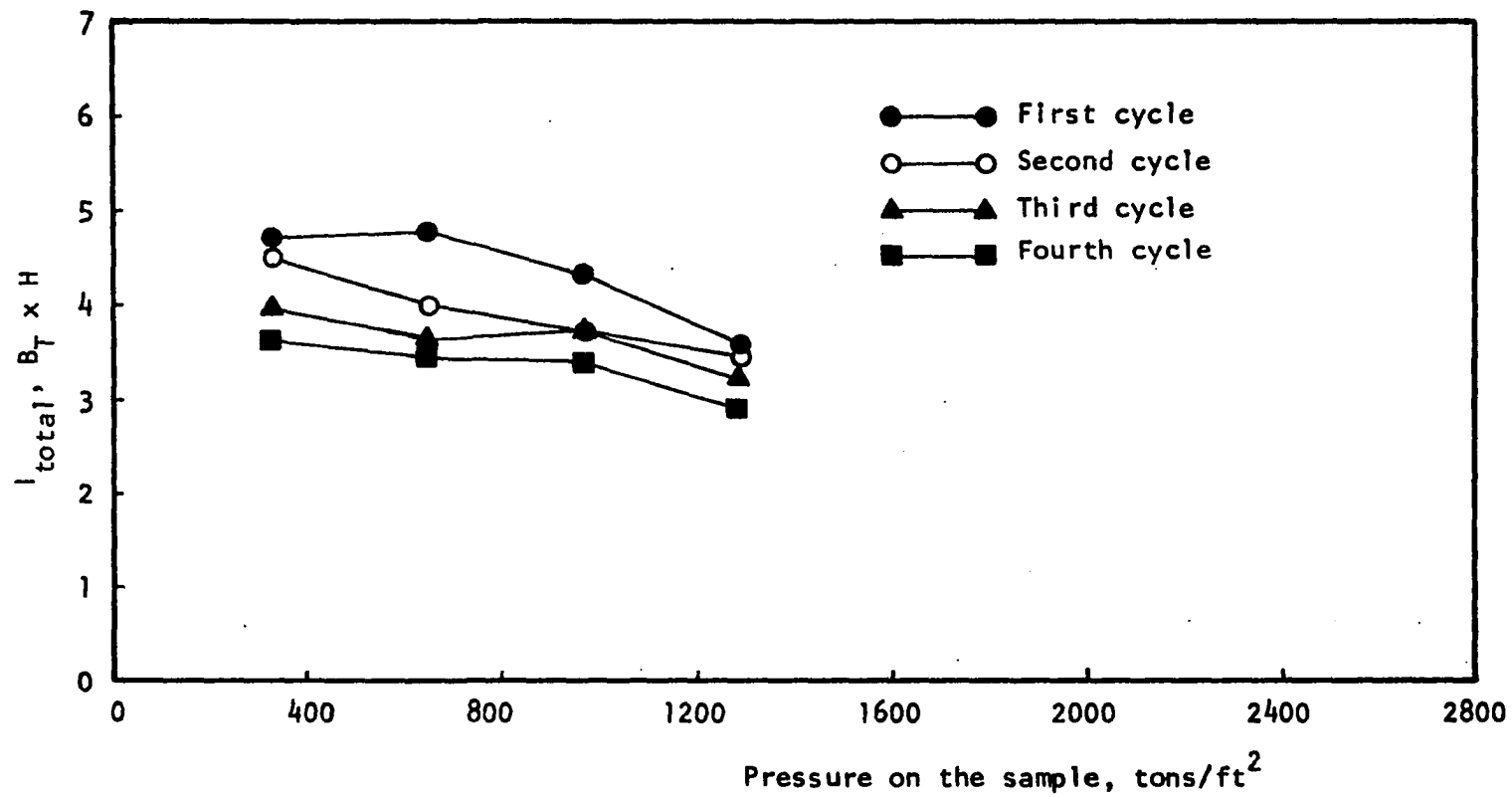Y-axis: I_{total}, B_T x H

X-axis: Pressure on the sample, tons/ft^2

Figure 34b. Variation of total intensity (B_T x H) with the pressure on the sodium montmorillonite sample for the cyclic loading, unloading path

Table 18 presents the swelling and consolidation pressures obtained from high pressure data compared with those from high-vacuum data. The Table also tabulates swelling pressure and consolidation pressures obtained from other investigators (98,107,109). It is clear that the consolidation pressures obtained from the high-vacuum data and the high pressure data are in the same range for the first and third states of hydration. Discrepancies may be due to nonuniform effective stress between the platelets in the high pressure study and the difficulty of squeezing water out of the platelets of the sodium montmorillonite. The swelling pressures from high-vacuum data in the present study fall in the same range as those obtained by Roderick and Demirel (98). However, the swelling pressures from high pressure data are many times greater than that from high-vacuum data. This is perhaps due to greater trapping of water between the platelets of sodium montmorillonite under a condition of uniaxial pressure and preferred orientation, compared to the relatively loose and random structure during adsorption-desorption experiments.

The high-vacuum data used in the present study are from adsorption runs, which give lower values of swelling pressure. If the desorption data were used and the graphical method of consolidation pressure determination employed, higher values of consolidation pressure would be obtained. However, these values would still be less than those obtained by the method of van Olphen because of the assumed series stepwise energy level in his calculation.

Table 18. Swelling pressures from high pressure data comparing to that from high-vacuum data

Hydration state	Swelling pressure, tons/ft^2			Consolidation pressure tons/ft^2	
	Adsorption data		High pressure data[b]	Desorption data[c]	High pressure data[d]
	Present study	Roderick and Demirel[a]		van Olphen	
I	282	313	4750	4800	5500
II	179	190	> 2450	1300	> 3200
III	63	47	340	380	650

[a]Based on high vacuum data, adsorption run (98).

[b]Obtained by subtracting pressure retention in Figure 32 from consolidation pressure, high pressure data.

[c]Extrapolated from high vacuum data, desorption run (107,109).

[d]Extrapolated from Figure 30 of the present study.

CONCLUSIONS

The following conclusions have been drawn on the basis of the results obtained:

1. The high pressure and high-vacuum accessories used in the present study, designed and assembled by Olson (89) functioned perfectly.

2. The change in average basal spacings of sodium montmorillonite takes place in a continuous but nonuniform manner with changes in relative pressure. Continuity is due to simultaneous existence of varying numbers of layers of interlayer water. Expansion tends to occur in three increments. These results are consistent with those of past investigations.

3. In the high pressure study of a single crystal of a sodium-tetraphenyl boron-degraded phlogopite, the X-ray spectra show separate peaks indicative of the co-existence of one and two layers of interlayer water between the plates.

4. In the high pressure study of a sodium montomorillonite, the X-ray spectra show overlapping peaks, indicating the co-existence of varying numbers of layers of interlayer water between the plates.

5. A method for resolving composite peaks was introduced and is found to be workable for both high-vacuum and high pressure studies.

6. Single peaks were found in a narrow range of relative pressures from 0.85 to 0.96, indicating all platelets have the same basal spacing. Outside this range the peaks are composite, indicating interstratification of the system.

7. The combined free energy data of Roderick (97) and the X-ray data of the present study indicates a possible laminar configuration of the interlayer water. Because of the questionable nature of the fit, each increment of adsorption at about one layer of interlayer water is called a hydration state.

8. The water-vapor adsorption surface area calculations of past investigators (44,55,91) assumed monolayer adsorption on internal surfaces, whereas X-ray data indicate only one molecular layer of interlayer water between successive platelets of sodium montmorillonite, or one-half layer for each surface. The surface area reported by those investigators thus is only about one-half of the actual surface area. Corrected determinations agre. closely with surface area calculations from crystallographic data.

9. The free energy change during the first state of hydration is approximately the same as that for the second state of hydration; the change during the third state is substantially less than those for the other two. Also pertaining to the same conclusions is the expansion energy for the various states.

10. Free energy data and X-ray data permit the estimation of swelling pressures exerted by sodium montmorillonite due to the uptake of interlayer water when the material is in contact with saturated vapor. The calculated swelling pressure exerted when the platelet separation is zero is about 282 tons/ft^2. The pressure exerted when the second state of hydration is beginning is about 179 tons/ft^2; and when the third state is beginning is about 63 tons/ft^2.

11. The swelling pressure calculated by the method of van Olphen using the data of Roderick (97) are many times greater than the values obtained from the free energy and X-ray data of the present study.

12. The high pressure apparatus has insufficient capacity to squeeze out all layers of the water from the sodium montmorillonite. The pressure to squeeze the last layer of water is obtained from extrapolation to be 5500 tons/ft^2.

13. The linearity of the pressure-basal spacing plot indicates the elastic nature of the sodium montmorillonite - water system, and also substantiates the method of peak resolution. The modulus of elasticity of sodium montmorillonite - water system is found to be variable with the pressure and number of water layers between the platelets.

14. The inequality of the consolidation and swelling pressures are probably due to the hysteresis of a highly oriented clay-water system under uniaxially applied pressure, i.e. difficulty in water squeezing out or re-entering between the platelets of sodium montmorillonite.

15. The total integrated intensity of diffraction increased with pressure for the loading path. For the unloading path the total integrated intensity is still increasing. This indicates the increased structure factor and/or preferred orientation for both paths.

16. In the cyclical loading, loading past the second cycle caused little change in total X-ray intensity but reduced hysteresis in the response of basal spacings to pressure.

17. Swelling pressures obtained from the high pressure study are 4750, more than 2450, and 340 tons/ft^2 for the first, second and third

states of hydration. These are close to those calculated by van Olphen (107, 109), but considerably higher than those calculated from the ad-sorption data.

18. The difference between the swelling pressures from high-vacuum and high pressure studies is presumably due to the different stress states influencing structure and preferred orientation and hence the difficulty with which water could be pulled or squeezed out, or could re-enter between the oriented flexible platelets of sodium montmorillonite. Another factor may be the nonuniform effective stress between the platelets.

BIBLIOGRAPHY

1. Adamson, A. W. Physical chemistry of surfaces. 2nd. ed. New York, Interscience Publishers. 1967.

2. Anderson, D. M. and Low, P. F. The density of adsorbed water by lithium, sodium, and potassium bentonite. Soil Science Society of America Proceedings 22: 99-103. 1958.

3. Aylmore, L. A. G. and Quirk, J. P. The structural status of clay systems. National Conference on Clays and Clay Minerals Proceedings 9: 104-130. 1960.

4. Aylmore, L. A. G. and Quirk, J. P. Swelling of clay water systems. Nature (London) 183: 1752-1753. 1959.

5. Bangham, D. H. The Gibbs adsorption equation and adsorption on solids. Faraday Society Transactions 33: 805-811. 1937.

6. Bangham, D. H. and Razouk, R. I. Adsorption and wettability of solid surfaces. Faraday Society Transactions 33: 1459-1463. 1937.

7. Barrer, R. M. and MacLeod, D. M. Intercalation and sorption by montmorillonite. Faraday Society Transactions 50: 980-989. 1954.

8. Barshad, I. Adsorption and swelling properties of clay-water system. State of California Department of Natural Resources, Division of Mines Bulletin 169: 70-77. 1955.

9. Barshad, I. The nature of lattice expansion and its relation to hydration in montmorillonite and vermiculite. American Mineralogist 34: 675-684. 1949.

10. Bartell, F. E. and Bower, J. E. Adsorption of vapors by silica gels of different structures. Journal of Colloid Science 7: 80-93. 1952.

11. Bartell, F. E. and Dobay, D. G. The adsorption aliphatic amine vapors by silica gel. American Chemical Society Journal 72: 4388-4393. 1950.

12. Baver, L. D. and Winterkorn, H. W. Sorption of liquids by soil colloids, II, surface behavior in the hydration of clays. Soil Science 40: 403-418. 1936.

13. Bering, B. P., Dreving, V. P., Kiselev, A. V., Serpinsky, V. V., Surova, M. D. and Shcherbakova, K. D. Adsorption properties of montmorillonite clays. Colloidal Journal (USSR) 14: 433-441. 1952.

14. Bernal, J. D. and Fowler, A. H. A theory of water and ionic solution with particular reference to hydroxyl ions. Journal of Chemical Physics 1: 515-548. 1933.

15. Boyd, G. E. and Livingston, H. K. Adsorption and energy changes at crystalline solid surfaces. American Chemical Society Journal 64: 2383-2388. 1942.

16. Bradley, W. F. Analysis of mixed-layer clay mineral structures. Analytical Chemistry 25: 727-730. 1953.

17. Bradley, W. F., Grim, R. E. and Clark, G. L. A study of the behavior of montmorillonite upon wetting. Zeitschrift für Krstallographie 97: 216-222. 1937.

18. Brindley, G. W. Experimental methods. In Brown, G., editor. The X-ray identification and crystal structure of clay minerals. pp. 1-50. London, Mineralogical Society. 1961.

19. Brindley, G. W. Identification of clay minerals by X-ray diffraction analysis. State of California Department of Natural Resources, Division of Mines Bulletin 169: 119-129. 1955.

20. Brindley, G. W. Quantitative analysis of clay mixtures. In Brown, G., editor. The X-ray identification and crystal structure of clay minerals. pp. 489-516. London, Mineralogical Society. 1961.

21. Brindley, G. W. X-ray diffraction by layer lattices with random layer displacements. In Brown, G., editor. The X-ray identification and crystal structures of clay minerals. pp. 446-466. London, Mineralogical Society. 1961.

22. Brunauer, S. The adsorption of gases and vapors. Physical adsorption. Princeton, N.J., Princeton University Press. 1943.

23. Brunauer, S. Solid surfaces and solid-gas interface. Advances in Chemistry Series 33: 5-17. 1961.

24. Brunauer, S., Deming, L. S., Deming, W. E. and Teller, E. On a theory of the van der Waals adsorption of gases. American Chemical Society Journal 62: 1723-1732. 1940.

25. Brunauer, S., Emmett, P. H. and Teller, E. Adsorption of gases in multimolecular layers. American Chemical Society Journal 60: 309-319. 1938.

26. Buessem, W. R. and Nagy, Bartholomew. The mechanism of the deformation of clay. National Academy of Science. National Research Council Publication 327: 480-491. 1953.

27. Clampitt, B. H. and German, D. E. Heat of vaporization of molecules at liquid-vapor interfaces. Journal of Physical Chemistry 62: 438-440. 1958.

28. Clark, L. J. Hydration characteristics of K-depleted mica. Unpublished Ph.D. thesis. Ames, Iowa, Library, Iowa State University of Science and Technology. 1969.

29. Cornet, I. Expansion of the montmorillonite lattice on hydration. Journal of Chemical Physics 18: 623-626. 1950.

30. Craig, R. G., Van Voohis, J. J. and Bartell, F. E. Free energy of immersion of compressed powders with different liquids. I. Graphite powders. Journal of Physical Chemistry 6: 1225-1230. 1956.

31. Deeds, C. T. and van Olphen, H. Density studies in clay-liquid systems. I. The density of water adsorbed by expanding clays. Advances in Chemistry Series 33: 332-339.

32. Deitz, V. R. Gas adsorption, the extreme limits of surface coverage. Industrial and Engineering Chemistry 57, No. 5: 49-66. 1965.

33. Demirel, T. Adsorption of water vapor by sodium and calcium montmorillonites. Unpublished Ph.D. thesis. Ames, Iowa, Library, Iowa State University of Science and Technology. 1962.

34. Dobay, D. G., Fu, Y. and Bartell, F. E. Energetics of the adsorption of aliphatic amines by silica gel. American Chemical Society Journal 73: 308-314. 1951.

35. Eisenberg, D. and Kauzmann, W. The structure and properties of water. New York, Oxford University Press. 1969.

36. Emmett, P. H., Brunauer, S. and Love, K. S. The measurement of surface area of soils and soil colloids by the use of low temperature van der Waals adsorption isotherms. Soil Science 45: 57-65. 1938.

37. Forslind, E. Crystal structure and water adsorption of clay minerals. Swedish Cement and Concrete Research Institute Bulletin 11: 1-20. 1948.

38. Forslind, E. Some remarks on the interaction between the exchangeable ions and the adsorbed water layers in montmorillonite. 4th International Congress of Soil Science Transactions 1: 110-113. 1950.

39. Foster, A. G. The sorption of condensible vapors by porous solids. I. The applicability of the capillary theory. Faraday Society Transactions 28: 645-657. 1932.

40. Foster, Margaret D. The relation between composition and swelling in clays. National Academy of Science - National Research Council Publication 395: 205-220. 1954.

41. Frank, Henry S. The structure of ordinary water. Science 169: 635-641. 1970.

42. Fu, Y. and Bartell, F. E. Surface area of porous adsorbents. Journal of Physical and Colloid Chemistry 55: 662-675. 1951.

43. Gillery, F. H. Adsorption-desorption characteristics of synthetic montmorillonoids in humid atmospheres. American Mineralogist 44: 806-818. 1959.

44. Goates, J. R. and Hatch, C. V. Standard adsorption potentials of water vapor on soil colloids. Soil Science 75: 275-278. 1953.

45. Grim, R. E. Applied clay mineralogy. New York, McGraw-Hill Book Company, Inc. 1962.

46. Grim, R. E. Clay mineralogy. 2nd ed. New York, McGraw-Hill Book Company, Inc. 1968.

47. Grim, R. E. Some fundamental factors influencing the properties of soil materials. Second International Conference on Soil Mechanics and Foundation Engineering Proceedings 3: 8-12. 1948.

48. Hemwall, John B. and Low, Philip F. The hydrostatic repulsive force in clay swelling. Soil Science 84: 135-145. 1956.

49. Hendricks, S. B. and Jefferson, M. E. Structure of kaolin and talc-pyrophyllite hydrates and their bearing on water sorption of clays. American Mineralogist 23: 863-875. 1938.

50. Hendricks, S. B., Nelson, R. A. and Alexander, L. T. Hydration mechanisms of the clay mineral montmorillonite saturated with various cations. American Chemical Society Journal 62: 1457-1464. 1940.

51. Hirst, C. D. The mechanical interaction between mobile insoluble adsorbed films, capillary condensed liquid and fine-structured solids. Faraday Society Discussions 3: 22-28. 1948.

52. Hodgman, C. D., Weast, R. C., Shankland, R. S. and Selby, S. M., editors. Handbook of Chemistry and Physics. 44th ed. Cleveland, Ohio. The Chemical Rubber Publishing Co. 1963.

53. Inness, W. B. and Rowley, H. H. Relationship between the adsorption isotherm and the spreading forces. Journal of Physical Chemistry 45: 158-165. 1941.

54. International Union of Crystallography. International tables for X-ray crystallography. Vol. 2. Birmingham, England. The Kynoch Press. 1959.

55. Johansen, R. T. and Dunning, H. N. Water-vapor adsorption on clays. National Conference on Clays and Clay Minerals, Proceedings 6: 249-258. 1959.

56. Johns, W. D., Grim, R. E. and Bradley, W. F. Quantitative estimation of clay minerals by diffraction methods. Journal of Sedimentary Petrology 24: 242-251. 1954.

57. Jonas, E. C. and Robertson, H. E. Particle size as a factor influencing expansion of the three-layer clay minerals. American Mineralogist 45: 828-838. 1960.

58. Jura, G. and Harkins, W. E. Determination of free surface energy of a solid by an adsorbed film. American Chemical Society Journal 66: 1356-1362. 1944.

59. Katz, J. R. The laws of swelling. Faraday Society Transactions 29: 279-300. 1933.

60. Klug, H. P. and Alexander, L. E. X-ray diffraction procedures for polycrystalline and amorphous materials. New York, John Wiley and Sons, Inc. 1954.

61. Lambe, T. W. and Whitman, R. V. Soil mechanics. New York, John Wiley and Sons, Inc. 1969.

62. Langmuir, I. The adsorption of gases on plane surfaces of glass, mica, and platinum. American Chemical Society Journal 40: 1361-1403. 1918.

63. Livingston, H. K. The cross-sectional areas of molecules adsorbed on solid surfaces. Journal of Colloid Science 4: 447-457. 1949.

64. Low, P. F. Physical chemistry of clay-water interaction. Advances in Agronomy 13: 269-327. 1961.

65. MacEwan, D. M. C. Interlamella sorption by clay minerals. State of California Department of Natural Resources, Division of Mines Bulletin 169: 78-85. 1955.

66. MacEwan, D. M. C. Montmorillonite minerals. In Brown, G., ed. The X-ray identification and crystal structures of clay minerals. pp. 143-207. London, Mineralogical Society. 1961.

67. MacEwan, D. M. C., Amil, A. R. and Brown, G. Interstratified clay
    minerals. In Brown, G., ed. The X-ray identification and crystal
    structures of clay minerals. pp. 393-445. London, Mineralogical
    Society. 1961.

68. Macey, H. H. Clay-water relationships and the internal mechanism of
    drying. Ceramic Society Transactions 41: 73-121. 1942.

69. Mackenzie, R. C. Some notes on the hydration of montmorillonite.
    Mineralogical Society of Great Britain. Clay Mineral Bulletin 4:
    115-120. 1950.

70. McBain, J. W. An explanation of hysteresis in the hydration and
    dehydration of gels. American Chemical Society Journal 48: 690-
    695. 1926.

71. Marshall, C. E. The physical chemistry and mineralogy of soils.
    Volume I. Soil materials. New York, John Wiley and Sons, Inc.
    1964.

72. Martin, R. Torrence. Adsorbed water on clay: a review. National
    Conference on Clays and Clay Minerals Proceedings 9: 28-70. 1960.

73. Means, R. E. and Parcher, J. V. Physical properties of soils.
    Columbus, Ohio, Charles E. Merrill Books, Inc. 1963.

74. Mering, J. On the hydration of montmorillonite. Faraday Society
    Transactions 42B: 205-219. 1946.

75. Mesri, G. and Olson, R. E. Consolidation characteristics of mont-
    morillonite. Geotechnique 21, No. 4: 341-352. 1971.

76. Messina, M. L. Expansion of fractional montmorillonite under various
    relative humidities. Clays and Clay Minerals 19: 617-632. 1964.

77. Mielenz, R. C. and King, M. E. Physical-chemical properties and
    engineering performance of clays. State of California Department of
    Natural Resources, Division of Mines Bulletin 169: 196-254. 1955.

78. Milne, I. H. and Warshaw, C. M. Methods of preparation and control
    of clay mineral specimens in X-ray diffraction analysis. National
    Conference on Clays and Clay Minerals Proceedings 4: 22-30. 1956.

79. Mooney, R. W., Keenan, A. G. and Wood, L. A. Adsorption of water
    vapor by montmorillonite. I. Heat of desorption and application
    of BET theory. American Chemical Society Journal 74: 1367-1371.
    1952.

80. Mooney, R. W., Keenan, A. G. and Wood, L. A. Adsorption of water vapor by montmorillonite. II. Effect of exchangeable ions and lattice swelling as measured by X-ray diffraction. American Chemical Society Journal 74: 1371-1374. 1952.

81. Morgan, J. and Warren, B. E. X-ray analysis of the structure of water. Journal of Chemical Physics 6: 666-673. 1938.

82. Nagelschmidt, G. On the lattice shrinkage and structure of montmorillonite. Zeitschrift für Krstallographie 93: 481-487. 1936.

83. Nahin, Paul G. Swelling of clay under pressure. National Academy of Science - National Research Council Publication 395. 174-185. 1954.

84. Norrish, K. The swelling of montmorillonite. Faraday Society Discussion 18: 120-134. 1954.

85. Norrish, K. and Quirk, J. P. Crystalline swelling of montmorillonite. Nature (London) 173: 255-256. 1954.

86. Norrish, K. and Quirk, J. P. Manner of swelling of montmorillonite. Nature (London) 173: 256-257. 1954.

87. Norrish, K. and Rausell-Colom, J. A. Low angle X-ray diffraction studies of the swelling of montmorillonite and vermiculite. National Conference on Clays and Clay Minerals Proceedings 10: 123-149. 1963.

88. Ockman, N. The infrared and Raman spectra of ice structure. Advances in Physics 7: 199-220. 1958.

89. Olson, Thomas W. Determination of swelling pressure of montmorillonites. Unpublished M.S. thesis. Ames, Iowa, Library, Iowa State University of Science and Technology. 1972.

90. Olson, R. E. and Mesri, G. Mechanisms controlling compressibility of clays. American Society of Civil Engineers Journal 96, No. SM 6: 1863-1878. 1970.

91. Orchiston, H. D. Adsorption of water vapor. III. Homoionic montmorillonites at 25°C. Soil Science 79: 71-78. 1955.

92. Overbeck, J. T. G. The interaction between colloidal particles. In Kruyt, H. R., ed. Colloid Science. Volume I. pp. 245-277. New York, Elsevier Publishing Company. 1952.

93. Owston, P. G. The structure of ice-I, as determined by X-ray and neutron diffraction analysis. Advances in Physics 7: 171-188. 1958.

94. Pauling, L. The nature of chemical bond. Ithaca, N.Y., Cornell University Press. 1960.

95. Pauling, L. The structure of water. In Hadzi, D., ed. The Symposium on Hydrogen Bonding. pp. 1-6. New York, Pergamon Press. 1959.

96. Ravina, I. and Low, P. F. Relation between swelling, water properties and b-dimension in montmorillonite-water systems. Clays and Clay Minerals Journal 20: 109-123. 1972.

97. Roderick, G. L. Water vapor-sodium montmorillonite interaction. Unpublished Ph.D. thesis. Ames, Iowa, Library, Iowa State University of Science and Technology. 1965.

98. Roderick, G. L. and Demirel, T. Water-vapor-sodium montmorillonite interaction. Hwy. Res. Bd., Record No. 128, pp. 45-67. 1966.

99. Rosenqvist, I. Th. The influence of physico-chemical factors upon the mechanical properties of clays. National Conference on Clays and Clay Minerals Proceedings 9: 12-27. 1960.

100. Schofield, R. K. Ionic force in thick films of liquid between charged surfaces. Faraday Society Transactions 42B: 219-228. 1946.

101. Senich, D. X-ray diffraction and adsorption isotherm studies of the calcium montmorillonite-H_2O system. Unpublished Ph.D. thesis. Ames, Iowa, Library, Iowa State University of Science and Technology. 1966.

102. Spangler, M. G. Soil Engineering. Scranton, Pa., International Textbook Company. 1960.

103. Takizawa, M. Mechanism of water vapor adsorption on bentonite. Tokyo Institute of Physical and Chemical Research, Scientific Papers 54: 313-322. 1960.

104. Taylor, D. W. Fundamentals of soil mechanics. New York, John Wiley and Sons, Inc. 1948.

105. Terzaghi, K. The physical properties of clays. M.I.T. Technical Engineering News 9: 10-36. 1928.

106. Topping, J. Errors of observation and their treatment. London, The Institution of Physics. 1957.

107. van Olphen, H. Compaction of clay sediments in the range of molecular particle distances. National Conference on Clays and Clay Minerals Proceedings 11: 178-187. 1963.

108. van Olphen, H. Forces between suspended bentonite particles. National Academy of Sciences - National Research Council Publication 456: 204-224. 1955.

109. van Olphen, H. Interlayer forces in bentonite. National Academy of Sciences - National Research Council Publication 327: 418-438. 1954.

110. van Olphen, H. An introduction to clay colloid chemistry. New York, Interscience Publishers. 1963.

111. van Olphen, H. Unit layer interaction in hydrous montmorillonite systems. Journal of Colloid Science 17: 660-667. 1962.

112. Verwey, E. J. W. and Overbeck, J. Th. G. Long distance forces acting between colloidal particles. Faraday Society Transactions 42B: 117-131. 1946.

113. Verwey, E. J. W. and Overbeck, J. Th. G. Theory of the stability of lyophobic colloids. New York, Elsevier Publishing Company, Inc. 1948.

114. Warkentin, B. P., Bolt, G. H. and Miller, R. D. Swelling pressure of montmorillonite. Soil Science Society of America Proceedings 21: 495-497. 1957.

115. Warkentin, B. P. and Schofield, R. K. Swelling pressures of dilute Na-montmorillonite pastes. National Conference on Clays and Clay Minerals Proceedings 7: 343-349. 1957.

116. White, W. A. Water adsorption properties of homoionic montmorillonite. National Academy of Science - National Research Council Publication 395: 186-204. 1954.

117. Winterkorn, H. W. The condition of water in porous systems. Soil Science 55: 109-115. 1943.

118. Wu, T. H. A nuclear magnetic resonance study of water in clay. Geophysical Research Journal 69: 1083-1091. 1964.

119. Yong, R., Taylor, L. O. and Warkentin, B. P. Swelling pressures of sodium montmorillonite at depressed temperatures. National Conference on Clays and Clay Minerals Proceedings 11: 268-281. 1963.

120. Zettlemoyer, A. C., Young, G. J. and Chessick, J. J. Studies of the surface chemistry of silicate minerals. Journal of Physical Chemistry 59: 962-966. 1955.

ACKNOWLEDGEMENTS

of Earth Science and Dr. Robert A. Lohnes, Associate Professor of Civil

Engineering, for serving as committee members.

Finally, I wish to express my gratitude to the Thailand-United States

Educational Foundation for the Travel Grant to the United States and

back to Thailand.

APPENDIX I

Surface Area Determination

Total surface area:

From $\Sigma = \dfrac{N\sigma}{M_s}$

where N is Avogadro number $= 6.023 \times 10^{23}$,

M_s is the formula $(Al_{3.34}Mg_{0.06}Si_8O_{20}(OH)_4Na_{0.66})$ weight of a unit cell layer,

σ is the area exposed by one unit cell layer.

$M_s = 742$ gm

$\sigma = 2 \times 5.16 \times 8.94 \ \text{Å}^2$

where $a_o = 5.16$ and $b_o = 8.94$ are the unit cell dimension (33).

After substituting, $\Sigma = 748 \ m^2/gm$ for sodium montmorillonite.

External surface area:

$$\Sigma_e = \frac{N_A q_m s}{M} \tag{1}$$

$M =$ molecular weight of water $= 18$ gm

$q_m = 0.023$ (from BET plot of Roderick (97))

$s = 10.8 \ \text{Å}^2$

$N_A = 6.023 \times 10^{23}$

After substituting, $\Sigma_e = 83.0 \ m^2/gm$.

APPENDIX II

Total Integrated Intensity Corrected for the Lorentz-polarization Factor

At p/p_o = 0, d_{001} = 9.9

From Bragg Equation, $\sin \theta = \dfrac{\lambda}{2d} = \dfrac{1.54}{2d}$

$\therefore \sin \theta = \dfrac{0.77}{d} = \dfrac{0.77}{9.9} = 0.078$

From Table 5.25B page 270, International Tables for X-ray Crystallography (54), the Lorentz-polarization factor = 325.7

Total Intensity = 5.3 in^2

The data was obtained at the range of 500 cps

$\therefore$ Area 1 $in^2 = \dfrac{500}{10}$ (60) = 3000 counts

$\therefore$ Total Intensity = 5.3 (3000)=15.9 x 10^3 counts

Corrected total Intensity = $\dfrac{15.9 \times 10^3}{325.7}$ = 48.6 counts.

APPENDIX III

Swelling Pressure or Consolidation Pressure Determination
(van Olphen's Method)

In order to calculate the swelling pressure by this method it is necessary to know the free energy accurately. The free energy change is obtained from the graphical integration of Equation (4). This can be determined from the area under the curve of the $\frac{q}{p/p_o}$ versus p/p_o plot for the adsorption run as shown by Roderick (97, p. 94). The free energy change ΔF is calculated from the formula

$$\Delta F = -\frac{RT}{M} \, I$$

$$= -\frac{(8.314 \times 10^7)(297.5)}{(18.02)(748 \times 10^4)} \, I$$

$$\Delta F = -183.5 \, I$$

where I is the value of the area under the curve being considered. In order to prevent the uptake of any interlayer water between the platelets, the value of I is 0.2210. For the beginning of the second and third states of hydration the values of I are 0.1099 and 0.0685, respectively.

The free energy change for the first state of hydration is

$$\Delta F = -183.5 \, (0.2210) = -40.55 \text{ ergs/cm}^2$$

For the second state of hydration $\Delta F = -183.5(0.1099)$

$$= -20.17 \text{ ergs/cm}^2.$$

For the third state of hydration $\Delta F = -183.5(0.0685)$

$$= -12.57 \text{ ergs/cm}^2.$$

Dividing by the diameter of one water molecule, the swelling

pressure $= \dfrac{40.55}{(2.76 \times 10^{-8})}$ dynes/cm^2

$= \dfrac{40.55}{(2.76 \times 10^{-8})(9.5760 \times 10^{5})}$ tons/ft^2

$= \dfrac{40.55 \times 10^{3}}{9.5760 \times 2.76}$ tons/ft^2

Swelling pressure $= 1534$ tons/ft^2.

Similarly, the swelling pressure for the second and third state of hydration will be 763 and 476 tons/ft^2, respectively. Consolidation pressures can be similarly calculated, but using ΔF data from the desorption run.

APPENDIX IV

Calculation of Pressure on the Clay Sample

Assuming the gage pressure = 100 psi.

Corrected pressure from calibration curve = 110 psi.

Area of the large piston = 0.7854 in^2

$\therefore$ Load on the large piston = 110(0.7854) lbs.

Area of the sample chamber = 0.0861 in^2.

$\therefore$ Pressure on the sample = $\dfrac{110(0.7854)}{0.0861}$ psi.

The value 9.121 is the area ratio of the piston and the sample chamber. This is a factor to convert the corrected gage pressure to pressure on the sample.

Pressure on the sample = 110(9.121) = 1003.310 psi

1 tons/ft^2 = 13.889 psi.

$\therefore$ Pressure on the sample = $\dfrac{1003.310}{13.889}$ = 72.21 tsf.

APPENDIX V

Calculation of Modulus of Elasticity

The equation of the straight line in $y = 16.449 - 0.000463x$

where

y = first order basal spacing in Angstrom

x = pressure on the sample

when

$x = 0$, $y = 16.449$ Å

Modulus of elasticity $E = \dfrac{\text{stress}}{\text{strain}}$

Let the initial thickness of the sample at zero pressure is equal to $y = 16.449$ = y-intercept of the equation.

The final thickness of the sample at 3204.73 tons per square foot is 15.030 Å (from Table 14)

$$\therefore \text{Strain} = \frac{(16.449 - 15.030)}{16.4449} = \frac{1.419}{16.449}$$

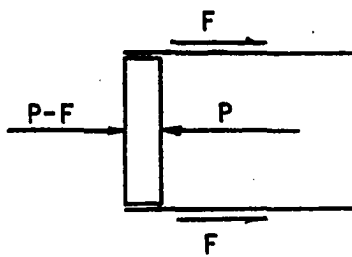$$\therefore E = \frac{3204.73 \times 16.449}{1.419} = 37149.121 \text{ tsf}$$

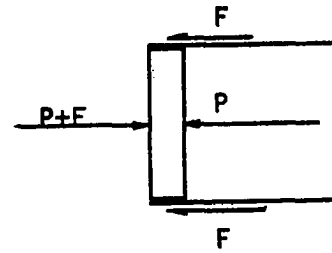$E = 13.889 \,(37149.121) = 515{,}964$ psi

Modulus of elasticity = 515,964 psi.

APPENDIX VI

Hysteresis between Loading and Unloading Conditions

The system of forces in the loading and unloading conditions can be shown below as

Loading condition   Unloading condition

Assuming zero hysteresis, at identical basal spacing and for the elastic deformation

$$(P-F) \text{ for loading} = (P+F) \text{ for unloading}$$

where

P = Pressure applied over the sample

F = Friction

∴ $2F = 0$ = hysteresis.

But there exist the hysteresis, so 2F is equal to the hysteresis between the loading and unloading cycle. This hysteresis consists of apparatus friction, elastic deformation of the platelets of the clay particles and difficulty in water squeezing and reentering between the platelets.